Doctoral Dissertation

博士論文

The size and angular momentum evolution of high redshift galaxies

(高赤方偏移銀河におけるサイズと角運動量の進化)

A Dissertation Submitted for Degree of Doctor of Philosophy, December 2019

令和元年 12 月　博士（理学）申請

Department of Astronomy, Graduate School of Science, The University of Tokyo

東京大学大学院　理学系研究科　天文学専攻

Taku Okamura

岡村拓

Supervisor:
Associate Prof. Kazuhiro Shimasaku : Department of Astronomy, School of Science, The University of Tokyo

Abstract

The morphology, size, and angular momentum of galaxies are three fundamental quantities that can be used as probes for internal structure and kinematics. Studying these quantities at high-redshift provides us invaluable insights for galaxy formation and evolution.

This thesis consists of two parts. In the first part, we investigate the angular momentum evolution of disk galaxies at $z \sim 2$, 3, and 4. The stellar disk size of a galaxy depends on the fraction of the dark halo mass settled as disk stars, $m_\star \equiv M_\star/M_{dh}$, and the fraction of the dark halo angular momentum transferred to the stellar disk, $j_\star \equiv J_\star/J_{dh}$. Since $m_\star$ and $j_\star$ are determined in a different manner by a series of star-formation related processes such as inflows and feedbacks, measuring $j_\star$ and $m_\star$ at various redshifts is needed to understand those processes and thus the formation history of disk galaxies. However, angular momentum studies at $z > 1$ are still very limited because it is difficult to kinematically measure $j_\star$.

We use the 3D-HST GOODS-S, COSMOS, and AEGIS imaging data and photo-z catalog, where stellar masses and star formation rates are also given, to examine $j_\star$ and $m_\star$ for star-forming galaxies at $z \sim 2$, 3, and 4, when disks are actively forming. For each redshift, we divide the catalog into $M_\star$ bins and infer M_{dh} from clustering analysis and abundance matching, thus obtaining $m_\star$ for each bin. We also measure, for objects in each bin, effective radii r_d at rest 5000Å with `GALFIT` which, combined with Mo et al.'s (1998) analytic disk formation model and M_{dh} and $m_\star$ measurements, gives $j_\star$ without measuring disk kinematics.

We find that the $j_\star/m_\star$ ratio is $\simeq 0.77 \pm 0.06$ for all three redshifts over the entire mass range examined, $8 \times 10^{10} < M_{dh}/h^{-1}M_\odot < 2 \times 10^{12}$, with a possible ($< 30\%$) decrease with mass. This high ratio is close to those of local disk galaxies, descendants of our galaxies in M_{dh} growth, implying a nearly constant $j_\star/m_\star$ over past 12 Gyr. It is found that recent theoretical galaxy formation simulations predict smaller j_d/m_d than our values. We also find that a significant fraction of our galaxies appear to be unstable against bar formation. We also examine the r_d–$M_\star$ relation for our galaxies, finding shallow power-law slopes of the relation decreasing from $\simeq 0.19$ at $z \sim 2$ to $\simeq 0.08$ at $z \sim 4$. These shallow slopes less than 0.2 reflect the non-positive slopes of the $j_\star/m_\star$-M_{dh}

relation, and the decrease toward $z \sim 4$ may be due to a decrease (getting more negative) in the slope of the $j_\star/m_\star$-M_{dh} relation over the same redshift range.

In the second part, we focus on the size and morphology of galaxies. We use a cosmological hydrodynamical simulation framework, FiBY, which is an updated version of Gadget-3 in order to investigate what problem would happen if we adopt the same size measurement procedure as one used in the local universe for very high-redshift galaxies at $z \sim 6$. The simulated galaxies are lensed onto the *Hubble* Frontier Fields (HFF) cluster image, and the sizes are measured on the mock image. By comparing the intrinsic sizes ($r_{\rm sim}$) in the simulations and the observed sizes ($r_{\rm obs,mock}$) in the mock observations, we have examined whether the surface brightness profile of the simulated galaxies is reproduced by a single Sérsic profile.

We find that our $r_{\rm sim}$–luminosity relation is slightly higher than the incompleteness corrected size–luminosity relation by Kawamata et al. (2018). On the other hand, $r_{\rm obs,mock}$ is measured two or three times smaller than $r_{\rm sim}$; the $r_{\rm obs,mock}$–luminosity relation is comparable to the incompleteness uncorrected size–luminosity relation. This is because the surface brightness limit of the HFF image is too shallow, and a single Sérsic profile can not trace the extended structure of our simulated galaxies.

For local to intermediate redshift galaxies, we can measure the accurate galaxy sizes by using the size measurement method assuming a Sérsic profile. However, our results in the second part indicate that we need special care to apply a Sérsic profile to very high-redshift galaxies at $z > 6$, because the sizes of galaxies may be underestimated by the size measurement procedure.

Acknowledgments

I would like to express my sincere gratitude to my advisors, Associate Prof. Kazuhiro Shimasaku for invaluable advices and thorough instructions. This study owes to his keen and thoughtful insight. I sincerely appreciate his conducting the burdensome-business tasks and all of the time he has spared. I feel especially thankful to my collaborator, Dr. Ryota Kawamata, who have suggested lots of efficient ways and helped me with the data reduction and analysis. Also, I cannot thank him enough for his help in my daily lives.

My heartfelt appreciation goes to Prof. Ken Nagamine for his invaluable advises on scientific and technical problems. I also would like to thank Mr. Syohei Arata, who has helped me with the data reduction and analysis. Without their support, I could not have completed the work in this Thesis.

I am grateful to Dr. Tanja Petrushevska, Dr. Michael Fall, Dr. Adam Stevens, Dr Masamune Oguri for their helpful comments. I am gratitude to the anonymous referees assigned by ApJ for useful comments that improved our studies.

I greatly appreciate the helps by and daily interactions with members of our laboratory, Dr. Rieko Momose, Dr. Takuya Hashimoto, Mr. Ryosuke Goto, Dr. Haruka Kusakabe, Mr. Kazushi Irikura, Mr. Makoto Ando, and Ms. Hinako Goto and members of our research group, Associate Prof. Masami Ouchi, Assistant Prof. Yoshiaki Ono, Dr. Takatoshi Shibuya, Dr. Akira Konno, Dr. Masafumi Ishigaki, Dr. Yuichi Harikane, Dr. Seiji Fujimoto, Mr. Haibin Zhang, Mr. Takashi Kojima, Mr. Yuma Sugahara, Mr. Shiro Mukae, Mr. Ryo Higuchi, Miftahul Hilmi, Mr Ryohei Itoh, and Mr. Shotaro Kikuchihara. I wish to thank members of the Department of Astronomy, the University of Tokyo, for the daily discussions and chats with them, particularly my colleagues from the Bachelor course, Mr. Kazuhiro Noda, Mr. Ryo Ando, Mr. Satoshi Kikuta, Mr. Tadafumi Matsuno Ms. Misako Tatsuuma, Mr. Kiyoshi Mouri, Mr. Sora Fujimoto, and Mr. Masato Ishizuka.

As the last of this section, I would like to express my gratitude to my parents, Yasuhiro Okamura, Mitsuyo Okamura, who allow me to go on to graduate school and support me throughout my entire life. I also thank my sister, Mayu Okamura, for warm encouragements and kind understanding.

This thesis is reviewed by Prof. Kentaro Motohara (chair), Prof. Takeshi Okuda, Prof.

Michiko Fujii, Prof. Akio Inoue, and Prof. Masao Mori.

Contents

List of Figures

List of Tables

Chapter 1

Introduction

1.1 Galaxy Evolution

Since William Herschel discovered that our galaxy 'Milky Way' is a cluster of stars, galaxies have fascinated us with their beautiful shapes. We now know that a galaxy is a more complex self-gravitating system that is composed of an innumerable number of stars, cold gas, dust, and a surrounding dark matter halo. Galaxies are not only mere cradles of stars but the building blocks of the Universe. They are distributed across cosmological time scales with brightness that can be observed, which allows astronomers to probe the evolution history of the Universe.

As the Universe evolves, the nature of galaxies also changes. One of the most noticeable properties is morphology. In the past Universe, most of the galaxies have disky or irregular shapes. Toward the present day, however, there appear a growing number of elliptical galaxies with orderly structures. It is because a fraction of disk and irregular galaxies evolve into ellipticals for some reasons. Interestingly, the morphologies of galaxies are closely related to their global properties, such as luminosity, color, gas content, and star formation. These properties also evolve along with the evolution of morphology. Therefore, the morphologies of galaxies reflect the underlying fundamental physics.

It is an intriguing mystery of the Universe why and how galaxies evolve. The recent development of large telescopes has opened a new way to observe the evolution of galaxies back to the first several hundred million years of the Universe. These telescopes make it possible to measure various properties including internal structure and kinematics of galaxies over the wide range of redshifts. In addition, the improvement of numerical techniques and computational power allows modeling a vast range of dynamic scales of the Universe from the large scale cosmic web to the internal structure of a single galaxy. Cosmological galaxy formation simulations have made remarkable progress in reproducing the various scaling relations of galaxies and helped to interpret observations. We are

now in the golden age of extragalactic astronomy, because we are, and we will soon be, able to understand the evolution process of galaxies from their birth thorough detailed observations and cosmological simulations.

1.2 Structure and Kinematics of Galaxies

It is important to study the evolution of galaxies from the perspective of structure and kinematics. Angular momentum, size, and morphology are three fundamental quantities that can be used as probes for internal structure and kinematics. These quantities are in the scope of this study.

Morphology

Galaxies have a variety of shapes. Edwin Hubble ordered galaxies based on their shapes, which is known as the Hubble sequence (Hubble, 1936). Although the Hubble sequence classifies galaxies based only on morphology, many other properties like color, age, and gas content also change along the sequence. According to the sequence, galaxies can be roughly classified into three types: disks, ellipticals, and irregulars. Disk galaxies are characterized by a thin disk, which include a bar, spiral arms, and a central bulge. Disks are rotationally supported and primally contain young stars and cold gas. Elliptical galaxies, on the other hand, have a smooth elliptical isophote and are composed of old stars and little cold gas. They are mainly supported by velocity dispersion and generally have a low rotation velocity.

Angular momentum

Disks galaxies and ellipticals are also separated by their angular momentum. When galaxies are formed, their angular momentum acquired by tidal torques stops the gas concentration, which leads to the formation of disks. Thus angular momentum plays an essential role in forming the disks of galaxies. Disk galaxies retain the initial specific angular momentum obtained by tidal torques almost fully through the concentration process and evolution history, whereas elliptical galaxies dissipate angular momentum through mergers and have a low specific angular momentum.

Galaxy size

Galaxy sizes are a more direct quantity that can be easily measured and provide information on kinematics. Since the angular momentum of disk galaxies play a crucial role in the formation of disks, disk sizes reflect the amount of the specific angular momentum. Thus, disk sizes can be used as an alternative measure of angular momentum, especially at high redshift where constructing a large spectroscopic sample is difficult.

1.3 Cosmological Simulations

Cosmological simulations have been strong tools to predict galaxy formation and evolution within the ΛCDM cosmology ever since early attempts to simulate galaxy formation in the cosmological context (e.g., Navarro & Benz, 1991; Navarro & White, 1994).

There exist two different approaches to model galaxy formation: semi-analytical modeling and hydrodynamical simulations. A hydrodynamical simulation is a straightforward way to calculate gravity and hydrodynamical equations for DM, gas, and stars. The 3D positions and velocities of these particles and/or grid cells are traced, by accounting for interactions with each other, which makes it possible to study the kinematics and other properties of galaxies in detail. The other complementary way is semi-analytical modeling, which was firstly developed by White & Frenk (1991). A semi-analytical model utilizes merger trees calculated by N-body simulations and does not calculate fundamental equations. Alternatively, some simplified recipes are implemented: the cooling rate of hot gas, the conversion rate of cold gas into stars, and feedbacks from supernovae and AGNs. The advantage of semi-analytical models is that they alleviate the calculation cost that imposes a severe limitation to the box sizes and resolution of hydrodynamical simulations even for latest computers.

Cosmological zoom-in simulations are a suite of numerical techniques, which have become popular in recent years. In zoom-in simulations, a subvolume including a matter of interest such as a halo or a galaxy is simulated at a higher resolution within a surrounding region at a low resolution. The low-resolution surroundings provide a tidal field allowing for the precise calculation of the zoom-in region. After an initial run at a coarser resolution, a halo of interest is selected, and mass particles in the regions are traced back to the initial state. The distribution of the mass particles determines the zoom-in region. The selected zoom-in region is filled with much more highly resolved particles, and the entire volume is re-simulated. A final run includes baryonic components such as gas and stars, and hydrodynamics is turned on. Zoom-in simulations in this way allow studying small scale baryonic processes precisely accounting for the effect of large scale structures within limited computing resources.

Early hydrodynamical simulation projects suffered from a crucial angular momentum catastrophe. During the assembly process of gaseous cores, a large proportion of their angular momentum has been transferred to the surrounding halo. A resulting galaxy had only a small fraction of specific angular momentum. Therefore simulations made only early-type galaxies and failed to produce pure disks (e.g., Navarro & White, 1994;

Sommer-Larsen et al., 1999; Navarro & Steinmetz, 2000). This problem has been improved by using an adequate numerical resolution and implementing an efficient SF feedback (e.g., Sommer-Larsen et al., 1999; Kaufmann et al., 2007; Governato et al., 2007). An efficient SF feedback ejects low angular momentum gases in the center of galaxies and redistributes it to the outskirts, resulting in extended disk galaxies (Brook et al., 2012).

In recent years, large-volume cosmological hydrodynamical simulations have been conducted and made significant progress in reproducing the structures and morphologies of galaxies with a wide range of redshift, which include Illustris (Vogelsberger et al., 2014; Genel et al., 2014), IllustrisTNG (Pillepich et al., 2018, 2019), and EAGLE (Schaye et al., 2015; Crain et al., 2015). These high-resolution simulations with a proper treatment of feedbacks produce late-type galaxies whose disk sizes and angular momentum are comparable to observed ones especially at $z \sim 0$ (e.g., Brook et al., 2011; Genel et al., 2015; Lagos et al., 2017).

1.4 Angular Momentum and their importance on the Formation of Disk Galaxies in ΛCDM cosmology

Within the ΛCDM paradigm, galaxies form in the center of hierarchically growing dark matter halos (Fall & Efstathiou, 1980). In the tidal torque theory, gases and dark matter halos acquire angular momenta with a log-normal distribution of the spin parameter through tidal gravitational fields (Peebles, 1969). The dimensionless spin parameter is given by

$$\lambda \equiv \frac{J|E|^{1/2}}{GM^{5/2}}, \tag{1.1}$$

where J, E, and M are the total angular momentum, total energy, and total mass of the system. Since gases and halos share initial tidal torque fields, it is expected that gases and dark matter halos have the same amount of specific angular momentum. Gases gradually radiate away the thermal energy and then cool and collapse toward the center of dark matter halos. Their angular momentum halts the collapse and leads to a rotationally supported disk galaxy (Fall & Efstathiou, 1980; White & Frenk, 1991; Mo et al., 1998).

In this formation scenario of disk galaxies, the disk size of a galaxy ($r_{\rm d}$) is given by

$$r_{\rm d} = \frac{1.678}{\sqrt{2}} \left(\frac{j_{\rm d}}{m_{\rm d}} \right) \lambda r_{200} f_{\rm c}(c_{\rm vir})^{-1/2} f_{\rm R}(\lambda, c_{\rm vir}, m_{\rm d}, j_{\rm d}), \tag{1.2}$$

(Mo et al., 1998). Here $j_{\rm d}/m_{\rm d}$ ($j_{\rm d} \equiv J_{\rm d}/J_{\rm dh},\ m_{\rm d} \equiv M_{\rm d}/M_{\rm dh};$ d :star+gas) is the angular momentum retention factor and displays how much angular momentum acquired via tidal

torques is conserved during the disk formation, r_{200} is the radius of the dark matter halo within which the average density is 200 times of the critical density, and $f_{\rm c}$ and $f_{\rm R}$ show, respectively, the difference in the density profile from an exponential profile and the gravitational effect of the disk. By assuming that the angular momentum of a disk is fully conserved, $j_{\rm d}/m_{\rm d} = 1$, this model successfully reproduces scaling relations of local disk galaxies: the stellar mass–size relation and the stellar mass–size scatter relation (Mo et al., 1998; Dutton & van den Bosch, 2012; Romanowsky & Fall, 2012). Because of this success, this model has been adopted in many semi-analytical models (e.g. Hatton et al., 2003; Somerville et al., 2008; Guo et al., 2011; Porter et al., 2014; Henriques et al., 2015; Croton et al., 2016; Tonini et al., 2017).

However, the assumption that $j_{\rm d}/m_{\rm d}$ equals to unity independent of mass and cosmic time is not trivial, because the angular momenta of dark matter halos and disk galaxies evolve differently. Dark matter halos increase their angular momentum at the outskirts through mergers, smooth accretion, and cosmic expansion (Obreschkow et al., 2015). On the other hand, highly-complex baryonic processes such as cooling, dynamical friction, and various feedback processes can change the specific angular momentum of disk galaxies (e.g. DeFelippis et al., 2017; Tonini et al., 2017). These processes are closely dependent on the mass of host dark matter halos. For example, the mass of dark matter halos controls how much expelled gases, which exchange the angular momentum with hot halo gases, can return to the galaxies again. The accumulation of such processes may increase or decrease the disk specific angular momentum. This is why the information of angular momentum is essential for comprehensive understanding of galaxy formation and evolution. It is important to understand the evolution of the angular momentum of galaxies as a function of dark halo mass at various redshifts.

In the present-day universe, since the pioneer work of Fall (1983), the angular momenta of galaxies with various morphological types and masses have been studied by observations and cosmological simulations (e.g. Steinmetz & Navarro, 1999; Governato et al., 2007; Romanowsky & Fall, 2012; Fall & Romanowsky, 2013). Romanowsky & Fall (2012) and Fall & Romanowsky (2013) have extended and updated the study of Fall (1983) with recent observational data. They have found that the specific angular momenta of spiral galaxies are not conserved, with $j_{\rm d}/m_{\rm d} \simeq 0.8$ independent of halo mass. This implies that some baryonic processes mentioned above decrease the disk specific angular momentum. Recent semi-analytical and hydrodynamical galaxy formation models have also obtained low angular momentum retention factors (Sales et al., 2012; Genel et al., 2015; Colín et al., 2016; Stevens et al., 2016; Lagos et al., 2017). Lagos et al. (2017) have investigated the specific angular momentum of simulated galaxies with EAGLE and found excellent

agreement with observations especially at $z \sim 0$. With Illustris, Genel et al. (2015) have demonstrated that the stellar angular momenta of late-type and early type galaxies show different types of relations as suggested by the observation of Romanowsky & Fall (2012). The roles of baryonic processes that determine the disk specific angular momentum have been examined: they include various types of feedback processes and the formation of bulges by disk instabilities.

On the other hand, beyond $z \sim 1$, there are only a few studies that have observationally examined the specific angular momentum of galaxies because of the difficulty in obtaining kinematic measurements. Burkert et al. (2016) have analyzed the angular momenta of 359 disk star-forming galaxies at $z \sim 0.8-2.6$ and found $j_{\rm d}/m_{\rm d} \simeq 1$. Contini et al. (2016) have found in 28 low mass galaxies at $z \sim 1$ almost the same stellar mass–angular momentum relation as the local one. However, some semi-analytical and hydrodynamical models predict that disk galaxies at $z \sim 1$ have smaller specific angular momenta than local galaxies (e.g. Sales et al., 2012; Pedrosa & Tissera, 2015). Some results of cosmological galaxy formation simulations support the picture in which disk galaxies gradually acquire specific angular momentum as they grow (Obreschkow et al., 2015; Colín et al., 2016). A consensus has not been reached on the angular momentum evolution beyond $z \sim 1$. More observational data are needed to test the model predictions: disk galaxies are formed with high specific angular momentum at the early stage of their formation or they are formed with low specific angular momentum but increase it through their evolution with some baryonic processes.

In this thesis, to tackle the issue of the angular momentum evolution of disk galaxies and understand the formation and evolution of galaxy disks, we study the relation between the fraction of the dark-halo angular momentum transferred to the stellar disk ($j_\star$: $\star$:star) and the stellar to dark matter halo mass ratio ($m_\star$) at $z \sim 2$, 3, and 4. We estimate dark halo masses by two independent methods: clustering analysis and abundance matching technique. In order to measure $j_\star$, it is popular to analyze galaxy kinematics with spectroscopy. However, it is very difficult to construct a large spectroscopic sample at high redshifts. Instead, we make use of the analytical model of Mo et al. (1998) that connects disk size with angular momentum. By measuring the disk sizes of galaxies and assuming this analytic model, we estimate $j_\star$.

Kravtsov (2013) has investigated stellar disk size to halo size ratios ($r_{\rm d}/r_{\rm dh}$), which also reflect angular momentum retention factors, for local galaxies with a similar approach. Kawamata et al. (2015) and Shibuya et al. (2015) have extended his study to high redshift galaxies and found that the disk size to halo size ratios are almost flat out to high redshift. Recently, Huang et al. (2017) and Somerville et al. (2018) have examined the

disk size to halo size ratios as a function of stellar mass in more detail out to $z \sim 3$ from CANDELS surveys using abundance matching. They have found that the disk sizes are proportional to the halo sizes from $z \sim 0 - 3$ and the ratios slightly decrease toward $z \sim 0$ and high stellar masses. Our studies are complementary to these studies. There are some new aspects in our work. We study the mass–angular momentum relation at high redshift. Moreover, while all previous studies have used abundance matching analysis, we use clustering analysis, which is an independent of method to estimate dark halo masses. We also compare our results with recent cosmological galaxy formation simulations.

1.5 Galaxy Sizes at very High Redshift

Recently, thanks to the development of large ground-based and space telescopes, large samples of galaxies at very high redshift ($z > 6$) have been constructed (e.g., McLure et al., 2013; Bowler et al., 2014; Finkelstein et al., 2015). In particular, *Hubble Space telescope* (HST) with the Wide Field Camera 3 (WFC3) has dramatically improved our ability to probe the structure and kinematics of galaxies. The *Hubble* Frontier Fields (HFF; Coe et al., 2015; Lotz et al., 2017) is a revolutionary HST deep survey program with the aim of imaging six massive cluster fields and six parallel fields. The strong gravitational lensing effect by the foreground clusters allows detecting faint sources down to $M_{\rm UV} \sim -16\,{\rm mag}$ (Atek et al., 2014, 2015; Castellano et al., 2016; Livermore et al., 2017). These considerably deep images have boosted the effort to study the sizes of faint galaxies ($M_{\rm UV} > -20\,{\rm mag}$) at $z \geq 6$ (Kawamata et al., 2015; Laporte et al., 2016; Bouwens et al., 2017; Kawamata et al., 2018).

The accurate size measurements of high redshift galaxies ($z \geq 6$) can tell us valuable information on galaxy evolution. As with the case of low-redshifts, galaxy sizes are a direct probe of kinematics and can be used as an alternative measure of angular momentum. By tracing the evolution of galaxy sizes, the relationship between galaxies and dark matter halos is also invesgated (e.g., Kravtsov, 2013; Somerville et al., 2018). In addition, size distribution of high-redshift galaxies is needed to correct the detection completeness of the UV luminosity function. At a given magnitude, the detectability of a large galaxy is lower than that of a small galaxy because the former has a lower surface brightness. Therefore, source sizes have a large impact on the determination of the faint end slope of the UV luminosity function, which constrains how faint galaxies play a crucial role in ionizing the Universe. Kawamata et al. (2018) have provided size measurements of $z = 6 \sim 9$ LBGs at $-21.6 < M_{\rm UV} < -12.3$ using the six cluster fields and six parallel fields data and reported that these galaxies have tremendously small sizes. By utilizing the fact that the surface

brightness of galaxies rely on the lensing shear, Bouwens et al. (2017) have also indicated that the intrinsic sizes of faint galaxies are small.

The improvements in simulation techniques allow some hydrodynamical simulations and semi-analytical models to study the size–luminosity relation of faint galaxies at $z \geq 6$ (Ma et al., 2018b; Arata et al., 2019; Marshall et al., 2019). These studies have predicted a larger size than observed at the faint end of the size–luminosity relation. Ma et al. (2018b) have predicted the sizes and morphologies of simulated galaxies at $z \geq 5$ with hydrodynamical cosmological zoom-in simulations from the Feedback In Realistic Environments (FIRE) project (Hopkins et al., 2014). The simulated galaxies have shown extended intrinsic structures, and the UV flux has been dominated by some small clumps. However, it is not an easy task to compare the results of observations and simulations, at such high redshifts because of significant surface brightness dimming and a clumpy morphology of galaxies. In addition, because these faint galaxies have been detected on strongly lensed fields, uncertainties due to the mass modeling of clusters, sky noise, the methodology of size measurements may affect measured sizes.

1.6 Problem on Measuring Sizes at very High Redshift

For size measurements of galaxies, there are some different approaches. Among them, a traditional and popular way is to perform surface brightness fitting assuming a Sersic (1968) profile (e.g., Davies et al., 1988; Simard et al., 1999; Peng et al., 2002; Trujillo et al., 2007; Tasca et al., 2009; Huang et al., 2013; Ono et al., 2013; van der Wel et al., 2014; Kawamata et al., 2015; Shibuya et al., 2015; Bouwens et al., 2017; Paulino-Afonso et al., 2017; Kawamata et al., 2018; Gillman et al., 2019). This is motivated by the studies of local galaxies. In the local Universe, the bulges of early-type galaxies are well fitted with a $n = 4$ Sérsic profile, and the disks of late-type galaxies tend to have a $n = 1$ Sérsic profile (Courteau et al., 1996; Andredakis, 1998). The advantage of adopting a parametric profile for size measurements is that it does not depend on the choice of the size of an aperture. As the size of an aperture determines total flux, the galaxy sizes measured by a non-parametric method is biased by the size of the aperture (Curtis-Lake et al., 2016). An alternative way to define a galaxy size is a non-parametric approach, which defines the size by an aperture enclosing a half or some percentage of total flux (e.g., Oesch et al., 2010; Curtis-Lake et al., 2016; Arata et al., 2019) or the number of pixels above a surface brightness threshold (Law et al., 2007; Ribeiro et al., 2016; Ma et al., 2018b).

From local to intermediate redshifts, size measurements assuming a parametric profile require high signal-to-noise (SN) ratio, but the method generally works well. As the surface

brightness dimming is not severe, we can observe the tail of galaxies, which is enough to measure the accurate size of galaxies. On the other hand, some specific problems occur at high redshifts. Recent observational studies have reported that very high-redshift galaxies tend to have clumpy and irregular structures (e.g., Jiang et al., 2013; Bowler et al., 2017). Jiang et al. (2013) have investigated the structure and morphology of spectroscopically confirmed LBGs and LAEs at $z \geq 6$ and found that about half of them exhibit merging or interacting features. Bowler et al. (2017) have also found that the fraction of clumpy or merging like galaxies is higher than 40 percent at the bright end ($M_{\rm UV} < -22.5$) of a sample of $z \simeq 7$ LBGs with HST data. These studies have suggested that high redshift galaxies are not well fitted by a simple parametric profile. Measured sizes and luminosities may have large systematic errors if intrinsic shapes are not described by a single Sérsic profile. In addition to that, because of low SN combined with strong cosmological surface brightness dimming, it is technically difficult to optimize many structural parameters simultaneously: positions, luminosities, elongation, position angle, and Sérsic index. Thus it is still unknown if parametric methods such as Sérsic fitting are similarly applicable, but most of the previous studies attempt the same method as the local one.

How to define a galaxy size is a complicated problem especially for these galaxies. Because local galaxies tend to have well-ordered shapes, the half-light radius of a galaxy is not affected by the definition of a galaxy size. However, for very high-redshift galaxies with clumpy shapes, it can happen that a galaxy size changes depending on how we define it. This is ultimately a problem of what the size of a galaxy is and which definition of a galaxy size is physically meaningful. For example, how do we define a galaxy size for the correction of the UV luminosity function? If a galaxy is clumpy, the detectability at a given magnitude is not simply a function of size. It also depends on morphology. We also need to consider the situation in which a clumpy galaxy is detected as multiple galaxies. When we estimate angular momentum from observed sizes, we assume that a galaxy is well approximated by a parametric profile. If this assumption is not the case, the discussion is vulnerable.

This thesis aims to investigate what problem would happen if we adopt the same size measurement procedure as one used in the local universe for very high-redshift galaxies. To achieve this purpose, we provide mock observed size–luminosity relations by using hydrodynamical cosmological zoom-in simulations and investigate whether the surface brightness profile of simulated galaxies is reproduced by a single Sérsic profile by comparing intrinsic sizes in the simulations and observed sizes in the mock observations. We use a cosmological hydrodynamical simulation framework, FiBY, which is an updated version of Gadget-3. The simulated galaxies are lensed onto the Abell2744 cluster field

and measured in the almost same manner as Kawamata et al. (2015, 2018).

1.7 Overview of This Thesis

This thesis consists of two parts. In Chapters $2-6$, we investigate disk angular momenta at $z \sim 2, 3$, and 4. In Chapters $7-9$, we compare size–luminosity relations at $z \sim 6$ with the mock observations and with the intrinsic relation. The layout of this thesis is as below.

In Chapter 2, we describe the sample selection in the 3D-HST and CANDELS programs. In Chapter 3, we present how we measure the sizes of galaxies with GALFIT. In Chapter 4, we obtain the best-fit stellar mass–size relation for our galaxies, assuming a single power law for a stellar mass–size relation and a log-normal distribution at a given stellar mass. We discuss the evolution of the median size (in section 4.2.1) and the slope (in section 4.2.2), and the scatter (in section 4.2.3) for the stellar mass–size relations. In Chapter 5, we estimate the hosting dark matter halo masses with two independent techniques: clustering analysis and abundance matching. In Chapter 6, we calculate disk specific angular momenta from the results in Chapter 4 and Chapter 5 and compare our results with those of recent SAMs and hydrodynamical simulations.

In Chapter 7, we describe the details of our cosmological hydrodynamical zoom-in simulations. In Chapter 8, we present the method of the mock observations. The simulated galaxies are lensed onto the HFF image mosaics, and we conduct size measurements with an almost same way as the real observational campaign accounting for the gravitational lensing effect and the PSF. We also define galaxy sizes so as to fairly compare the sizes in mock observations with those in simulations. In Chapter 9, we show size–luminosity relations obtained through mock observations and compare with observations (in section 9.1) and discuss the validity of assuming a Sérsic profile (in section 9.2).

Conclusions are given in Chapter 10.

Throughout this thesis, we adopt a flat cosmological model with the matter density $\Omega_M = 0.3$, the cosmological constant $\Omega_\Lambda = 0.7$, the baryon density $\Omega_b = 0.045$, and the Hubble constant $H_0 = 70\,\mathrm{km\,s^{-1}\,Mpc^{-1}}$, the power-law index of the primordial power spectrum $n_s = 0.965$, and the linear amplitude of mass fluctuation $\sigma_8 = 0.8$ (Planck Collaboration et al., 2016). We assume a Chabrier (2003) initial mass function (IMF). Magnitudes are in the AB system (Oke & Gunn, 1983), and coordinates are given in J2000. Galaxy sizes are given in the physical scale.

Chapter 2

Data and samples

2.1 Data

We use data from the 3D-HST and CANDELS programs (Grogin et al., 2011; Koekemoer et al., 2011; Brammer et al., 2012; Skelton et al., 2014). Skelton et al. (2014) provide a photometric catalog of the 3D-HST and CANDELS imaging data for five sky fields (COSMOS, GOODS-North, GOODS-South, AEGIS, and UDS) with a total area of ~ 900 arcmin^2. As these fields have wealthy available data of optical to near-infrared broadband photometry, one can obtain a precise spectral energy distribution (SED) for many high-redshift galaxies. The number of optical to near-infrared broadband filters ranges from 18 in UDS up to 44 in COSMOS. We make use of photometric redshift, stellar mass, and star formation rates (SFR), all of which are available through the 3D-HST Web site.[*3] Sources have been detected with `SExtractor` (Bertin & Arnouts, 1996) from the combined F125W, F140W, and F160W images. Among the five fields we only use COSMOS, GOODS-South, and AEGIS fields because the clustering properties of galaxies in the remaining two fields appear to largely deviate from the cosmic average as detailed in Appendix.

Photometric redshifts have been determined from the `EAZY` (Brammer et al., 2008) package, a public photometric redshift code. From the output catalog of `EAZY`, we adopt `z_peak` as photometric redshifts. Stellar masses and SFRs have been obtained by using the `FAST` code (Kriek et al., 2009). See Skelton et al. (2014) for details of the procedure. In this paper, we assume a Chabrier (2003) initial mass function (IMF). From here, we take photometric redshifts as redshifts.

[*3] http://3dhst.research.yale.edu

Table 2.1: Number of star-forming galaxies for stellar mass subsamples

z	$\log(M_\star/M_\odot)$	Number (Clustering) [a]	Number (Size "success") [b]
2.0	$10.4-11.1$	264	198
	$9.7-10.4$	1086	870
	$9.0-9.7$	3267	2458
	$8.3-9.0$	3173	1772
3.0	$9.7-10.4$	805	560
	$9.0-9.7$	1596	1060
	$8.3-9.0$	838	412
4.0	$9.7-10.4$	273	161
	$9.0-9.7$	348	176
	$8.3-9.0$	133	70

[a] Number of star-forming galaxies used for clustering analysis.

[b] Number of star-forming galaxies that have robust fitting parameters with `GALFIT` detailed in Section 3.1

2.2 Sample selection

We limit our sample to $H_{160} < 26.0$, which is nearly equal to the 5σ complete magnitude in the shallowest field COSMOS (Skelton et al., 2014). As size measurements need images with high signal to noise ratios (S/N), the 5σ limit is marginally acceptable and slightly shallower compared to other size measurement studies (van der Wel et al., 2014; Shibuya et al., 2015). Stellar masses are limited to $M_\star > 10^{8.3} M_\odot$. In the H_{160}–$M_\star$ diagram (Figure 2.1), stellar masses are largely complete down to $M_\star \simeq 10^{9.0} M_\odot$ for $z \sim 2$ and down to $M_\star \simeq 10^{10} M_\odot$ for $z \sim 3$ and 4. Below those values, our samples are biased toward low M/L galaxies. We exclude galaxies with $M_\star > 10^{10.4} M_\odot$ from our samples for $z \sim 3$ and 4 because the number of galaxies is insufficient for clustering analysis.

We use the stellar mass–SFR diagram to remove quiescent galaxies. On the basis of the stellar masses and the SFRs obtained from the `FAST`, we construct stellar mass–SFR diagrams for our samples, as shown in Figure 2.2. First, we fit the stellar mass–SFR distribution by a power law, which defines the main-sequence. At $z \sim 2$ and 3, galaxies that lie above the -2σ of the main-sequence are considered to be star-forming galaxies, where the standard deviation of the MS is $\sigma \simeq 0.33$ dex for both redshifts. For $z \sim 4$, we remove galaxies that have small SFRs by eye. In this paper, we do not consider the effects

of bulges because main sequence galaxies above $z \sim 2$ have low B/T ratios (Brennan et al., 2017).

We exclude regions that have a shallow or deep exposure time for each field because clustering analysis requires images with a uniform depth. We also construct masks to avoid the vicinity of bright stars and diffraction spicks. For each redshift, we divide the entire sample into four ($z \sim 2$) or three ($z \sim 3$ and 4) subsamples according to stellar mass. The number of galaxies in the final samples is summarized in Table 2.1.

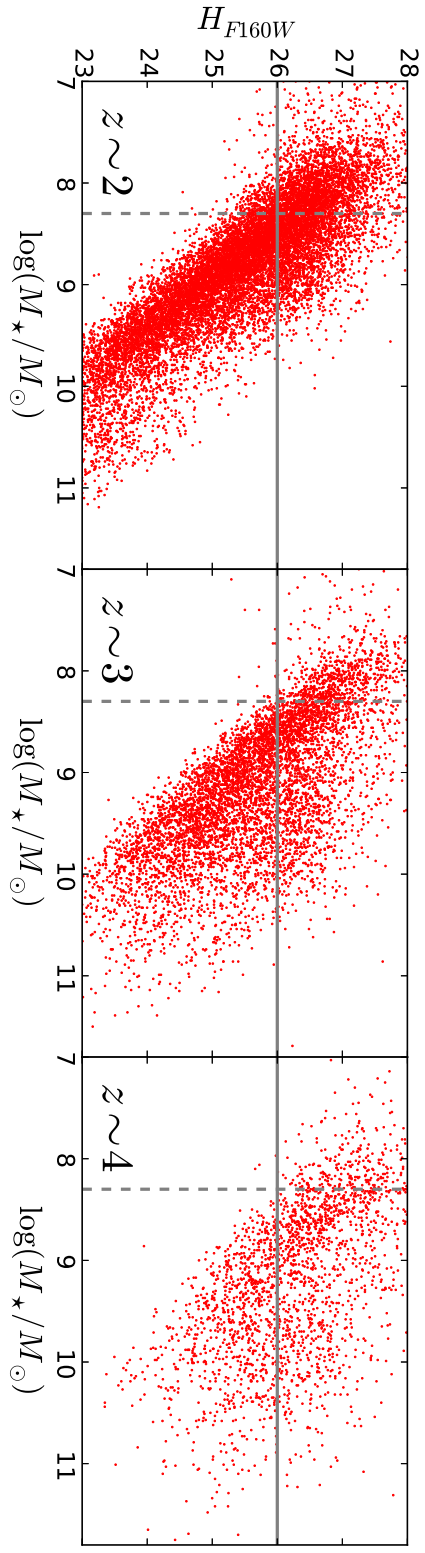

Figure 2.1: $H_{160} - M_\star$ diagram at $z \sim 2$, 3, and 4 (left to right). The vertical dashed lines and horizontal solid lines indicate the stellar mass limits and the observed H_{F160W} magnitude limits, respectively.

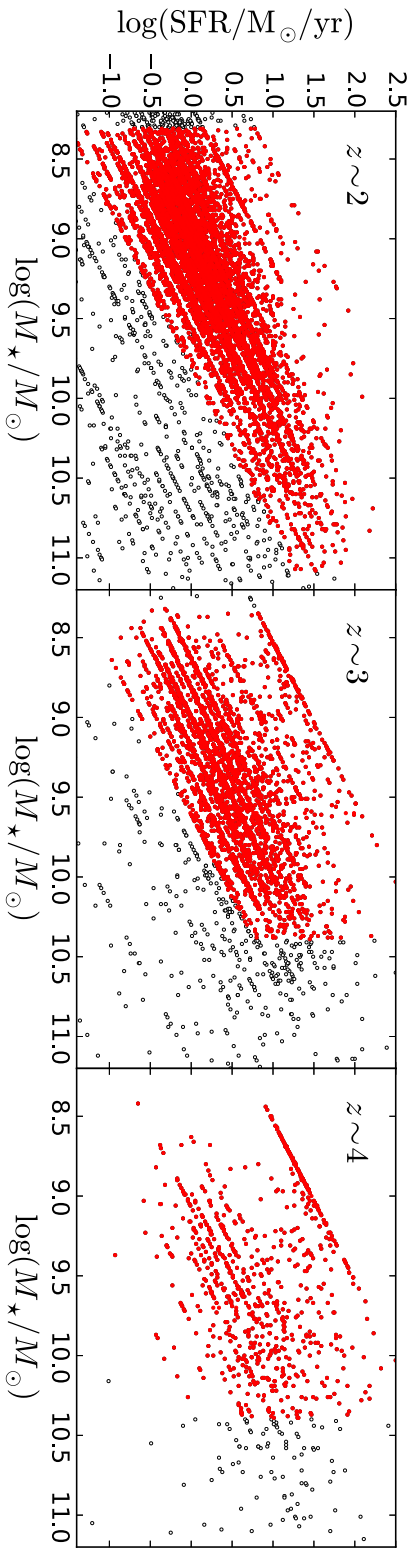

Figure 2.2: SFR vs. stellar mass diagram at $z \sim 2-4$ (left to right). Objects used in our study are shown in red.

Chapter 3

Size measurements

3.1 Size measurements with GALFIT

Galaxy sizes are measured for the F160W imaging data provided by the 3D-HST. Position, flux, half-light radius ($r_{\rm d}$), Sérsic index (n), axis ratio ($q \equiv b/a$), and position angle are treated as free parameters to determine. In this paper, we use the half-light radius along the semi-major axis of the Sérsic profile to define the size of galaxies. We make 100 pixels $\times$ 100 pixels cutout images around object galaxies before size measurement. We then run GALFIT (Peng et al., 2002, 2010) on those cutout images, where neighbors are masked as not to perturb the fitting of the target galaxies. The masks are created from SExtractor segmentation maps.

As an initial guess of the free parameters, we use SExtractor output parameters given in the 3D-HST catalog. Results of GALFIT are not sensitive to initial values as long as they are not far from real values Häussler et al. (2007). We vary individual parameters over the following ranges: $\Delta x,\ \Delta y < 3$ pixels, $0.3 < r_{\rm d} < 100$ pixel, $0.1 < n < 8$, $0.1 < q < 1$, where Δx and Δy are the difference in the centroids between SExtractor and GALFIT. We define galaxies whose best-fit parameters are within these ranges as "success". We only use "success" galaxies in the following analysis in Sections 3 and 4. The number of "success" galaxies is summarized in Table 2.1. While we obtain robust structural parameters of only a part of our clustering sample, the average SExtractor sizes of the "success" sample and the entire sample are nearly equal. Thus we use the GALFIT sizes of the "success" sample as the representatives of the entire sample.

Figure 3.1 shows the distributions of Sérsic index (n) at $z \sim 2$, 3, and 4. Most of our galaxies have $n \sim 1-2$; the majority of our samples are disk-like galaxies. The median of Sérsic index (n) for each stellar mass subsample is summarized in Tabel 3.1.

Table 3.1: Median of Sérsic index (n) and normalized correction factor of angular momentum for stellar mass subsamples

z	$\log(M_\star/M_\odot)$	n [a]	$f_n(n)^{-1}/f_n(1)^{-1}$ [b]
2.0	$10.4-11.1$	0.88	0.97
	$9.7-10.4$	1.14	1.03
	$9.0-9.7$	1.28	1.06
	$8.3-9.0$	1.19	1.04
3.0	$9.7-10.4$	1.23	1.05
	$9.0-9.7$	1.25	1.06
	$8.3-9.0$	1.15	1.03
4.0	$9.7-10.4$	1.22	1.05
	$9.0-9.7$	1.17	1.04
	$8.3-9.0$	1.16	1.03

[a] Median of Sérsic index (n)

[b] Normalized correction factor of specific angular momentum (j_d) detailed in Section 6.1

3.2 Deriving $r_{\rm d}$ at rest-frame 5000$\AA$

We derive $r_{\rm d}$ at the rest-frame 5000$\AA$ at all redshifts. While we measure sizes in observed 1.6μm (F160W band), there exists a color gradient that depends on stellar mass and redshift. We obtain rest 5000$\AA$ $r_{\rm d}$ by using the formula given in van der Wel et al. (2014):

$$r_{\rm d} = r_{{\rm d},F160W}\left(\frac{1+z}{1+z_p}\right)^{\Delta\log r_{\rm d}/\Delta\log\lambda}. \tag{3.1}$$

where z_p is the "pivot redshift"(2.2 for F160W) and the wavelength dependence is given by:

$$\frac{\Delta\log r_{\rm d}}{\Delta\log\lambda} = -0.35 + 0.12z - 0.25\log\left(\frac{M_\star}{10^{10}M_\odot}\right). \tag{3.2}$$

Although van der Wel et al. (2014) have only examined wavelength dependence over $0<z<2$, we extend this formula to $z\simeq 4$ because the redshift evolution of this relation looks linear as a function of redshift. In any case, the correction values at $z\sim 3$ and 4 are relatively small ($\sim 1\%$ at $z\sim 2$, $\sim 1\%$ at $z\sim 3$, and $\sim 10\%$ at $z\sim 4$).

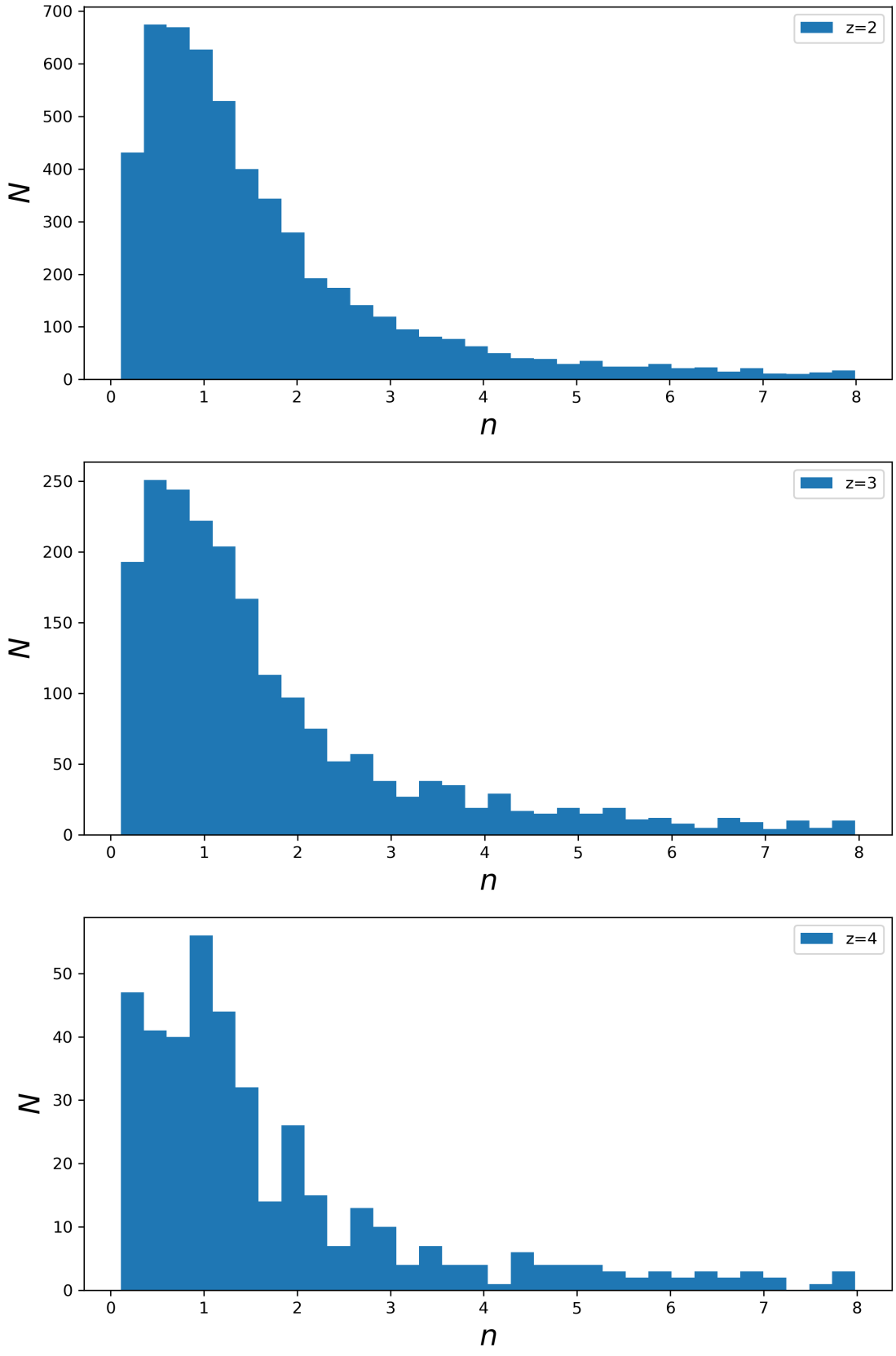

Figure 3.1: Distribution of Sérsic index (n) at $z \sim 2$, 3, and 4 (top to bottom).

Chapter 4

Stellar mass–size relation

The stellar mass–size distributions of our star forming galaxies are shown in Figure 4.1. In Section 4.1, we analyze these distributions by modeling them with a power law. Then, we discuss the results in Section 4.2.

4.1 Analytical Model of the stellar mass–size relation

The stellar mass–size relation is usually modeled as a single power-law:

$$\overline{r}_d(M_{\star,10})/\mathrm{kpc} = A \cdot M_{\star,10}^{\alpha}, \tag{4.1}$$

where $M_{\star,10} = M_\star/1.0 \times 10^{10} M_\odot$, and $\overline{r}_d$ $(M_{\star,10})$ is the median size at $M_{\star,10}$. For the size distribution at a given stellar mass, we adopt a log-normal distribution:

$$p(r_d|\sigma_{\ln r}, \overline{r}_d)dr_d = \frac{1}{\sqrt{2\pi}\sigma_{\ln r} r_d} \exp\left(-\frac{(\ln r_d - \ln \overline{r}_d)^2}{2\sigma_{\ln r}^2}\right) dr_d, \tag{4.2}$$

where $p(r_d|\sigma_{\ln r}, \overline{r}_d)dr_d$ is the probability that a galaxy has a size between $(r_d, r_d + dr_d)$ at the given stellar mass, and $\sigma_{\ln r}$ is the dispersion of the distribution. The reason for adopting a log-normal distribution comes from Equation (1.2). The disk size is proportional to the dimensionless spin parameter λ, and the distribution of λ is well approximated by a log-normal distribution according to N-body simulations (Barnes & Efstathiou, 1987; Bullock et al., 2001).

We assume that each of the observed disk size has a gaussian error:

$$g(x|r_d, \delta r_d) = \frac{1}{\sqrt{2\pi}\delta r_d} \exp\left(-\frac{(x - r_d)^2}{2\delta r_d^2}\right). \tag{4.3}$$

The probability of observing $(r_d, \delta r_d)$ assuming the log-normal distribution $p(r_d|\sigma_{\ln r}, \overline{r}_d)$ is given by the convolution of the two functions:

$$(p * g)(r_d) = \int p(x) g(r_d - x) dx. \tag{4.4}$$

We use the 1-σ error in `GALFIT` as δr_d. For each redshift, the free parameters of this model are given by $\mathbf{P} = (A, \alpha, \sigma_{\ln r,i})$, where, i denotes i-th subsample; we assume that different stellar mass bins have different $\sigma_{\ln r}$ values. We have six free parameters at $z \sim 2$, and five free parameters at $z \sim 3$ and 4. We use the maximum likelihood estimation (MLE) to determine these parameters, where the estimated parameters make the observed r_d distribution the most probable. For subsample i at a given redshift, the likelihood function is defined as

$$\mathcal{L} = \prod_{j=1}^{N} (p * g)(r_{d,j}|\sigma_{\ln r,i}, \overline{r}_d), \tag{4.5}$$

where j represents the j-th object. We determine the parameter set $\mathbf{P}$ that will maximize the likelihood function $\mathcal{L}$. The best-fit values are listed in Table 4.1. We use the `scipy.optimize` package to find the maximizing point. The function `fmin_l_bfgs_b` uses the L-BFGS-B algorithm (Zhu et al., 1997). The uncertainties in the parameters are estimated by the Markov Chain Monte Carlo (MCMC) sampling. MCMC is a powerful algorithm to approximate multi-dimensional parameters using a Markov chain. We use the python package `emcee` (Foreman-Mackey et al., 2013) to MCMC. In Figure 4.2-4.4, we show for each parameter the best-fit values and the 68%, 95%, and 99% confidence intervals. This figure is made using the public python package `corner` (Foreman-Mackey, 2016).

Table 4.1: Best-fit parameters of the stellar mass–size relation

z	A	α	$\sigma_{8.3<M_\star<9.0}$	$\sigma_{9.0<M_\star<9.7}$	$\sigma_{9.7<M_\star<10.4}$	$\sigma_{10.4<M_\star<11.4}$
2.0	$2.51^{+0.03}_{-0.05}$	$0.19^{+0.01}_{-0.01}$	$0.46^{+0.01}_{-0.01}$	$0.51^{+0.01}_{-0.01}$	$0.50^{+0.02}_{-0.02}$	$0.53^{+0.03}_{-0.05}$
3.0	$1.94^{+0.06}_{-0.05}$	$0.14^{+0.01}_{-0.03}$	$0.42^{+0.03}_{-0.03}$	$0.47^{+0.02}_{-0.02}$	$0.47^{+0.02}_{-0.02}$	...
4.0	$1.57^{+0.11}_{-0.13}$	$0.08^{+0.05}_{-0.05}$	$0.45^{+0.18}_{-0.05}$	$0.51^{+0.08}_{-0.07}$	$0.47^{+0.09}_{-0.06}$	...

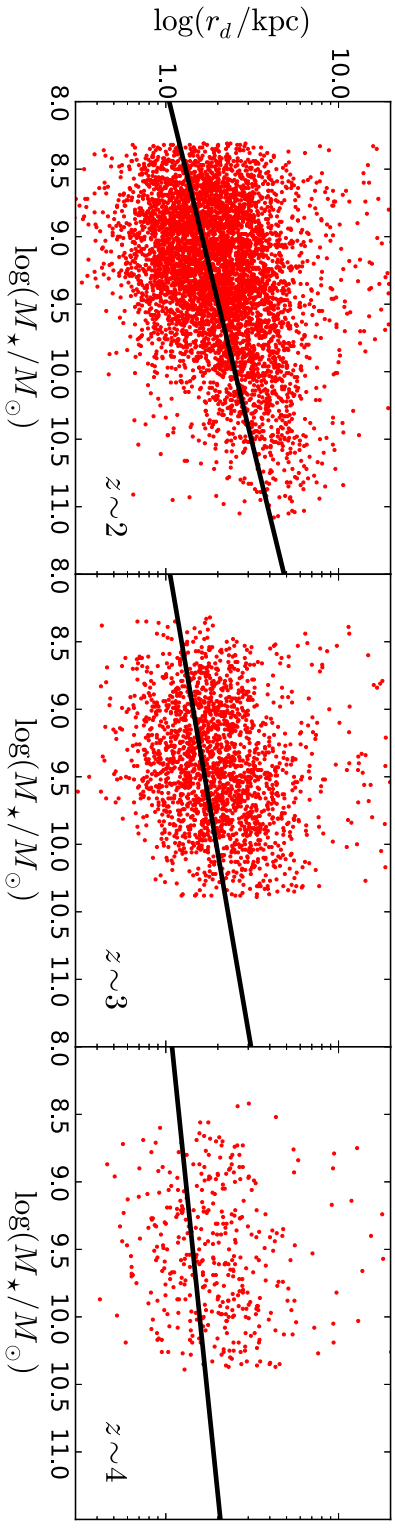

Figure 4.1: Stellar mass–size distribution of disk galaxies at $z \sim 2-4$ (left to right). The solid lines indicate the best-fit power laws.

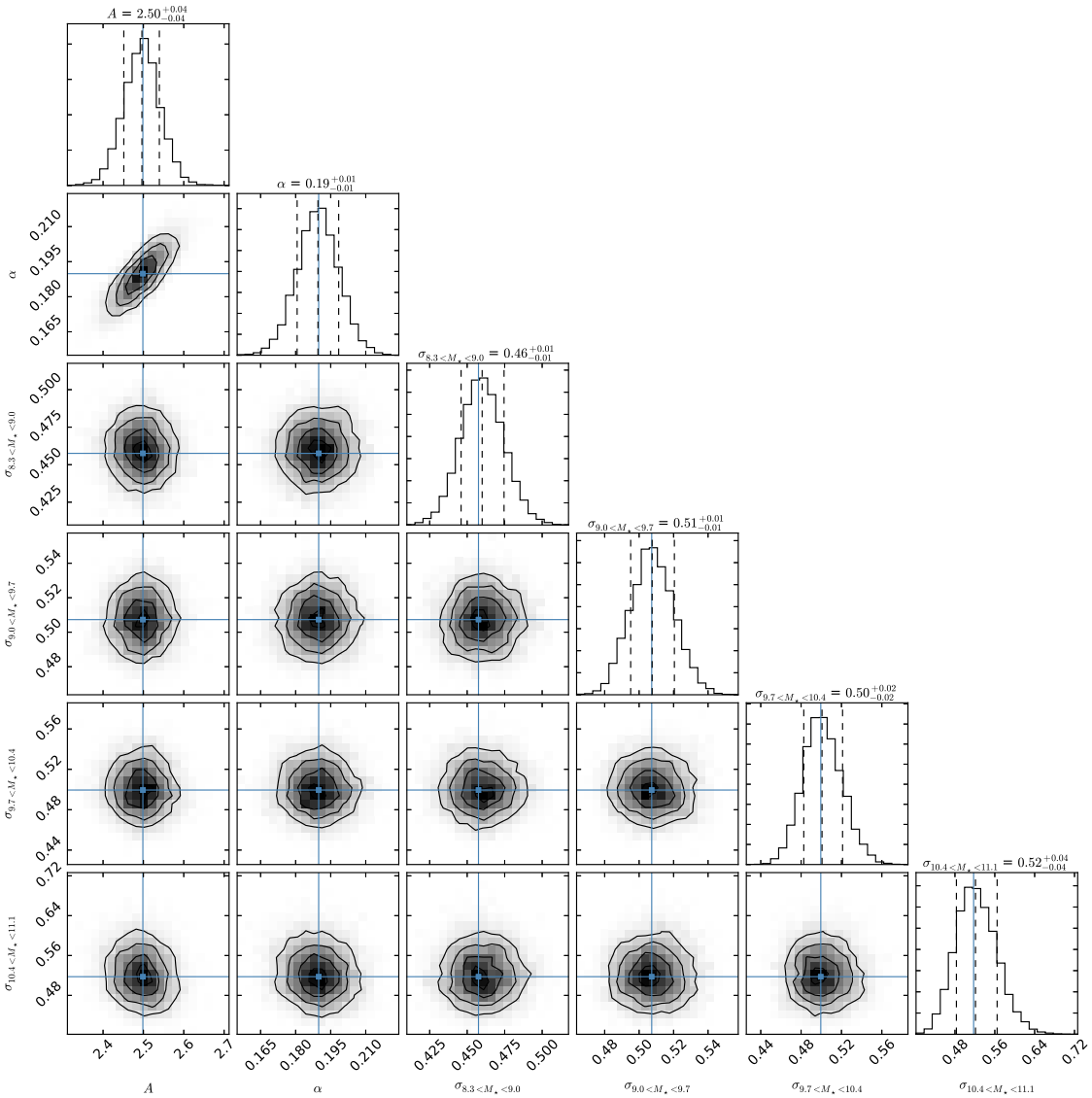

Figure 4.2: Sixty-eight percent, 96%, and 99% confidence intervals for individual parameters at $z \sim 2$. The top panels of each coloum show the probability distribution function of each parameter. The median values and 68% confidence intervals are on the top of each coloum. The solid blue lines indicate the median values.

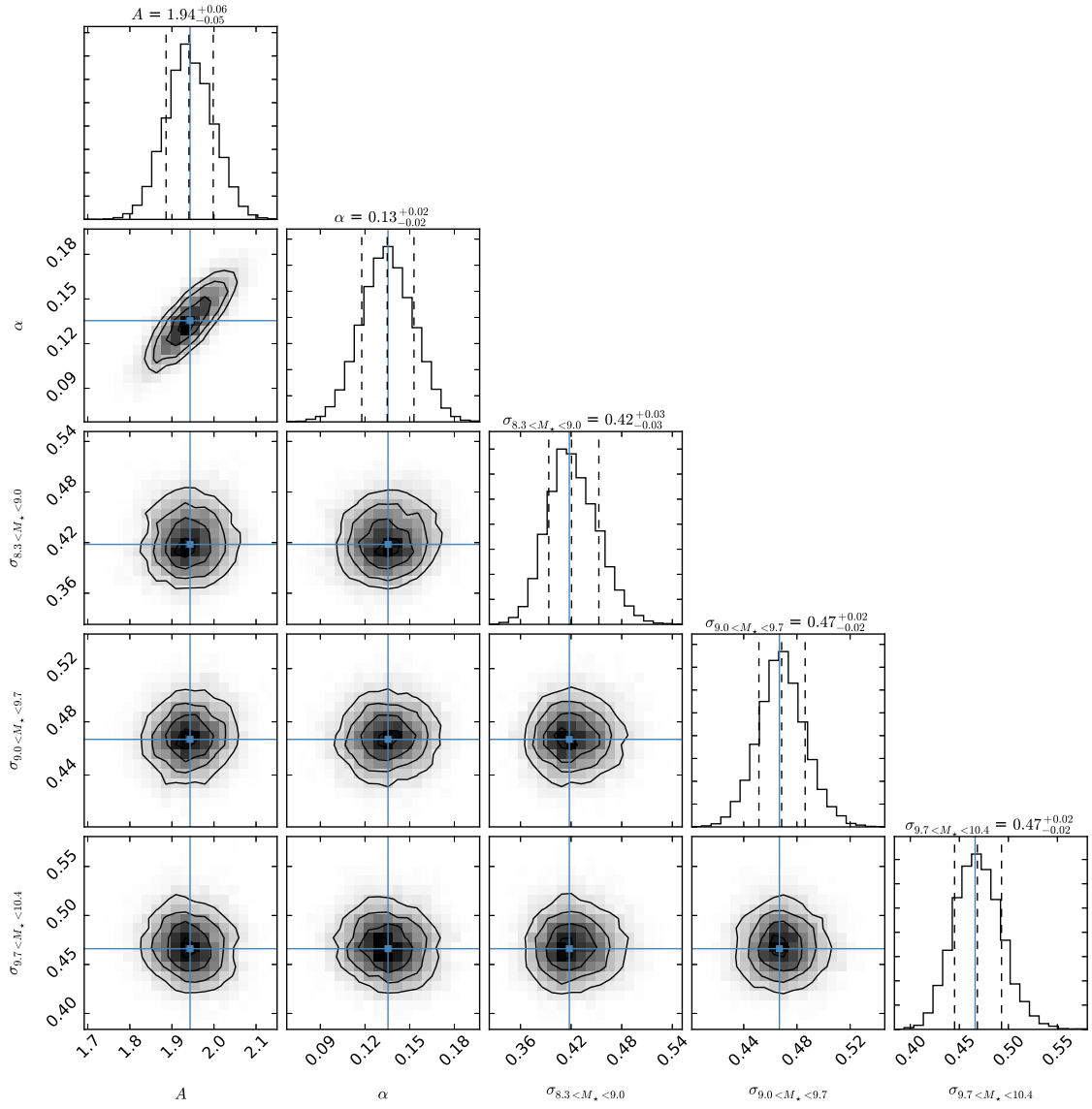

Figure 4.3: Same as Figure 4.2 but for $z \sim 3$.

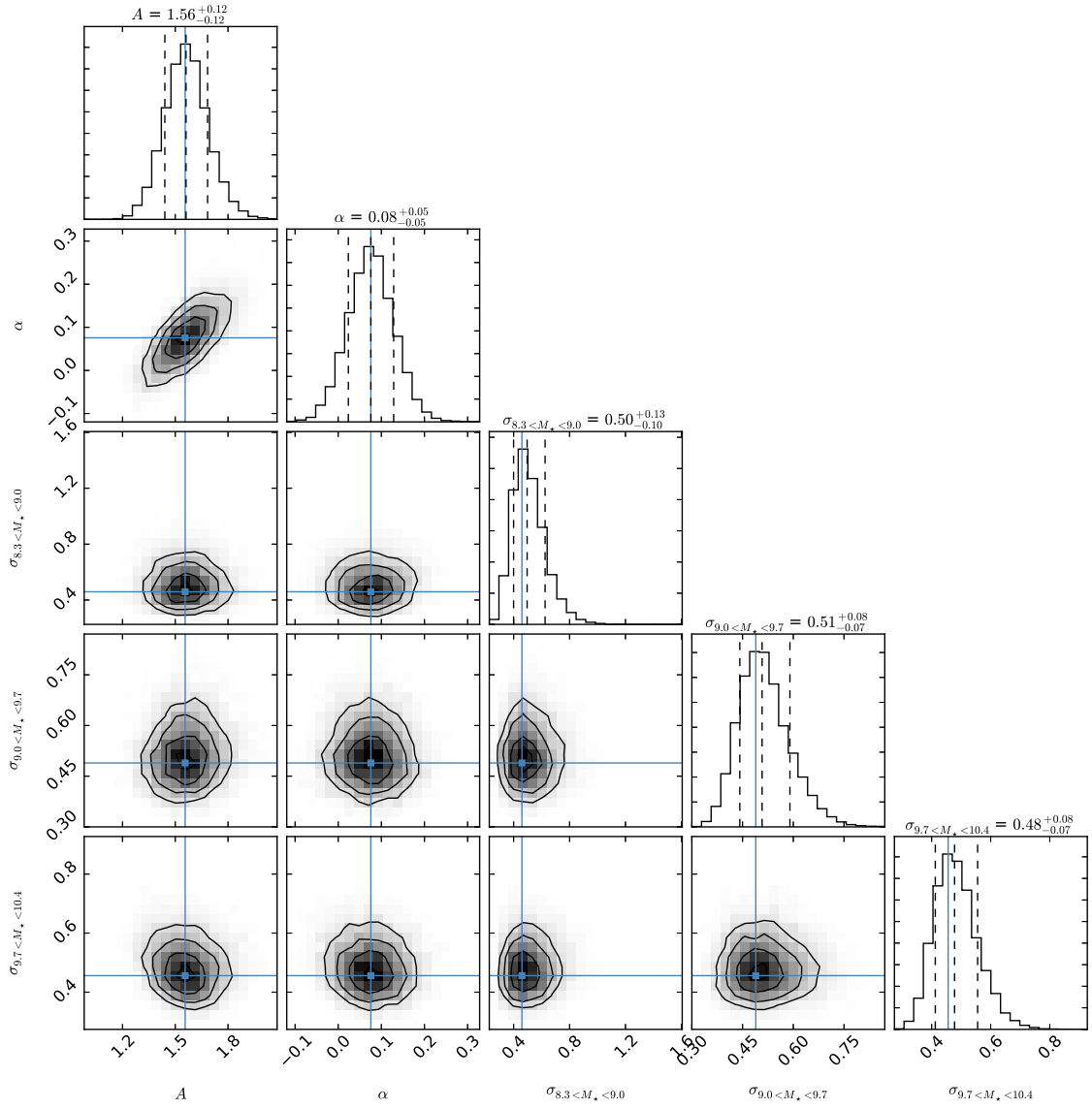

Figure 4.4: Same as Figure 4.2 but for $z \sim 4$.

4.2 Size evolution

The evolution of A, α, and $\sigma_{\ln r}$ are shown in Figure 4.5. In this Section, we discuss the evolution of each parameter in detail.

4.2.1 Median size evolution

The size evolution at a fixed stellar mass is generally parameterized as $(1+z)^{-\beta_z}$, where β_z is a constant expressing the strength of evolution (evolution slope). The top left panel of Figure 4.5 represents the median size evolution of disk star forming galaxies at $M_\star = 1.0 \times 10^{10} M_\odot$. The solid blue line shows the best-fit function over $z \sim 2-4$: $\overline{r}_d(M_{\star,10})/\mathrm{kpc} = 6.88(1+z)^{-0.91\pm0.01}$. Allen et al. (2016) have measured the size evolution of a mass-complete sample ($\log(M_\star/M_\odot) > 10$) of star-forming galaxies over redshifts $z = 1-7$, to find that the average size at a fixed mass of $\log(M_\star/M_\odot) = 10.1$ is expressed by $r_e = 7.07(1+z)^{-0.89\pm0.01}$. The slope we find is in agreement with Allen et al. (2016)'s value. Shibuya et al. (2015) also have measured the stellar mass–median circularized size evolution of star-forming galaxies with $9.0 < \log(M_\star/M_\odot) < 11.0$ at $0 < z < 6$. The gray dotted line represents the average circularized half-light radius from their samples with the gray region showing the 16th and 84th percentiles. The evolution slope is consistent with our result. The difference in the amplitude is due to the different definition of galaxy sizes. We also note that Shibuya et al. (2015) have used the Salpeter IMF (Salpeter, 1955) to derive the stellar masses.

However, $\beta_z = 0.91 \pm 0.01$ is slightly steeper than the value by van der Wel et al. (2014). They have studied a mass complete sample of star-forming galaxies and have found $(1+z)^{-0.75}$ at a $\log(M_\star/M_\odot) = 10.7$ over the redshift range $0 < z < 3$. As their method of size measurements is the same as ours, we attribute this discrepancy to the difference in the redshift range. The evolution slope of star-forming galaxies appears to become steeper above $z \sim 2$ or 3. Allen et al. (2016)'s sample also shows steeper slopes at higher redshifts (See Figure 3 of Allen et al. (2016)).

As size evolution is closely related to the evolution of hosting dark matter halos, β_z contains the information of dark matter halos. From Equation 1.2, when r_d/r_{vir} is constant irrespective of z and M_{dh}, r_d is given by

$$r_d \propto H(z)^{-1} V_c \tag{4.6}$$

$$\propto H(z)^{-2/3} M_{dh}^{1/3}, \tag{4.7}$$

where V_c is the circular velocity of dark matter halos. The Hubble parameter as a function

of z, $H(z) = H_0\sqrt{\Omega_m(1+z)^3+\Omega_\Lambda}$, is approximated as $H(z) \propto (1+z)^{1.5}$. According to Equations 4.6 and 4.7, $r_d \propto (1+z)^{-1.5}$ means evolution at a constant circular velocity and $r_d \propto (1+z)^{-1.0}$ means evolution at a constant virial mass (Ferguson et al., 2004). The $\beta_z = 0.91$ is close to the prediction for a constant virial mass. This is consistent with the really constant $M_\star/M_{dh}$ value (at $M_\star = 10^{10}M_\odot$) over $z = 2-4$ obtained by the clustering analysis and the abundance matching.

4.2.2 Slope evolution

The top right panel of Figure 4.5 shows the slope evolution in the stellar mass–size relation (α). The slope evolution of the stellar mass–size relation for late-type galaxies was first investigated by van der Wel et al. (2014). They have found that the slope has nearly a constant value $\simeq 0.2$ over the redshift range $0 < z < 3$. Similarly Allen et al. (2016) have found $\alpha = 0.15 \pm 0.01$ for star-forming galaxies at $1 < z < 2.5$. Our results are consistent with those of van der Wel et al. (2014) and Allen et al. (2016) at $z \sim 2$ and 3, however, being slightly lower at $z \sim 4$.

The slope evolution of the stellar mass–size relation is determined as a combination of the slope of the stellar mass–halo mass relation and the slope of the disk size–halo size relation. In this thesis, I have measured all three slopes. I will discuss the relation between the three slopes in Chapter 6.

4.2.3 Scatter evolution

We present the evolution of the intrinsic scatter in the bottom left panel of Figure 4.5: here, "intrinsic" means that measurement errors have been removed. The scatter for local galaxies is generally small. Shen et al. (2003) have found $\sigma_{\ln r_d} \sim 0.3$ for both late-type and early type galaxies from SDSS. This result has also been ascertained by the result of Courteau et al. (2007), $\sigma_{\ln r_d} \sim 0.3$, for local spiral galaxies. These studies have been extended by van der Wel et al. (2014) to the high-redshift universe and they have found that the intrinsic scatter had no strong evolution since $z \sim 2.75$ for both late-type and early-type galaxies. In their study, the scatter for late type galaxies is $0.16 - 0.19$ dex, which is comparable to the result of Shen et al. (2003) and Courteau et al. (2007). We extend van der Wel et al. (2014)'s study up to $z \sim 4$, and find that the intrinsic scatter is constant with $0.4 - 0.6$ over $z \sim 2 - 4$.

The scatter of λ has been specifically investigated by N-body simulations and found to be $\sigma_\lambda \sim 0.5$ (Bullock et al., 2001). Thus the disk formation model of Equation 1.2 naively predicts that the intrinsic scatter of sizes is ~ 0.5.

The results for local galaxies imply that the size scatter is smaller than that of the spin parameter λ. To explain the observed small scatters, some mechanisms are needed. One possible mechanism is bulge growth. The growth of bulges increases the specific angular momentum of disks and thus expands disk sizes. Low-spin galaxies selectively grow their bulges. Some kind of disk instability and feedback have also been proposed which remove galaxies with low-spin and high-spin halos.

Our result, $\sigma_{\ln r_d} \sim 0.4 - 0.6$, is comparable with the scatter of the log-normal distribution of λ. This implies that for star-forming galaxies at $z \sim 2-4$ the size scatter at a given stellar mass is fully explained by the scatter of λ. Our result, however, does not agree with the large scatters, $\sigma_{\ln r_d} \sim 0.8 - 0.9$, found by Huang et al. (2013) for the size–UV luminosity relations of $z \sim 4 - 5$ LBGs. This may suggest that the UV luminosity–halo mass relation of LBGs has a considerably large scatter.

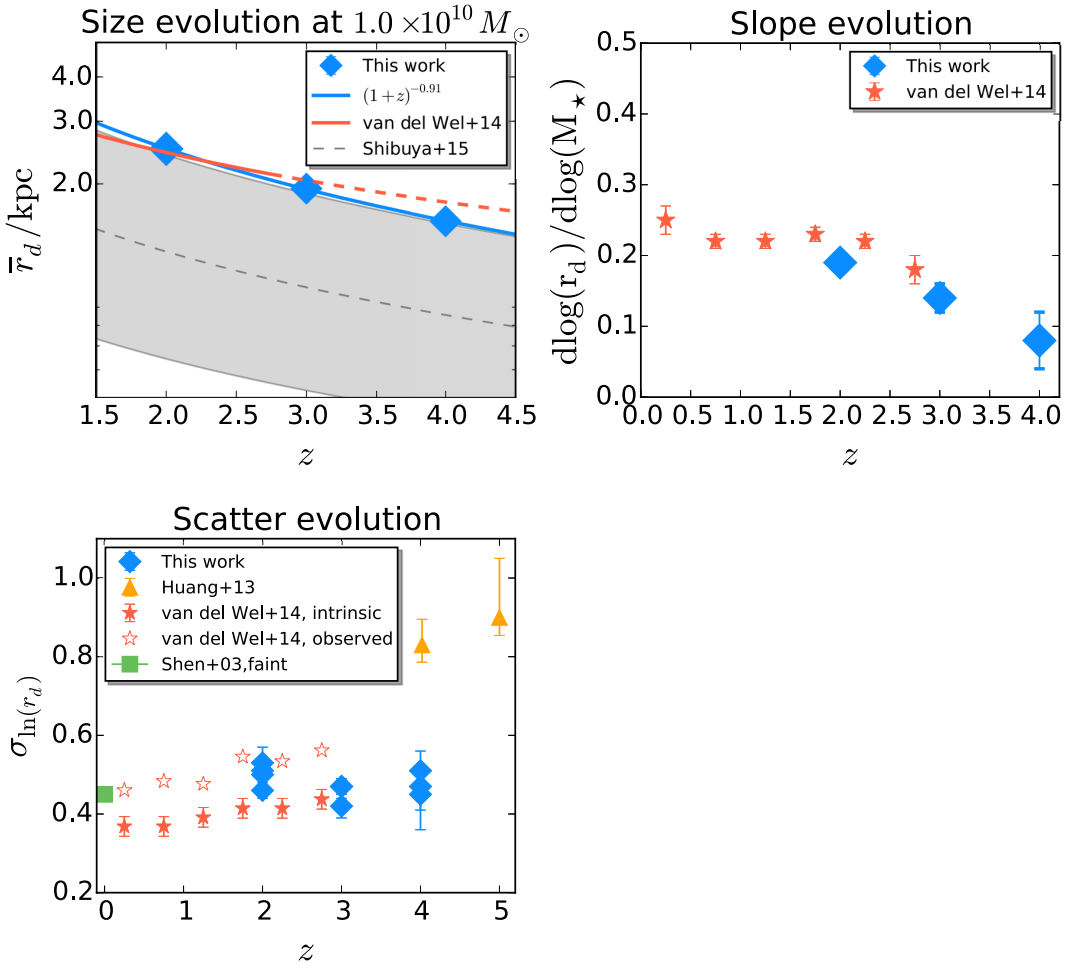

Figure 4.5: Redshift evolution of the stellar mass–size relation of star-forming galaxies. Top left: the size evolution at $M_\star = 1.0 \times 10^{10} M_\odot$. The blue diamond symbols indicate the results obtained in this thesis, and the solid blue line shows the best-fit power-law. The red solid line indicates the size evolution of late-type galaxies from van der Wel et al. (2014) at $10^{9.75} M_\odot$, and the red dashed line is its extrapolation. The gray dotted line and the shaded region indicate the median circularized sizes and 16th and 84th percentiles distribution of star-forming galaxies with $9.5 < \log M_\star/M_\odot < 10.0$ (Shibuya et al., 2015). Top right: slope evolution. The blue symbols represent our galaxies. The red symbols indicate the late-type galaxies from van der Wel et al. (2014). Bottom left: the intrinsic scatter evolution from this work and previous studies. The blue symbols represent our galaxies. The orange symbols represent the LBGs from Huang et al. (2013) at $z \sim 4$ and 5. The red and red open symbols show the late-type galaxies of van der Wel et al. (2014). The green symbol shows the SDSS galaxies of Shen et al. (2003) at the faint end.

Chapter 5

Halo mass estimates

In this Chapter we estimate the masses of the dark matter halos hosting our galaxies by using two independent methods: clustering analysis and abundance matching technique. Clustering analysis utilizes the large scale clustering amplitude of observed galaxies to obtain their hosting dark matter halo masses. Clustering analysis is a popular way to estimate hosting dark matter halo masses, however the mass estimates in this thesis have relatively large errors because the sizes of individual subsamples are not so large. To test the results of the clustering analysis, we use abundance matching technique, which connects the stellar mass of galaxies to that of dark matter halos. While abundance matching can easily estimate hosting dark matter halo masses, it does not consider that different galaxy types have different stellar mass dark halo mass ratios. We briefly explain the two methods and show the obtained dark matter halo masses.

5.1 Clustering analysis

5.1.1 Angular correlation function

We compute the two point angular correlation functions (ACFs), $\omega_{\rm true}(\theta)$, of star forming galaxies. The observed ACFs, $\omega_{\rm obs}(\theta)$, are measured by counting the number of unique pairs of observed galaxies and comparing it with what is expected from random samples. We adopt the estimator proposed by Landy & Szalay (1993):

$$\omega_{\rm obs}(\theta) = \frac{DD(\theta) - 2DR(\theta) + RR(\theta)}{RR(\theta)}, \tag{5.1}$$

where $DD(\theta)$, $DR(\theta)$, and $RR(\theta)$ are the normalized numbers of galaxy-galaxy, galaxy-random and random-random pairs, respectively, with separation θ. We generate 1000 times as many random points as the number of galaxies accounting for the geometry of

the observed area and the masks. The formal error in ω_{true} is given by

$$\sigma_\omega = \sqrt{[1+\omega_{\rm obs}]/DD(\theta)}. \tag{5.2}$$

We assume a power low parameterization for the ACF,

$$\omega_{\rm true}(\theta) = A_\omega \theta^{-\beta}. \tag{5.3}$$

We fix $\beta = 0.8$ following previous studies (e.g., Peebles, 1975; Ouchi et al., 2001, 2004, 2010; Foucaud et al., 2003, 2010; Harikane et al., 2016).

It is known that $\omega_{\rm obs}$ is underestimated because we only use a finite survey area. This is compensated by introducing an integral constant (IC; Groth & Peebles, 1977):

$$\omega_{\rm true} = \omega_{\rm obs} + {\rm IC}. \tag{5.4}$$

The IC value depends on the size and shape of the survey area, and is estimated using a random catalog:

$${\rm IC} = \frac{\sum_i RR(\theta_i)\omega_{\rm true}(\theta_i)}{\sum_i RR(\theta_i)} = \frac{\sum_i RR(\theta_i)A_\omega\theta^{-\beta}}{\sum_i RR(\theta_i)}. \tag{5.5}$$

Because the three 3D-HST fields used in this thesis have almost the same size, we obtain nearly the same IC value ($\rm IC_{GOODS-S} = 0.016A_\omega$, $\rm IC_{COSMOS} = 0.013A_\omega$, and $\rm IC_{AEGIS} = 0.010A_\omega$). The amplitude A_ω is estimated through the ACFs of the three fields by minimizing χ^2:

$$\chi^2 = \sum_{i,\ j={\rm fields}} \frac{A_\omega\theta_i^{-\beta} - [\omega_{obs,j}(\theta_i) + {\rm IC_j}]}{\sigma^2_{\omega,j}(\theta_i)}, \tag{5.6}$$

where $\rm IC_j$, $\omega_{{\rm obs},j}$, and $\sigma^2_{\omega,j}(\theta)$ denote the IC, observed ACF, and errors in field j, respectively. We use data at $\theta > 10$" for fitting because at $\theta < 10$" the contribution of the one halo term cannot be ignored. In Figure 5.1, we plot the ACFs of our subsamples with the best-fit power laws.

Then we estimate the spatial correlation function, $\xi(r)$, from the measured ACFs and the redshift distribution of galaxies. The spatial correlation function is usually assumed to be a single power low as

$$\xi(r) = \left(\frac{r}{r_0}\right)^{-\gamma}, \tag{5.7}$$

where r_0 is the correlation length and γ is the slope of the power low. These parameters are related to those of the two point angular correlation function via the Limber transform

(Peebles, 1980; Efstathiou et al., 1991).

$$\beta = \gamma - 1, \tag{5.8}$$

$$A_\omega = \frac{r_0^\gamma B[1/2,(\gamma-1)] \int_0^\infty dz N(z)^2 F(z) D_\theta(z)^{1-\gamma} g(z)}{[\int_0^\infty N(z)dz]^2}, \tag{5.9}$$

$$g(z) = \frac{H_0}{c}(1+z)^2\{1+\Omega_m z + \Omega_\Lambda[(1+z)^{-2}-1]\}^{1/2}, \tag{5.10}$$

where $D_\theta(z)$ is the angular diameter distance, $N(z)$ is the redshift distribution of galaxies, B is the beta function, and $F(z)$ describes the redshift evolution of $\xi(r)$. $F(z)$ is often modeled as $F(z) = [(1+z)/(1+z_c)]^{-(3+\bar{\epsilon})}$ for $\epsilon = -1.2$ (Roche & Eales, 1999), where z_c is the characteristic redshift of galaxies. We assume that the clustering evolution is fixed in comoving coordinates over the redshift range in question.

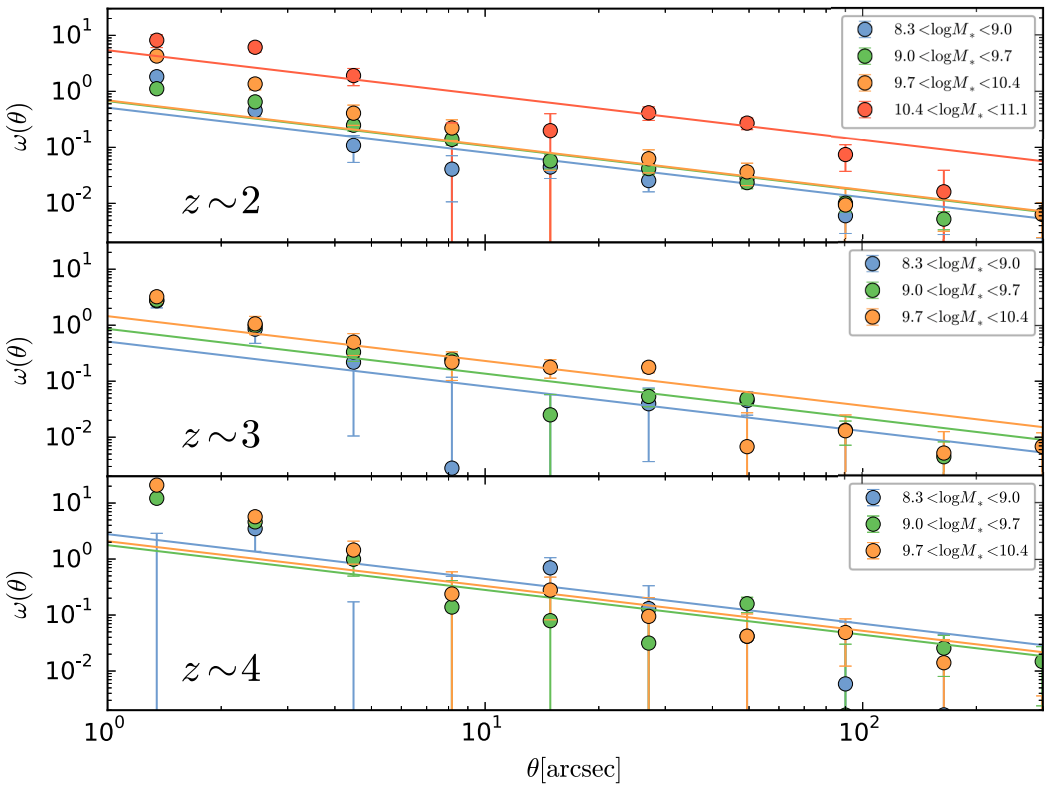

Figure 5.1: ACFs of star-forming galaxies at $z \sim 2-4$ (top to bottom). Data points and the best-fit power laws are color-coded by the stellar mass range.

5.1.2 Galaxy biases and halo masses

To understand the relation between galaxies and hosting dark matter halos we use the halo model of Sheth et al. (2001), which is obtained from the ellipsoidal collapse model. In their model the number density of dark matter halos is given by

$$n(M,z)dM = A\left(1+\frac{1}{\nu'^{2q}}\right)\sqrt{\frac{2}{\pi}}\frac{\overline{\rho}}{M}\frac{d\nu'}{dM}\exp\left(-\frac{\nu'^{2q}}{2}\right)dM, \tag{5.11}$$

where $\nu' = \sqrt{a}\nu$, $a = 0.707$, $A \simeq 0.322$, and $q = 0.3$. Here, ν is defined as

$$\nu = \frac{\delta_c}{\sigma(M,z)} = \frac{\delta_c}{D(z)\sigma(M,0)} \tag{5.12}$$

where $D(z)$ is the linear growth factor, $\sigma(z)$ is the mass rms. of the smoothed density field, and $\delta_c = 1.69$ is the critical amplitude above which overdense regions collapses to form a virialized object. We calculate $D(z)$ by the formula of Carroll et al. (1992) and $\sigma(M, 0)$ using an initial power spectrum of a power law index $n = 1$ and the transfar function of Bardeen et al. (1986). In the model of Sheth et al. (2001) the dark halo bias, b_{DH}, which connects the fluctuation of dark halos and that of the matter density, is given by

$$b_{DH} = 1 + \frac{1}{\delta_c}\left[\nu'^2 + b\nu'^{2(1-c)} - \frac{\nu'^{2c}/\sqrt{a}}{\nu'^{2c} + b(1-c)(1-c/2)}\right], \tag{5.13}$$

where $b = 0.5$ and $c = 0.6$. Then we define the linear galaxy bias, which is the relation between the clustering amplitude of galaxies and that of dark matter halos, at a large scale ($= 8h_{100}^{-1}$ Mpc) as

$$b_g = \sqrt{\frac{\xi_g(r = 8h_{100}^{-1}\ \mathrm{Mpc})}{\xi_{DM}(r = 8h_{100}^{-1}\ \mathrm{Mpc})}} = \sqrt{\frac{[8h_{100}^{-1}\ \mathrm{Mpc}/\mathrm{r}_0]^{-\gamma}}{\xi_{DM}(r = 8h_{100}^{-1}\ \mathrm{Mpc})}}, \tag{5.14}$$

where $\xi_{DM}(r = 8h_{100}^{-1}$ Mpc) is the dark matter spatial correlation function. We calculate $\xi_{DM}(r = 8h_{100}^{-1}$ Mpc) using the non-linear model of Smith et al. (2003). Assuming that the galaxy bias at large scales is almost the same as the halo bias ($b_g \simeq b_{DH}$), we obtain an estimate of dark halo masses. The correlation length and the estimated halo masses are summerized in Table 5.1.

5.2 Abundance Matching

In order to reinforce the results of the clustering analysis, we also use abundance matching analysis, which connects the number density of galaxies to that of dark halos to estimate the hosting dark halo mass for a given stellar mass. We adopt the abundance matching result of Behroozi et al. (2013). Many researchers that study the angular momentum retention factor adopt the abundance matching analysis of Dutton et al. (2010) and Behroozi et al. (2013) to estimate halo masses (e.g. Romanowsky & Fall, 2012; Burkert et al., 2016). This makes easy to compare our results with previous results of angular momentum studies. The estimated halo masses are also summerized in Table 5.1.

Figure 5.2 shows a comparison of the estimated dark matter halo masses. The estimated dark matter halo masses by the two independent methods are consistent within the error bars except for the highest stellar mass bins at $z \sim 2$. This makes the results of the clustering analysis more plausible. In the following Section, we display the results based on the both methods.

Table 5.1: Summary of the clustering analysis and the abundance matching analysis

z	$\log(M_\star/M_\odot)$[a]	N	$A_\omega[\mathrm{arcsec}^{0.8}]$	$r_0[h^{-1}\mathrm{Mpc}]$	$\log M_{\mathrm{dh,CL}}$[b]	$\log M_{\mathrm{dh,AM}}$[c]
2.0	10.58	264	$5.40^{+0.96}_{-0.96}$	$12.30^{+1.18}_{-1.25}$	$13.37^{+0.10}_{-0.12}$	12.23
	9.94	1086	$0.69^{+0.25}_{-0.25}$	$3.92^{+0.73}_{-0.87}$	$11.69^{+0.32}_{-0.56}$	11.79
	9.30	3267	$0.67^{+0.07}_{-0.07}$	$3.86^{+0.21}_{-0.23}$	$11.66^{+0.11}_{-0.13}$	11.51
	8.72	3173	$0.51^{+0.08}_{-0.08}$	$3.31^{+0.28}_{-0.30}$	$11.32^{+0.18}_{-0.23}$	11.30
3.0	9.93	805	$1.45^{+0.31}_{-0.31}$	$5.18^{+0.58}_{-0.65}$	$11.92^{+0.17}_{-0.23}$	11.81
	9.37	1596	$0.86^{+0.15}_{-0.15}$	$3.87^{+0.36}_{-0.39}$	$11.40^{+0.17}_{-0.21}$	11.53
	8.78	838	$0.51^{+0.31}_{-0.31}$	$2.90^{+0.87}_{-1.18}$	$10.79^{+0.56}_{-1.60}$	11.29
4.0	10.01	273	$2.08^{+0.93}_{-0.93}$	$5.57^{+1.27}_{-1.56}$	$11.79^{+0.31}_{-0.56}$	11.78
	9.37	348	$1.77^{+0.72}_{-0.72}$	$5.09^{+1.06}_{-1.28}$	$11.64^{+0.30}_{-0.51}$	11.45
	8.82	133	$2.78^{+1.74}_{-1.74}$	$6.54^{+2.03}_{-2.75}$	$12.03^{+0.38}_{-0.91}$	11.22

[a] Median stellar mass.

[b] Dark matter halo masses estimated by using clustering analysis.

[c] Dark matter halo masses estimated by using the abundance matching technique of Behroozi et al. (2013). We extrapolate the result of Behroozi et al. (2013) to obtain the dark matter halo masses of the lowest stellar mass bins at $z \sim 3$ and 4.

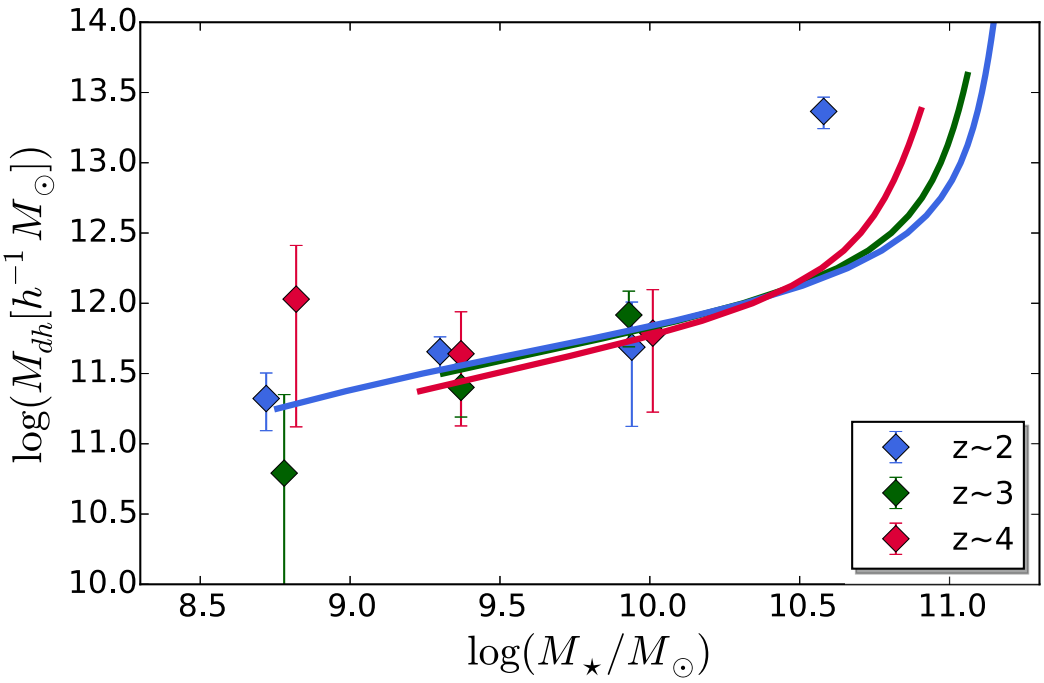

Figure 5.2: Dark matter halo mass as a function of stellar mass obtained from clustering analysis and abundance matching technique at $z \sim 2$, 3, and 4. The colored symbols indicate the results of clustering analysis, while the solid lines indicate the results of the abundance matching of Behroozi et al. (2013).

Chapter 6

Angular momentum

6.1 Estimation of the specific angular momentum

In this Section, we briefly explain the way to estimate the disk specific angular momentum. As already mentioned in Chapter 1, the disk size of a galaxy reflects its specific angular momentum. According to the model of Mo et al. (1998), the specific angular momentum of disk galaxies with an exponential profile ($n = 1$) for a singular isothermal sphere is given by:

$$j_{\rm d} = \frac{\sqrt{2}}{1.678} r_{\rm d} m_{\rm d} \lambda^{-1} r_{200}^{-1}. \tag{6.1}$$

If we assume $r_{\rm d}$ as the half-light radius of a Sérsic index n, we can expand this equation. A Sérsic profile is defined as

$$\Sigma(r) = \Sigma_0(r) \exp\left[-\kappa \left(\frac{r}{r_d}\right)^{1/n}\right], \tag{6.2}$$

where $\Sigma(r)$, $\Sigma_0(r)$, and κ are the surface density profile, the surface density at $r = 0$, and the conversion factor from the scale radius to the half-right radius, respectively. The conversion factor κ is well approximated by

$$\kappa = 2n - \frac{1}{3} + \frac{4}{405n} + \frac{46}{25525n^2} + \frac{131}{1148175n^3} + \mathcal{O}(n^{-4}) \ (n > 0.36), \tag{6.3}$$

$$\kappa = 0.01945 - 0.8902n + 10.95n^2 - 19.67n^3 + 13.43n^4 \ (n < 0.36) \tag{6.4}$$

(Ciotti & Bertin, 1999; MacArthur et al., 2003). The surface density profile is related with the disk mass (M_d) and the disk angular momentum (J_d) as

$$M_d = 2\pi \int_0^\infty r\Sigma(r)dr, \tag{6.5}$$

$$= \frac{2\pi}{\kappa^{2n}} r_d^2 \Sigma_0 n\Gamma(2n), \tag{6.6}$$

$$J_d = 2\pi \int_0^\infty V_c r^2 \Sigma(r)dr, \tag{6.7}$$

$$= \frac{2\pi}{\kappa^{n}} r_d^3 \Sigma_0 V_c n\Gamma(3n), \tag{6.8}$$

$$= \frac{\Gamma(3n)}{\Gamma(2n)\kappa^n} M_d r_d V_c, \tag{6.9}$$

where V_c is the circular velocity, Γ is the gamma function. By using Equation (1.1) and Equation (6.9) and writing $M_d = m_d M_{\rm dh}$ and $J_d = j_d J_{\rm dh}$ we get

$$r_d = \frac{\Gamma(2n)\kappa^n}{\Gamma(3n)} \frac{\lambda G M_{\rm dh}^{3/2}}{V_c |E|^{1/2}} \left(\frac{j_d}{m_d}\right). \tag{6.10}$$

The total energy of a singular isothermal sphere is obtained from the virial theorem

$$E = -\frac{M_{\rm dh} V_c^2}{2}. \tag{6.11}$$

The halo mass for a singular isothermal sphere is related with r_{200} as

$$M_{\rm dh} = \frac{V_c^2 r_{200}}{G}. \tag{6.12}$$

On inserting Equation (6.11) and (6.12) into Equation (6.10) we can get

$$j_{\rm d} = f_n(n)^{-1} r_{\rm d} m_{\rm d} \lambda^{-1} r_{200}^{-1}, \tag{6.13}$$

$$f_n(n) = \frac{\sqrt{2}\Gamma(2n)\kappa^n}{\Gamma(3n)}. \tag{6.14}$$

For a NFW profile, Equation (6.13) can be expanded to

$$j_{\rm d} = f_n(n)^{-1} r_{\rm d} m_{\rm d} \lambda^{-1} r_{200}^{-1} f_{\rm c}(c_{\rm vir})^{1/2} f_{\rm R}(\lambda, c_{\rm vir}, m_{\rm d}, j_{\rm d})^{-1}. \tag{6.15}$$

The full functional forms of $f_{\rm c}$ and $f_{\rm R}$ are given in Mo et al. (1998). The values of λ and $c_{\rm vir}$ are well determined by N-body simulations (Vitvitska et al., 2002; Davis & Natarajan, 2009; Prada et al., 2012; Rodríguez-Puebla et al., 2016). We adopt $(\lambda, c_{\rm vir}) = (0.035, 4.0)$ throughout the examined redshift range ($z \sim 2-4$). From the dark matter halo masses estimated in Section 5, we can calculate $m_{\rm d}$ and r_{200}, where r_{200} is calculated by

$$r_{200} = \left(\frac{G M_{\rm dh}}{100 H(z)^2}\right)^{1/3}. \tag{6.16}$$

Combined with n and $r_{\rm d}$ measured in Sections 3 and 4, we can estimate $j_{\rm d}$ from Equation 6.15. The normalized correction values ($f_n(n)^{-1}/f_n(1)^{-1}$) are summarized in Table 3.1.

6.2 Mass–angular momentum relation

6.2.1 Average $j_{\rm d}/m_{\rm d}$ ratio and its evolution

Figure 6.1 shows the angular momentum retention factor of star-forming galaxies as a function of hosting halo mass. We find $j_\star/m_\star = 0.77 \pm 0.06$ from clustering analysis and $j_\star/m_\star = 0.83 \pm 0.13$ from abundance matching at $z \sim 2$, 3, and 4. No strong redshift evolution is confirmed. As we mention in Section 1, $j_\star/m_\star = 1$ means that the angular momentum is fully conserved and $j_\star/m_\star < 1$ means that galaxies lose their specific angular momentum during their formation and evolution.

Romanowsky & Fall (2012) and Fall & Romanowsky (2013) have investigated kinematical structure for about 100 bright early and late-type galaxies at $z \sim 0$. They have found that late-type galaxies typically have $j_{\rm d}/m_{\rm d} \simeq 0.8$ and early-type galaxies have $j_{\rm d}/m_{\rm d} \simeq 0.1$. A small $j_{\rm d}/m_{\rm d}$ value has also been reported by Dutton & van den Bosch (2012). They have calculated angular momentum retention factor as a function of halo mass by constructing the mass models (Dutton et al., 2011) tuned to observed scaling relations for SDSS galaxies. They have obtained a constant value $j_{\rm d}/m_{\rm d} = 0.61^{+0.13}_{-0.11}$ with halo masses $10^{11.3} M_\odot \lesssim M_{\rm dh} \lesssim 10^{12.7} M_\odot$. Our values at $z \sim 2$, 3, and 4 are in agreement with these local values for late-type galaxies within errors.

There exist a few studies that have investigated the mass–angular momentum relation at high redshifts. Recently, Burkert et al. (2016) have investigated the relation for ~ 360 star-forming galaxies at $z \sim 0.8 - 2.6$, among which about 100 are at $z \sim 2$, by Hα kinematics based on KMOS and SINS/zC-SINF surveys. They have found $j_{\rm d}/m_{\rm d} = 1.0$ with a statistical uncertainty of ± 0.1 and a systematic uncertainty of ± 0.5. This j_d/m_d value is consistent with our result at $z \sim 2$.

We then compare our results with those of Huang et al. (2017) and Somerville et al. (2018). These authors have derived disk size to halo size ratios ($r_{\rm d}/r_{\rm dh}$) as a function of stellar mass over $z \sim 0$ and 3 using the CANDELS data and mapping stellar masses to halo masses with abundance matching. At $z \sim 2$, the $r_{\rm d}/r_{\rm dh}$ ratios obtained by Huang et al. (2017) are consistent with ours, with values of ~ 0.03 in the stellar mass range $10^9 M_\odot < M_\star < 10^{10.5} M_\odot$. We note that our method is very similar to theirs. Their definitions of disk sizes and halo sizes are the same as ours. They have used four abundance matching results including that of Behroozi et al. (2013) which we also use. On the other hand, Somerville et al. (2018) have obtained somewhat higher ratios of $r_{\rm d}/r_{\rm dh} \simeq 0.4$. They have adopted a different halo definition and also taken a different method to link stellar masses to halo masses; they have carried out "forward modeling"

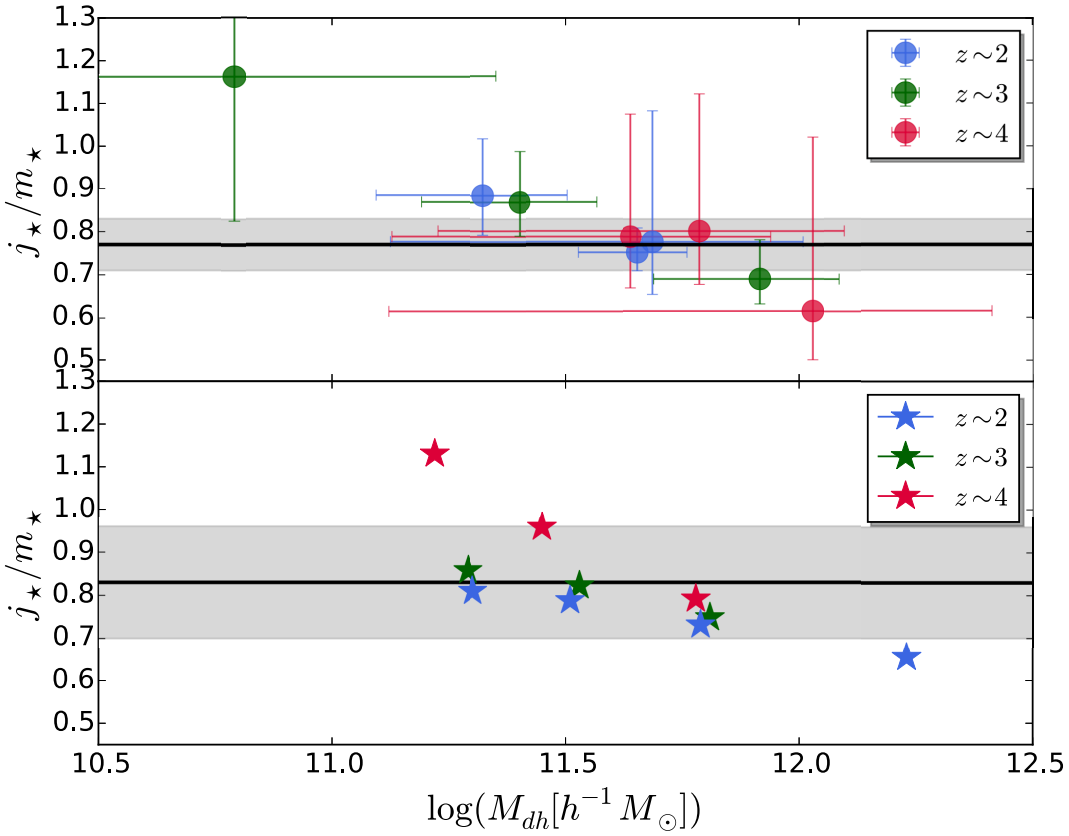

Figure 6.1: Angular momentum retention factor $j_\star/m_\star$ vs. $M_{\rm dh}$ for $z \sim 2$, 3, and 4. The colored symbols in the top panel and the bottom panel indicate the results of clustering analysis and the results of abundance matching analysis, respectively. For each panel, the black solid line and the gray shaded region indicate the average of all estimates and its 1σ error, respectively.

where halos are taken from an N-body simulation and are assigned to stellar masses taking account of a random scatter. These differences may be a cause of the inconsistency in $r_{\rm d}/r_{\rm dh}$ estimates.

To connect our study to those for low redshifts, we use Extended Press-Schechter (EPS) formalism (Bond et al., 1991; Bower, 1991; Lacey & Cole, 1993). The EPS formalism is able to calculate the conditional probability mass function ($f(M_2|M_1)$) of $z = z_2$ descendant halos for a given halo mass (M_1) at a high-redshift (z_1) universe by following their

merger histories. We set $M_1 = 5.0 \times 10^{11} h^{-1} M_\odot$ and $z_1 = 3.0$ to follow the evolution of our halos. The lower 68 and upper percentiles of $f(M_2|M_1)$ at $z_2 = 0$ are $2.0 \times 10^{12} h^{-1} M_\odot$ and $5.6 \times 10^{12} h^{-1} M_\odot$, respectively. This implies that some fraction of our galaxies are the progenitors of objects in the Dutton & van den Bosch (2012) sample in terms of mass growth. From the results we obtain, we can depict a unified view of the angular momentum evolution. Figure 6.2 shows the angular momentum evolution of disk galaxies and comparison with some observations (top) and galaxy formation simulations (bottom). As shown in the top panel of Figure 6.2, observed disk galaxies maintain high $j_\mathrm{d}/m_\mathrm{d}$ values ($\sim 0.6 - 1.0$) during their evolution from cosmic noon to the present day, unless they lose angular momenta by some mechanisms like mergers and turn into early-type galaxies (Romanowsky & Fall, 2012). One the other hand, galaxy formation simulations predict a variety of $j_\mathrm{d}/m_\mathrm{d}$ values ($\sim 0.1 - 1.0$) at $z \sim 2$. We will present a detailed comparison with those galaxy formation simulations in Section 6.3. We note that although our samples can be connected with those of Dutton & van den Bosch (2012) in terms of mass growth, the sample selection is not unified with the previous studies shown in Figure 6.2. We also note that the progenitor-descendant connection based on halo mass is a simplified argument. In reality, this connection involves galaxy halo bias and some galaxy properties in a complex way. For example, Genel et al. (2014) have reported that galaxies in a small stellar mass range at $z \sim 2$ evolve into galaxies with diverse masses due to differences in SFR.

6.2.2 Halo mass dependence of $j_\mathrm{d}/m_\mathrm{d}$ and the slope of the size–stellar mass relation

When we introduce the disk size–halo mass relation in Equation (4.7), we assume that r_d/r_{200} is constant, which means that $j_\star/m_\star$ is constant irrespective of z and M_dh. However, it appears from Figure 6.1 that $j_\star/m_\star$ weakly depends on both M_dh and z. Similar dependencies have also been shown in Huang et al. (2017) and Somerville et al. (2018): $r_\mathrm{d}/r_\mathrm{dh}$ weakly depends on both M_dh and z. We approximate the observed $j_\star/m_\star$–M_dh relation at each redshift by a power law, $j_\star/m_\star \propto M_\mathrm{dh}^{\gamma_z}$. We find $\gamma_z = -0.09 \pm 0.02$ for $z \sim 2$, $\gamma_z = -0.13 \pm 0.01$ for $z \sim 3$, and $\gamma_z = -0.29 \pm 0.02$ for $z \sim 4$. A negative slope of $\gamma_z = -0.19 \pm 0.04$ has also been obtained by Burkert et al. (2016) for $z \sim 0.8 - 2.6$ galaxies. With a non-zero slope γ_z, Equation (4.7) is replaced by:

$$r_\mathrm{d} \propto H(z)^{-2/3} M_\mathrm{dh}^{\gamma_z + 1/3}. \tag{6.17}$$

We also approximate the stellar mass–halo mass relation by a single power-law, $M_\star \propto M_\mathrm{dh}^{\epsilon}$: $\epsilon \simeq 1.6$, from the abundance matching results of Behroozi et al. (2013). By combining

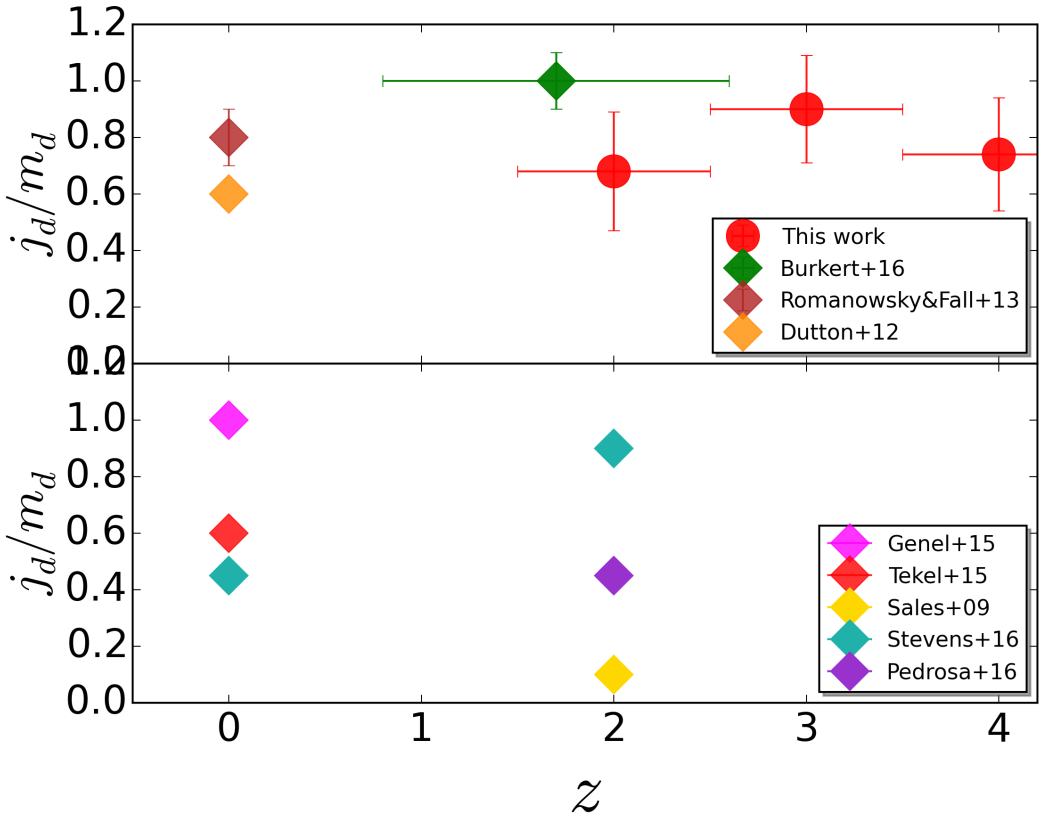

Figure 6.2: Redshift evolution of angular momentum retention factor $j_{\rm d}/m_{\rm d}$ by observations (top) and galaxy formation simulations (bottom). Our results of clustering analysis are shown with red circles, and those from previous studies are shown in colored diamond symbols.

these two relations, we obtain the disk size–stellar mass relation:

$$r_{\rm d} \propto M_\star^{1/3\epsilon+\gamma_z/\epsilon}, \tag{6.18}$$

$$r_{\rm d} \propto M_\star^{0.2+0.6\gamma_z}. \tag{6.19}$$

The slope of the size–stellar mass relation of our galaxies is $\alpha = 0.19^{+0.01}_{-0.01}$ for $z \sim 2$, $0.14^{+0.01}_{-0.03}$ for $z \sim 3$, and $0.08^{+0.05}_{-0.05}$ for $z \sim 4$ (see Section 4.2.2). The result that α is less than 0.2 for all three redshifts is explained by the negative γ_z values obtained above. We also find that the decrease in α from $z \sim 3$ to $z \sim 4$ is due to the decrease in γ_z.

Using a theoretical modified cooling model which includes disc instability, Dutton & van den Bosch (2012) have predicted a slightly negative γ_z for high redshift disk galaxies, in

qualitative agreement with our results. Their negative slope reflects the fact that the mass loading factor decreases with increasing of halo mass. While this model is not consistent with their empirical model at $z \sim 0$, this model may be applicable to high redshifts. The possible decrease in γ_z from $z \sim 3$ to $z \sim 4$ found above may imply that feedback processes also change in this redshift range.

As already seen in Figure 4.5, van der Wel et al. (2014) have reported constant disk size–stellar mass slopes (~ 0.2) since $z \sim 2 - 0$. From the model of Equation (6.19), this implies that the angular momentum–halo mass relations are also flat. This is quite in agreement with the empirical results of Dutton & van den Bosch (2012) at the present-day universe. Thus Equation (6.19) well represents the relation between angular momentum and disk size.

6.3 Comparison with galaxy formation models

As the kinematics of galaxies provides us with important constraints on galaxy formation and evolution as well as do other global properties like stellar mass, star-formation rate, and metallicity, many modelers have attempted to reproduce the kinematic structures of galaxies. Early attempts concerning angular momentum with hydrodynamical simulations were in trouble with reproducing observations. They suffered from unexpected angular momentum loss. In those simulations, most of the angular momentum of galaxies was transferred to the background hosting halos. As a result, compact disk galaxies were produced (e.g. Navarro & Benz, 1991; Navarro & White, 1994). This problem is known as the "angular momentum catastrophe".

This problem has been considerably improved by high-resolution hydrodynamical simulations with a proper treatment of feedback processes (Robertson et al., 2006; Governato et al., 2007; Scannapieco et al., 2008). In recent years, many galaxy formation simulations have succeeded in reproducing the mass–angular momentum relation for both early-type and late-type galaxies in the present-day universe (Genel et al., 2015; Teklu et al., 2015). On the other hand, at high redshifts, there do not exist theoretical studies that compare with observational data. It is still unknown that these simulations are able to reproduce the observed mass–angular momentum relation beyond $z \sim 1$. Here, we first compare our observational angular momentum results with those of some galaxy formation simulations (Sales et al., 2012; Pedrosa & Tissera, 2015; Stevens et al., 2016).

In Figure 6.3, we compare the mass–angular momentum distribution of star-forming galaxies obtained from clustering analysis and abundance matching analysis with predictions from hydrodynamical and semi-analytical galaxy formation models at $z \sim 2$. To

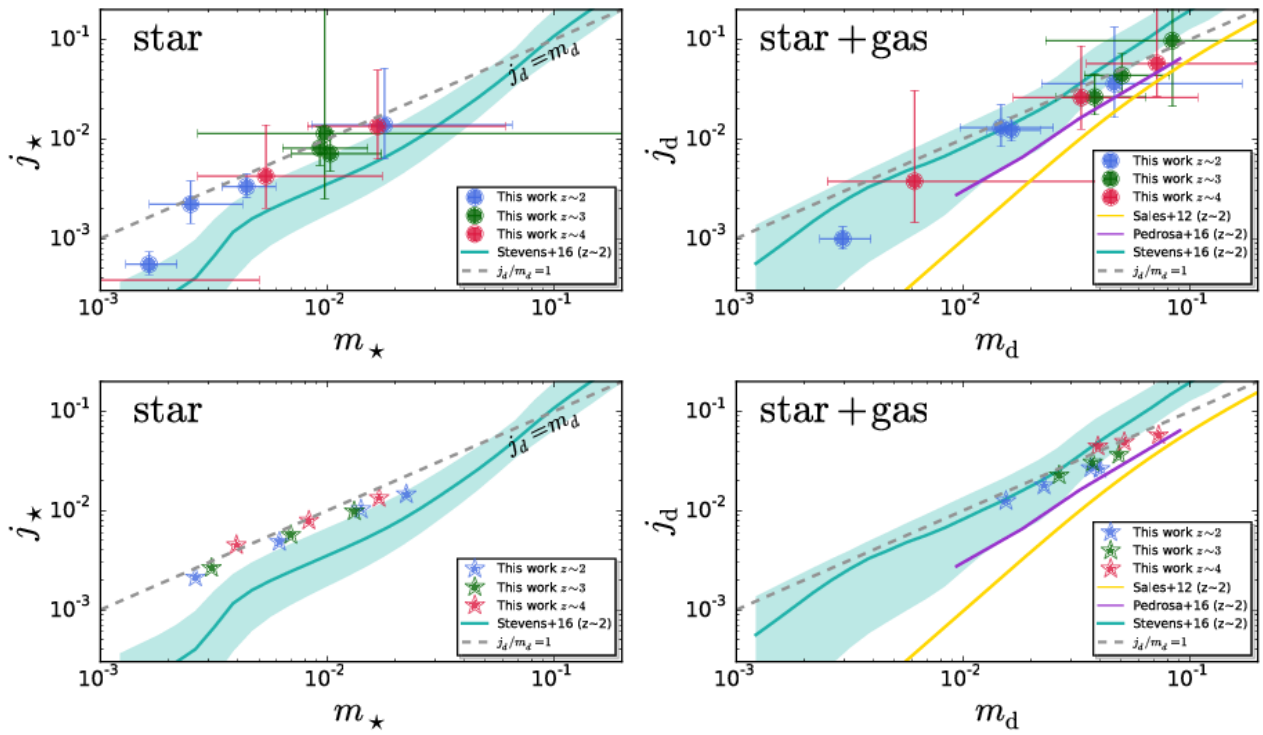

Figure 6.3: Observed mass–angular momentum relation compared with three hydrodynamical and semi-analytic galaxy formation simulations. The left panels show the relation for the stellar component and the right panels for the stellar plus gas component. The colored symbols in the top panels are the results obtained from clustering analysis and those in the bottom panels are from abundance matching analysis. The solid cyan lines indicate the semi-analytical galaxy formation simulation of Stevens et al. (2016) at $z \sim 2$. The solid purple and yellow lines on the right panels indicate the hydrodynamical galaxy formation simulations of Sales et al. (2012) and Pedrosa & Tissera (2015), respectively, at $z \sim 2$. The gray dashed lines indicate the line of angular momentum conservation.

directly compare with two models which give only stellar plus gas properties, we also estimate the entire disk masses by correcting for gas masses using the gas fraction estimates given in Schinnerer et al. (2016). They have investigated the gas masses for 45 massive star-forming galaxies observed with ALMA at redshifts of $z \sim 3 - 4$. We extend their

results to lower mass and lower redshift by the prediction of 2-SFM (2 star formation mode) model (Sargent et al., 2014). We correct $m_\star$ and $j_\star$ by the same factor assuming that the stellar and gas disks have the same j value. The right panel of Figure 6.3 shows the baryonic disk mass–angular momentum relation.

Sales et al. (2012) have presented baryonic mass–angular momentum relations with various types of feedback from large cosmological N-body/gasdynamical simulations at $z \sim 2$. They have found that regardless of the strength of the feedback process m_d vs. j_d follows the same relation (the yellow solid lines in Figure 6.3). When strong feedbacks push out most of the baryons from the galaxies, both m_d and j_d are reduced. Pedrosa & Tissera (2015) have also analyzed the mass–angular momentum relation by decomposing disks and bulges with cosmological hydrodynamical simulations at $z \sim 0 - 2$. They have found no significant evolution since $z \sim 2$ to $z \sim 0$. The relation for total baryonic components at $z \sim 2$ is shown in Figure 6.3.

Stevens et al. (2016) have presented a semi-analytical model Dark Sage, which is designed for specific understanding of angular momentum evolution. They have investigated the evolution of the stellar mass–specific angular momentum relation over $0 < z < 4.8$. The solid cyan lines in Figure 6.3 indicate the predicted mass–angular momentum relation at $z \sim 2$.

All of these simulations other than the model by Stevens et al. (2016) in the star+gas plot predict specific angular momenta systematically smaller than our values from both dark matter halo mass estimation methods. Our relations are almost parallel to the line of angular momentum conservation (dashed gray lines in Figure 6.3) regardless of mass scales, however, the simulations predict smaller specific angular momenta and the deviations are large for smaller $m_\star$ and m_d. While the star+gas plots appear to have smaller deviations than those of the star only plots, note that we ignore a possible difference in the distribution of gases and stars within galaxies. In other words, we assume that gases and stars have the same specific angular momentum. However, Brook et al. (2011) have shown that the angular momentum distributions of stars and $\mathrm{H_I}$ gases are different, with $\mathrm{H_I}$ gases having a tail of high angular momentum. Indeed, extended $\mathrm{H_I}$ gas disks are found in intermediate (Puech et al., 2010) and high redshift (Daddi et al., 2010) galaxies. Gases beyond star-forming regions serve as a high angular momentum reservoir (Brook et al., 2011). These gases should have a larger specific angular momentum than stars. In this case, the gaps on the right panels in Figure 6.3 become larger.

These deviations imply that it is not trivial for galaxy formation simulations to produce large disk sizes at high redshifts. Some mechanisms that increase disk specific angular momentum at high redshifts may be needed. For example, selective ejection of low angular

momentum material from galaxies leads to a redistribution of angular momentum (Brook et al., 2012; Governato et al., 2012). This explains the difference in the distribution of angular momentum between dark matter halos and visible galaxies: dark matter halos have a large low angular momentum tail, while observed galaxies do not. This process reproduces large bulge-less high angular momentum galaxies.

Whether or not these feedback related mechanisms are enough to solve the deviations seen in Figure 6.3 is still unknown. More detailed observations and simulations are needed.

6.4 Disk instability

The angular momentum of disks is also closely related to their global instabilities. Disks can be unstable against bar mode instability, because low angular momentum material forms a bar (Shen et al., 2003). Efstathiou et al. (1982) have investigated this kind of instabilities for a exponential disk embedded in a variety of halos using N-body simulations and found a stellar disk is globally unstable against bar formation under the criterion:

$$\epsilon_{\rm m} \equiv \frac{V_{\rm max}}{(GM_{\rm d}/r_{\rm d})^{1/2}} \lesssim 1.1, \tag{6.20}$$

where $V_{\rm max}$ is the maximum rotation velocity of the disk. The threshold for gaseous disks is $\epsilon_{\rm m} \simeq 0.9$. According to Mo et al. (1998), for a NFW halo, this criterion is well approximated by

$$\lambda' < m_{\rm d}, \tag{6.21}$$

where $\lambda' \equiv \lambda j_{\rm d}/m_{\rm d}$.

We note that the criteria of Equations (6.20) and (6.21) are not strict. Guo et al. (2011) have proposed an alternative criterion, $V_{\rm max} < \sqrt{GM_{\rm d}/3r_{\rm d}}$, which reflects that $V_{\rm max}$ of the real dark matter halo systems is smaller than that of ideal systems. In this paper, we use Equation (6.21).

We show in Figure 6.4 the distribution in the λ'–$m_{\rm d}$ plane of our star-forming galaxies over $z \sim 2-4$. We find most of the data points to be near the line of instability over the entire redshift range regardless of the method to estimate dark halo masses. This implies some fractions of $z \sim 2-4$ galaxies may be dynamically changing the disk structure toward forming a bar and a bulge through bar formation.

To compare with local spiral galaxies, we assume $\lambda = 0.04$ and $j_{\rm d}/m_{\rm d} \simeq 0.8$ (Fall & Romanowsky, 2013) in the present-day Universe. Then, the average value of λ' is estimated as 0.032. The abundance matching result of Behroozi et al. (2013) predicts $m_{\rm d}$ lower than 0.032 in a wide range of halo mass. This displays that local spiral galaxies appear to be more stable than high redshift galaxies.

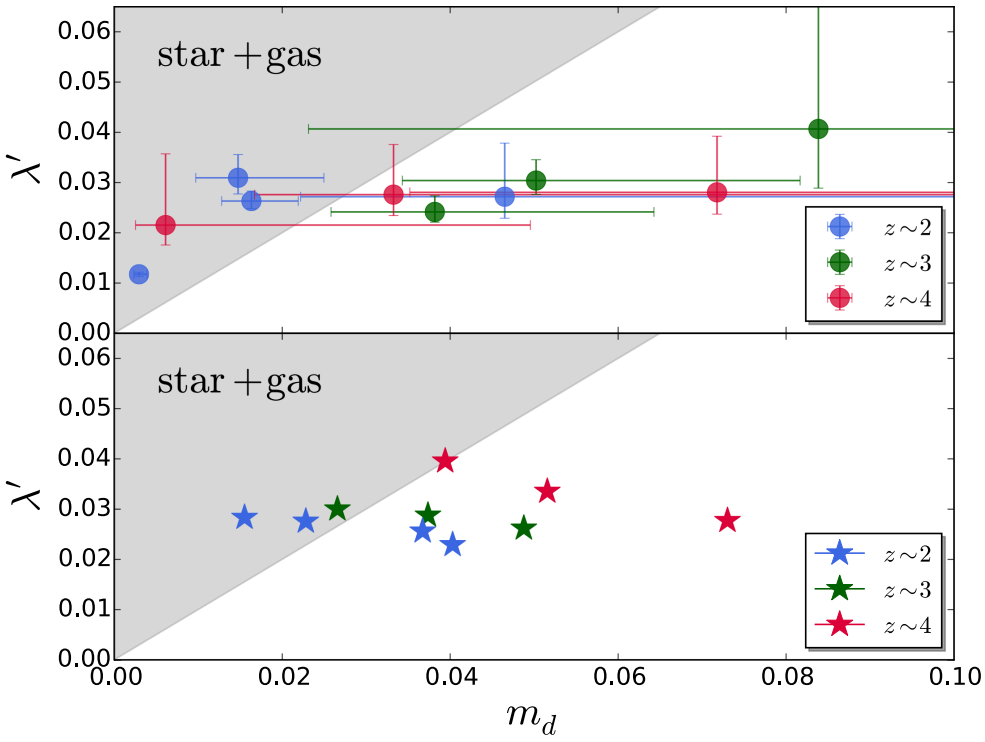

Figure 6.4: Diagram of λ' vs. $m_{\rm d}$ at $z \sim 2$, 3, and 4. The colored symbols in the top panel and the bottom panel indicate results from clustering analysis and abundance matching analysis, respectively. Galaxies in the gray shaded regions are unstable against bar-mode instability.

We have to keep in mind again that we should take into account a possible difference in angular momentum between gases and stars mentioned in Section 6.3. In this case, the plots in Figure 6.4 will move to more stable regions.

Other than the global instability, there exist scenarios that form bars and bulges (Mo et al., 2010). For example, an interaction with a massive perturber leads to a bar-like structure (Noguchi, 1987). In addition to this, the migration of giant clumps, which are created by local Toomre Q instabilities (Toomre, 1964), grows a bulge. Global instability may be one of the ways to explain galaxies with bars or bulges in the local Universe.

Chapter 7

Zoom-in Simulation

In this Chapter, we describe the detail of our cosmological zoom-in simulations.

7.1 Simulation Setup

We use a numerical framework from the First Billion Years (FiBY) project (e.g. Johnson et al., 2013; Paardekooper et al., 2013; Agarwal & Khochfar, 2015) for our simulations presented in this thesis, which is a modified version of the Tree-PM SPH code GADGET-3 (Springel, 2005). The modifications include updates to pop3-SF and non-equilibrium primordial chemistry and an update of the dust formation law, which is intended to investigate specific physics relevant for the galaxy formation in the high-redshift Universe (Johnson et al. 2013). The overall effect of the modifications has been studied in a suite of the FiBY project. The FiBY reproduces the observed mass function and star formation rates of galaxies at $z \geq 6$ (Khochfar et al., in preparation), the metallicity evolution (Dalla Vecchia et al., in preparation), and other general properties of high-redshift galaxies (e.g., Cullen et al., 2017; Arata et al., 2019).

We run the simulations from $z \sim 100$ to $z \sim 6$. The initial conditions are generated with `MUSIC` code (Hahn & Abel, 2011). The `MUSIC` generates the positions and velocities of DM and gas particles following Lagrangian cosmological perturbation theory up to the second-order within a specified comoving volume.

First, we carry out dark-matter only coarser resolution simulations of a $(250\mathrm{Mpc})^3$ comoving volume with 256^3 DM particles to define zoom-in regions. Halos and sub-halos are identified by the Friends-of-Friends (FOF) algorithm. For the zoom-in simulations, we are required to select halos large enough ($> 10^{12}\,h^{-1}M_{\odot}$) to expectedly host bright galaxies that can be detected in the following mock observations. In order to make several large halos, the $(250\mathrm{Mpc})^3$ comoving volume are needed according to the halo mass function at $z \sim 6$ (e.g., Press & Schechter, 1974; Angulo & White, 2010). We

Table 7.1: Parameters of our cosmological zoom-in simulations

halo ID	$M_{\rm h}[h^{-1}M_\odot]$ [a]	$m_{\rm DM}[h^{-1}M_\odot]$ [b]	$m_{\rm gas}[h^{-1}M_\odot]$ [c]	$\epsilon_{\rm min}[h^{-1}{\rm pc}]$ [d]	A
1	3.3×10^{12}	2.0×10^{6}	3.5×10^{5}	200	2.5×10^{-3}
2	2.7×10^{12}	2.0×10^{6}	3.5×10^{5}	200	2.5×10^{-3}

[a] Halo mass at $z\sim6$.

[b] Mass of a dark matter particle.

[c] Initial mass of a gas particle.

[d] Gravitational softening length.

[e] Amplitude factor for the star formation model based on the Kennicutt-Schmidt law.

select two halos whose masses are $3.3\times10^{12}\,h^{-1}M_\odot$ and $2.7\times10^{12}\,h^{-1}M_\odot$. We call them halo1 and halo2, respectively. The DM particles of the halos and the surrounding regions are traced back to the initial conditions for zoom-in simulations. The defined zoom-in regions are distributed with baryons at much higher resolutions. Then, we simulate the entire volume again. For all halos, the effective resolution is 8096^3. After the second run, we select sub-halos which include galaxies with a magnitude of $M_{\rm UV}\leq-17$ taking into account the detection limit of the HFF field, where $M_{\rm UV}$ is calculated from UV flux density as detailed in Section 7.5. Finally, we select 27 galaxies at $z\sim6$: 17 galaxies from halo1 and 10 galaxies from halo2. The gravitational softening length is set to $200\,h^{-1}$Mpc in the comoving unit, which corresponds to $\sim40\,$pkpc at $z\sim6$. This resolution makes it possible to investigate the sizes of faint high-redshift galaxies. The adopted stellar IMF for Population II stars is that of Chabrier (2003). The parameters of our halos are shown in Table 7.1.

7.2 Star Formation

The spatially resolved star formation rates of local galaxies follow the Kennicutt-Schmidt (KS) law (Kennicutt, 1998):

$$\dot{\Sigma}_* = A\left(\frac{\Sigma_g}{1{\rm M}_\odot{\rm pc}^{-2}}\right)^n, \tag{7.1}$$

where $\dot{\Sigma}_*$ is the star formation rate per unit area per unit time and Σ_g is the gas surface density. Kennicutt (1998) found $A_{\rm local}\sim1.5\times10^{-4}\,{\rm M}_\odot\,{\rm yr}^{-1}\,{\rm kpc}^{-2}$ and $n\sim1.4$ as the best fit parameters for normal star-sforming galaxies assuming a Saltpeter IMF. Because we are using a Chabrier IMF, the amplitude should be changed by a factor of 1/1.65: $A_{\rm local,Chab}=2.5\times10^{-4}{\rm M}_\odot{\rm yr}^{-1}{\rm kpc}^{-2}$.

In our simulations, the star formation rate is calculated based on an adapted version of the Kennicutt-Schmidt (KS) law, which is proposed by Schaye & Dalla Vecchia (2008). They analytically modified the KS law in terms of volume density and pressure rather than surface density, which enables us to implement the empirical star formation law into simulations:

$$\dot{m}_* = m_g A (1\mathrm{M}_\odot \mathrm{pc}^{-2})^{-\mathrm{n}} \left(\frac{G}{\gamma} f_g P_{\mathrm{tot}} \right), \tag{7.2}$$

where $\dot{m}_*$ is the star formation rate, m_g is the mass of a gas particle, G is the gravitational constant, $\gamma = 5/3$ is the ratio of specific heats, f_g is the gas mass fraction and P_{tot} is the total pressure.

Because high redshift galaxies tend to have much higher star formation rates than local galaxies, we adopt the amplitude A ten times larger than that of local galaxies assuming a Chabrier IMF i.e., $A = 2.5 \times 10^{-3}\,\mathrm{M}_\odot\,\mathrm{yr}^{-1}\,\mathrm{kpc}^{-2}$. As for the threshold density above which star formation occurs, we adopt $n_H = 10\ \mathrm{cm}^{-3}$. We also assume $f_g = 1$ following Schaye (2002).

7.3 Supernova Feedback

It is widely accepted that stars, especially massive stars, distribute a vast amount of energy and momentum into the ISM via supernova feedback. The injected energy and momentum contribute to regulating the subsequent star formation (e.g., Agertz et al., 2011; Hopkins et al., 2011; Aumer et al., 2013). For hydrodynamical simulations, various kinds of sub-grid recipes have been developed. One approach is to turn off cooling (Stinson et al., 2006) and deposit the thermal energy from stars into gases selectively (Murante et al., 2010) or stochastically (Vecchia & Schaye, 2012).

In this work, we implement the thermal supernova (SN) feedback introduced by Vecchia & Schaye (2012). They treat SN feedback as a stochastic thermal distribution as a means to solve the overcooling problem (e.g., Suginohara & Ostriker, 1998; Lewis et al., 2000; Tornatore et al., 2003). The thermal energy released by a single star particle is injected into a nearby SPH particle. The temperature of the SPH particle increases by $\Delta T = 10^{7.5}\mathrm{K}$ with a probability which is determined by the fraction f_{th}. According to Crain et al. (2015), f_{th} depends on the local physical properties: gas metallicity, Z, and gas density $n_{\mathrm{H,birth}}$. The parametrisation is given as

$$f_{\mathrm{th}} = f_{\mathrm{th,min}} + \frac{f_{\mathrm{th,max}} - f_{\mathrm{th,min}}}{1 + \left(\frac{Z}{0.1\,Z_\odot} \right)^{n_Z} + \left(\frac{n_{\mathrm{H,birth}}}{n_{\mathrm{H},0}} \right)^{n_n}}, \tag{7.3}$$

where $f_{\mathrm{th,min}}$ and $f_{\mathrm{th,max}}$ are the asymptotic values of a sigmoid function, $Z_\odot = 0.0127$ is

the solar metallicity (Allende Prieto et al., 2001).

Vecchia & Schaye (2012) estimated the maximum gas density $n_{\mathrm{H,t_c}}$ under which stochastic heating would be effective by comparing the sound crossing time and cooling time for heated resolution elements:

$$n_{\mathrm{H,t_c}} \sim 10\,\mathrm{cm}^{-3} \left(\frac{T}{10^{7.5}\,\mathrm{K}}\right)^{3/2} \left(\frac{m_g}{10^6\,M_\odot}\right)^{-1/2}. \tag{7.4}$$

7.4 Cooling

The cooling rate of gas is based on line-cooling in photoionization or collisional equilibrium for metal elements. FiBY tracks 11 metal elements (H, He, C, N, O, Ne, Mg, Si, S, Ca, and Fe) following Wiersma et al. (2009). All radiative cooling is calculated by using the publicly available photoionization code CLOUDY v07.02 (Ferland et al., 1998).

7.5 Projected Images

Figure 7.1 represents the visualization of the projected gas density of the zoom-in regions for our halos at $z = 6.0$. The gas distribution features a turbulence and filamentary structure. The yardstick represents the scale of 1 h^{-1}Mpc in comoving coordinates.

Figure 7.2 shows the projected gas density map (top left panel), the stellar mass surface density map (bottom left panel), the dust mass surface density map (top right panel), and the surface brightness (bottom right panel) at UV (1500$\mathring{A}$) of the most massive galaxy at $z = 6$. The yardstick represents the scale of 5 kpc in physical coordinates.

We calculate the UV flux density due to star formation taking dust extinction into account. Without dust extinction, the SFR is estimated with equations (3) from Kennicutt (1998):

$$\frac{SFR}{M_\odot \mathrm{yr}^{-1}} = 1.4 \times 10^{-28} \frac{L_\nu}{\mathrm{erg\,s^{-1}\,Hz^{-1}}}. \tag{7.5}$$

As each SPH particle has the information of metallicity, we estimate dust masses assuming that dust mass is proportional to metal mass (Draine et al., 2007). We adopt a constant dust mass to metal mass ratio, $M_{\mathrm{dust}}/M_{\mathrm{metal}} = 0.04$, following Yajima et al. (2015). Dust attenuation is related to dust mass surface density as:

$$A_{\mathrm{UV}} \simeq 1.5 \times \frac{\Sigma_{\mathrm{dust}}}{10^5\,M_\odot\,\mathrm{kpc}^{-2}}, \tag{7.6}$$

under the assumption of the 'foreground screen' model from Calzetti et al. (1994), the dust model from Draine & Li (2007), and the dust-to-gas ratio from Draine et al. (2014).

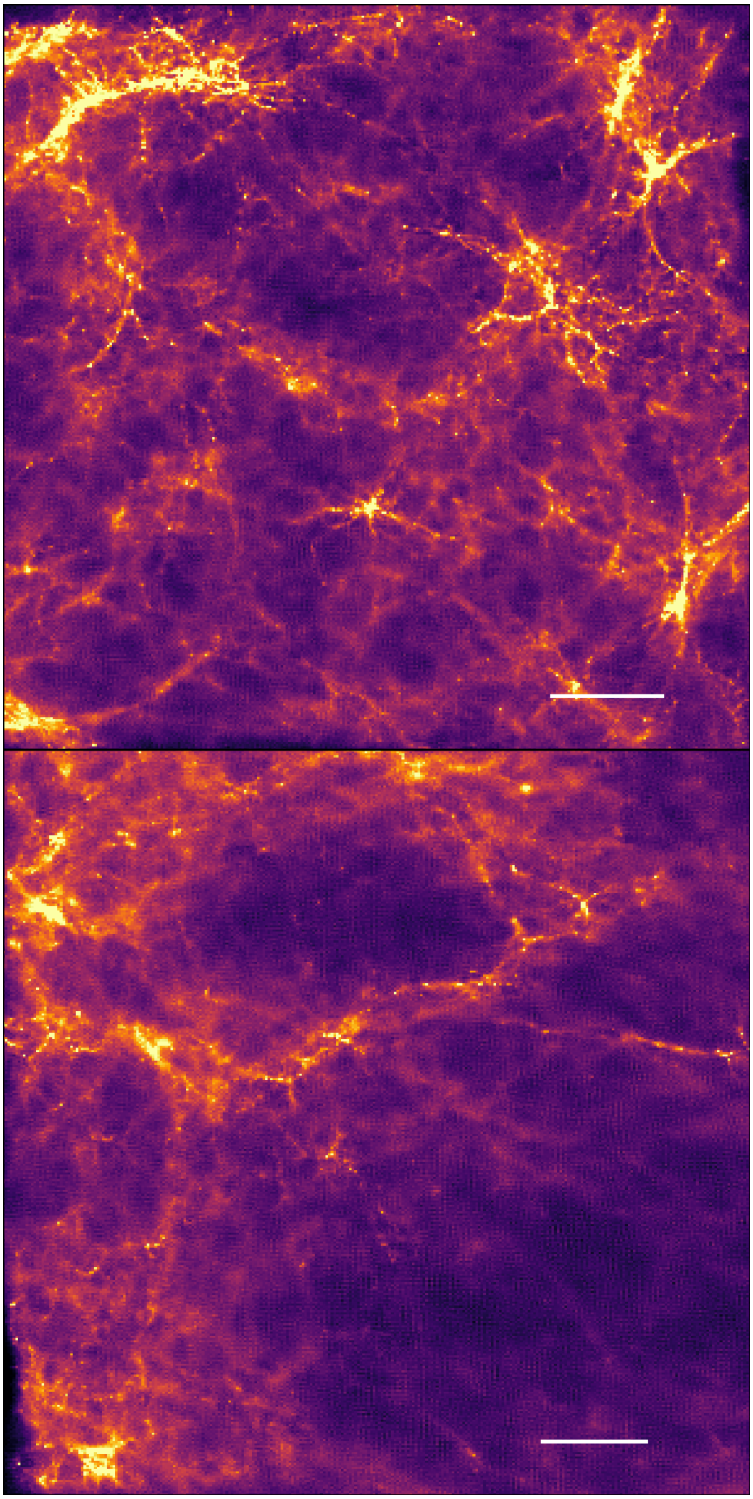

Figure 7.1: Projected gas density for our halos at $z \sim 6$. The white yardstick corresponds to $1\,h^{-1}$Mpc in comoving coordinates.

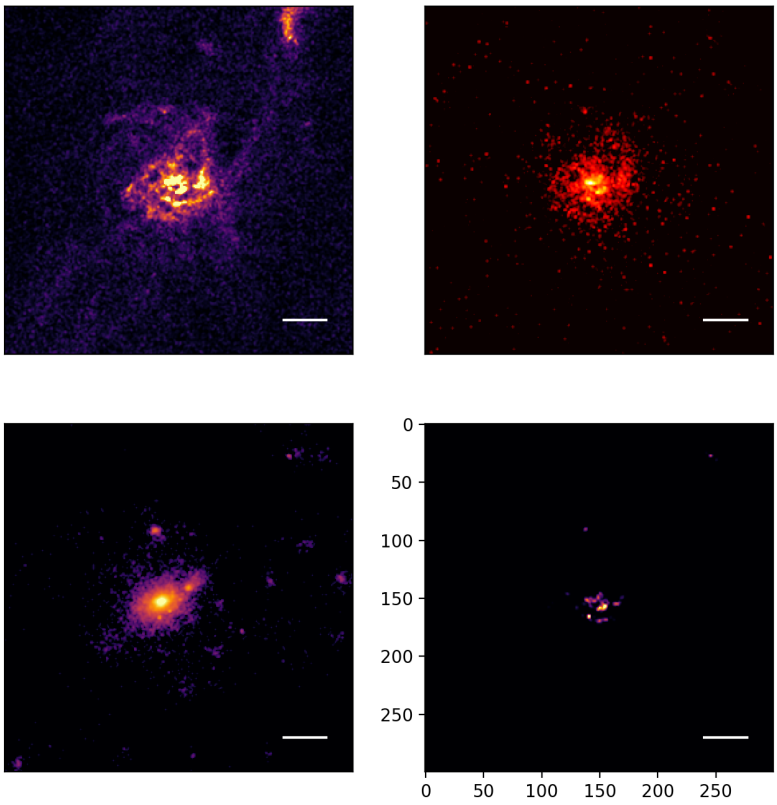

Figure 7.2: Projected gas (top left), dust (top right), stellar (bottom left), UV flux densities (bottom right) of the most massive galaxy. The white yardstick corresponds to 5 kpc in physical coordinates.

Chapter 8

Mock Observations

Here we describe our mock observations for the simulated galaxies. We put the simulated galaxies in the Abell2744 cluster field image mosaic accounting for the gravitational lensing effect and the PSF effect simultaneously (in Section 8.3), and then we measure the sizes of the lensed images with almost the same procedure as in Kawamata et al. (2015, 2018) (in Section 8.4). We introduce two types of definitions of galaxy size: an observed size ($r_{\rm obs,mock}$) in the mock observations and an intrinsic size ($r_{\rm sim}$) in the simulations (in Section 8.5).

8.1 HFF Data

We base our mock observations on the reduced mosaic data in the HFF program, which are released to the public through the STScI website. This program includes the reduced data of the F435W (B_{435}), F606W (V_{606}), F814W (i_{814}), F105W (Y_{105}), F125W (J_{125}), F140W (JH_{140}), and F160W (H_{160}) bands. We only use the Abell 2744 cluster field among the six cluster fields, Abell2744, MACS J0416.1 − 2403, MACS J0717.5+3745, MACS J1149.5+2223, Abell S1063, and Abell 370, and accompanying six parallel fields observed in this program. We base our work on the v1.0 reduction mosaics. We utilize the JJHH combined image, which has been used for the i-dropout selection in Kawamata et al. (2018). This image was created by combining the J_{125}, JH_{140}, and H_{160} images. The 5σ limiting magnitude is ~ 29 mag on a 0".35 diameter aperture. The pixel scale of this image is 0".03.

8.2 Mass Modeling with Glafic

In this thesis the gravitational lensing equation is solved with the public software `glafic` v1.2.8 (Oguri, 2010), which has been widely used for mass modeling of cluster fields (e.g.,

Oguri et al., 2012, 2013; Köhlinger & Schmidt, 2014; Ishigaki et al., 2015; Petrushevska et al., 2018). We utilize the mass model for the Abell2744 cluster field constructed in Kawamata et al. (2016, 2018). The details of the mass modeling are described in Kawamata et al. (2016, 2018), but we give a brief summary below.

The `glafic` constructs mass models with three mass components: cluster-scale halos, cluster member galaxy halos, and external perturbation. The cluster-scale halos are modeled by the NFW profiles (Navarro et al., 1997). The profiles of NFW are given as

$$\rho(r) = \frac{\rho_s}{(r/r_s)(1+r/r_s)^2}, \tag{8.1}$$

where ρ_s is the characteristic density and r_s is the scale radius. The scale radius is defined with the concentration parameter (c) by

$$r_s = \frac{r_{\rm vir}}{c}, \tag{8.2}$$

where $r_{\rm vir}$ is the virial radius of the cluster-scale halo. The scale radius and the characteristic density are related to the virial mass ($M_{\rm vir}$) and the concentration parameter with the following relation:

$$r_s = \frac{r_{\rm vir}}{c} = \left[\frac{3M_{\rm vir}}{4\pi\Delta(z)\overline{\rho}(z)}\right]^{1/3}\frac{1}{c}, \tag{8.3}$$

$$\rho_s = \frac{\Delta(z)\overline{\rho}(z)c^3}{3m_{\rm nfw}(c)}, \tag{8.4}$$

$$m_{\rm nfw}(c) = \int_0^c \frac{r}{(1+r)^2}dr = \ln(1+c) - \frac{c}{1+c}, \tag{8.5}$$

where $\Delta(z)$ is the nonlinear overdensity and the mean matter density of the universe at redshift z. The cluster-scale halos have four free parameters: $M_{\rm vir}$, c, ellipticity, and position angle. For the Abell2744 cluster field, three NFW profiles are placed on the bright galaxies in the core of the cluster.

The cluster member galaxy halos are modeled by pseudo-Jaffe ellipsoids (Keeton, 2001). In this model, the mass profile of galaxies is determined by the velocity dispersion (σ) and the truncation radius ($r_{\rm turn}$). The velocity dispersion and truncation radius are calculated using the following scaling relations:

$$\frac{\sigma}{\sigma_*} = \left(\frac{L}{L_*}\right)^{1/4}, \tag{8.6}$$

$$\frac{r_{\rm turn}}{r_{\rm turn,*}} = \left(\frac{L}{L_*}\right)^{\eta}, \tag{8.7}$$

where L_* is the normalization luminosity, which is set to $i_{814} = 18.33$ for the Abell2744 cluster field, and σ_*, $r_{\rm turn}$, and η are treated as free parameters. The luminosity L, ellipticity, and position angle of each galaxy are measured in the i_{814} band.

External perturbation is included in order to improve mass modeling. The perturbation is described by (e.g., Kochanek, 1991)

$$\phi = \frac{C}{m} r^n \cos m(\theta - \theta_*), \tag{8.8}$$

where C is the expansion coefficient, θ is the angular coordinate, θ_* is the position angle, and r is the distance from the brightest cluster galaxy. For the Abell2744 cluster field, the second ($n = 2, m = 2$) and the third ($n = 3, m = 3$) order term are modeled.

The parameters of these components have been constrained in order to reproduce the positions and the photometric redshifts of lensed multiple images. The multiple images have been identified in Merten et al. (2011), Atek et al. (2014), Richard et al. (2014), Zitrin et al. (2014), Lam et al. (2014), Ishigaki et al. (2015), Jauzac et al. (2015), and Mahler et al. (2018). The positions and redshifts of 132 multiple images of 45 systems have been used.

In this thesis `glafic` is used for two purposes. One is that we calculate the images on the image plane from the simulated galaxies on the source plane (in Section 8.3). The other is that we measure the galaxy sizes on the source plane by fitting the lensed simulated images with a lensed Sérsic profile (in Section 8.4).

8.3 Lensing onto the JJHH Image

We lens the projected UV surface density images simulated in Chapter 7 onto the JJHH image. The procedure is as follows. First, on the source plane, we create count maps, whose count scales are matched to that of the JJHH image, from the projected UV surface density images. We calculate pixel counts from UV flux densities by using PHOTFLAM for the Abell2744 cluster field, i.e., $f_\lambda = \mathrm{PHOTFLAM} \times \mathrm{COUNT}$, where f_λ is the flux density in units of $\mathrm{erg\,s^{-1}\,cm^{-2}\,\AA^{-1}}$ and $\mathrm{PHOTFLAM} = 3.0386574 \times 10^{-20}$. Given that the pixel scale of the JJHH image is several times coarser than that of the projected UV surface density images, we adjust the latter to the former by increasing the pixel scale to 0".03. Then we calculate the gravitational lensing effect for tophat sources with a radius (r_{tophat}), which is placed as an alternative of each pixel. Although `glafic` can lens some parametric profiles such as a tophat profile or a Sérsic profile onto the image plane, there is no means to lens the entire image of a galaxy at once. Among the usable parametric profile, we select a tophat profile that would best reproduce the original pixel. We set r_{tophat} to 0".017 so as to have the same area and same total count as the original pixel (0".03). Positions and luminosities on the image plane are calculated, and the lensed image of a galaxy is reproduced as a summation of lensed tophat sources. Finally, we convolve the lensed images with the point-spread function (PSF). Within the Abell2744

cluster field, we select three positions where the lensed images emerge, as shown in Figure 8.1. These positions are determined by the following criteria: appropriate magnification factor ($\mu = 3 \sim 5$) and not the vicinity of bright stars or galaxies. By using several positions, we avoid a systematic error by a specific magnification factor and sky noise.

8.4 Size Measurements

Size measurements are conducted in almost the same manner as described in Kawamata et al. (2015, 2018), but we briefly describe them. We make a 3.0" × 3.0" cutout image around a lensed galaxy on the image plane. An ellipsoidal Sérsic profile with a set of initial parameters on the source plane is lensed onto the image plane. This lensed-distorted profile, which is convolved with the PSF, is fitted with a cutout image with the `optimize` command of the `glafic`. The best fit parameter which minimizes χ^2 on the image plane is searched on the parameter space on the source plane. This is a more direct method compared with one in which a galaxy on the image plane is fitted with an unlensed Sérsic profile by using `GALFIT`, and the parametric profile is corrected simply based on the magnification factor. We mask bright neighbors so that they do not disturb the fitting for the galaxies of interest. Six parameters are treated as the free parameters to determine: positions, half-light radius, flux, ellipticity, and position angle. We restrict the upper limit of ellipticity to 0.9. The Sérsic index is fixed to $n = 1$ considering recent size measurements for faint galaxies at $z > 6$ (Bouwens et al., 2017; Kawamata et al., 2018).

8.5 Size Definition

We define the galaxy size in the mock observations ($r_{\rm obs,mock}$) as the circularized half-light radius of the best-fit Sérsic profile. A Sérsic profile is defined as

$$I(r) = I_0 \exp\left[-\kappa\left(\frac{r}{r_{e,\rm major}}\right)^{1/n}\right], \tag{8.9}$$

where $I(r)$, I_0,κ, $r_{e,\rm major}$, and n are the surface brightness profile, the surface brightness at $r = 0$, the conversion factor from the scale radius to the half-light radius, the half-light radius along the semi-major axis, and the Sérsic index, respectively. The circularized radius ($r_{\rm obs,mock}$) is derived from the half-light radius along the semi-major axis ($r_{e,\rm major}$) through $r_{\rm obs,mock} \equiv r_{e,\rm major}\sqrt{b/a}$.

For the intrinsic sizes of the simulation galaxies, we use the radius ($r_{\rm sim}$) as the radius of a circle which is centered on the brightest pixel and encloses a half of the total flux. Before we measure intrinsic sizes, each SPH particle is smoothed over a 2D gaussian kernel with

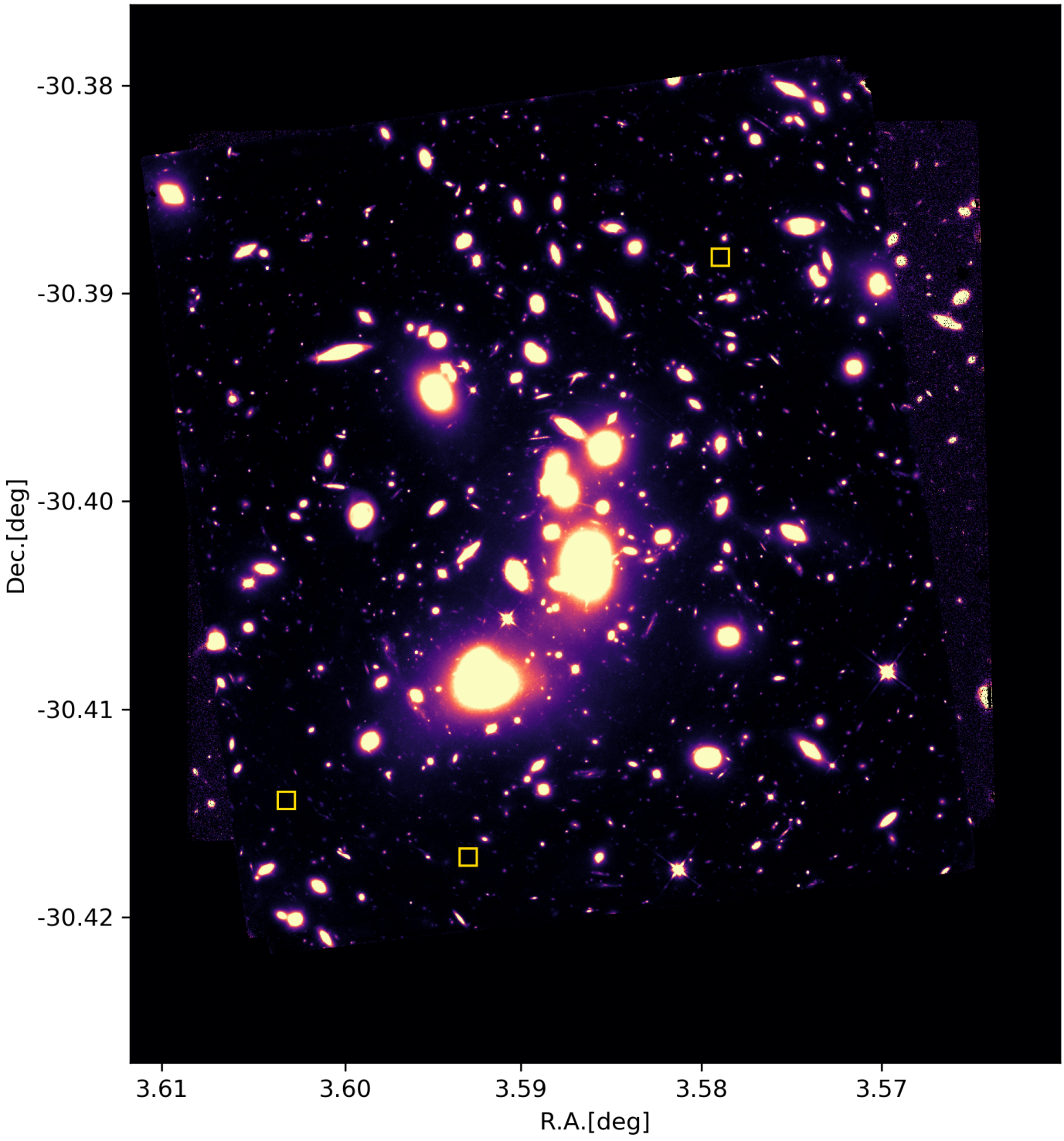

Figure 8.1: The image of the A2744 cluster field where three simulated galaxies (yellow open squares) have been added.

a dispersion equal to the softening length. Here, we adopt a straightforward definition of a half-light radius. We do not intend to determine the definition of a galaxy size universally applicable to clumpy or irregular galaxies. Our aim is to investigate whether a parametric fitting assuming a Sérsic profile reproduces an intrinsic size. For this purpose, this definition of $r_{\rm sim}$ makes sense.

Chapter 9

Mock Observed Size–luminosity Relation

9.1 Overview of the simulated galaxies

To give a visual inspection, we show the projected UV images of our simulated galaxies at three different viewing angles in Figure 9.1. The fourth column shows the same image as the first column at the resolution of the JJHH image (0".03 arcsec).

These galaxies have different morphologies from clumpy structures to a single smooth isophoto. Interestingly, clumpy structures are not resolved at the resolution of the JJHH image (the fourth column in Figure 9.1). The surface brightness profiles are blurred and look like smooth and extended profiles. In addition, our galaxies do not have a clear disk. Recent cosmological simulations also suggest that high-redshift galaxies tend to have giant clumps via violent disk instabilities and have a clumpy or irregular shape (e.g., Genel et al., 2012; Mandelker et al., 2017).

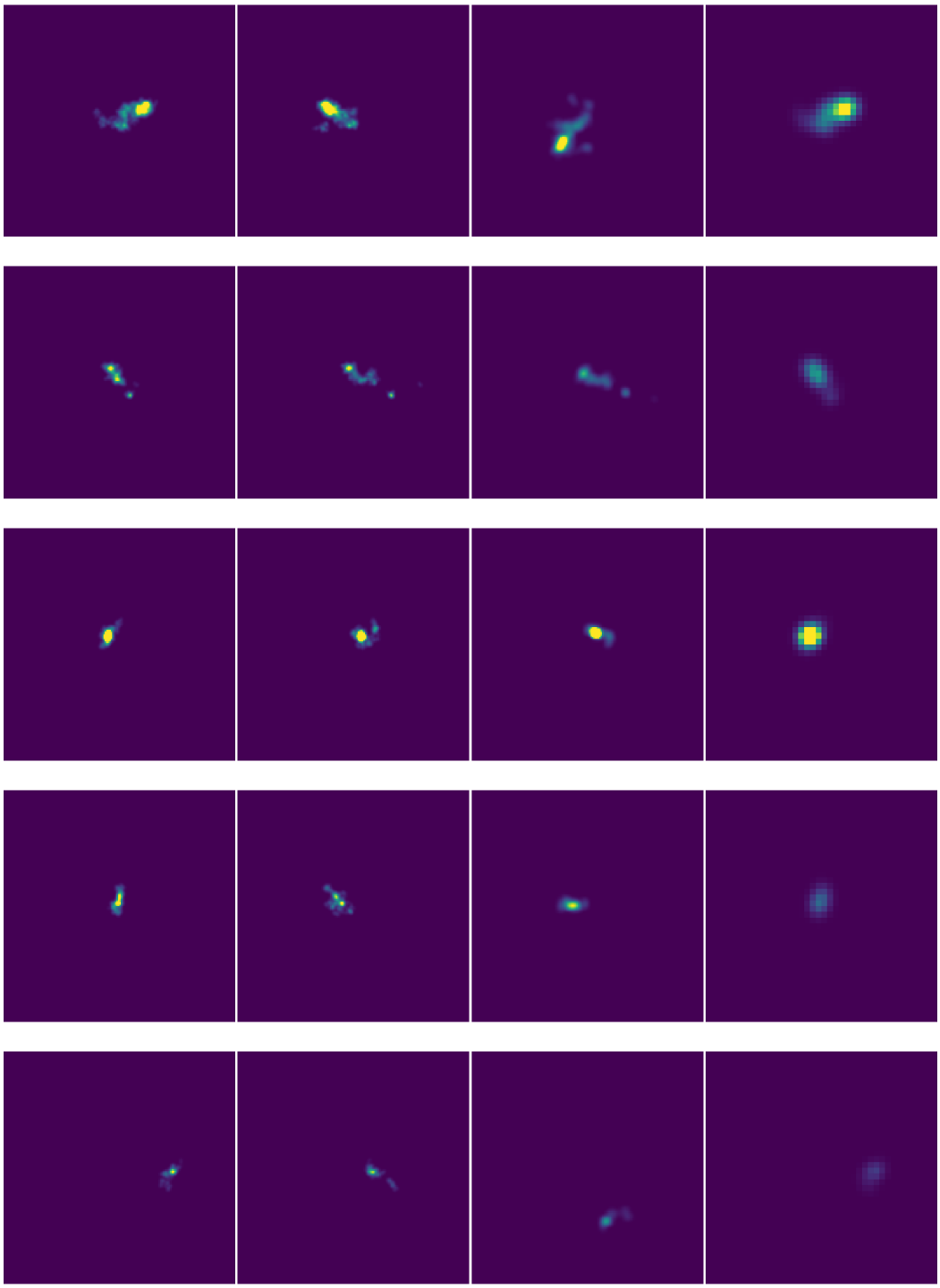

Figure 9.1: The projected UV images of our simulated galaxies on the source plane at three different viewing angles. The fourth column shows the same images as the first column at the resolution of the JJHH image.

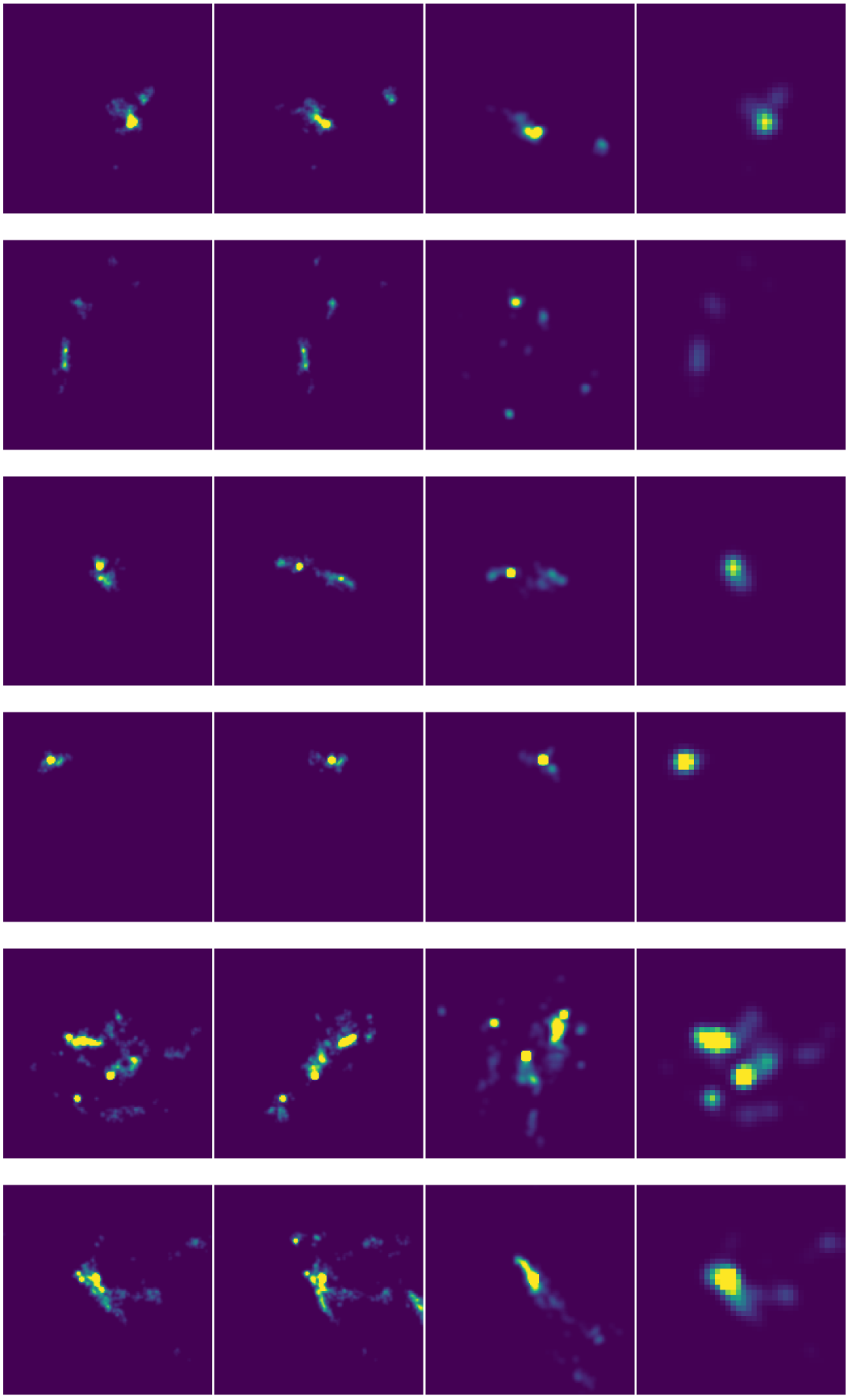

Figure 9.1: Continued.

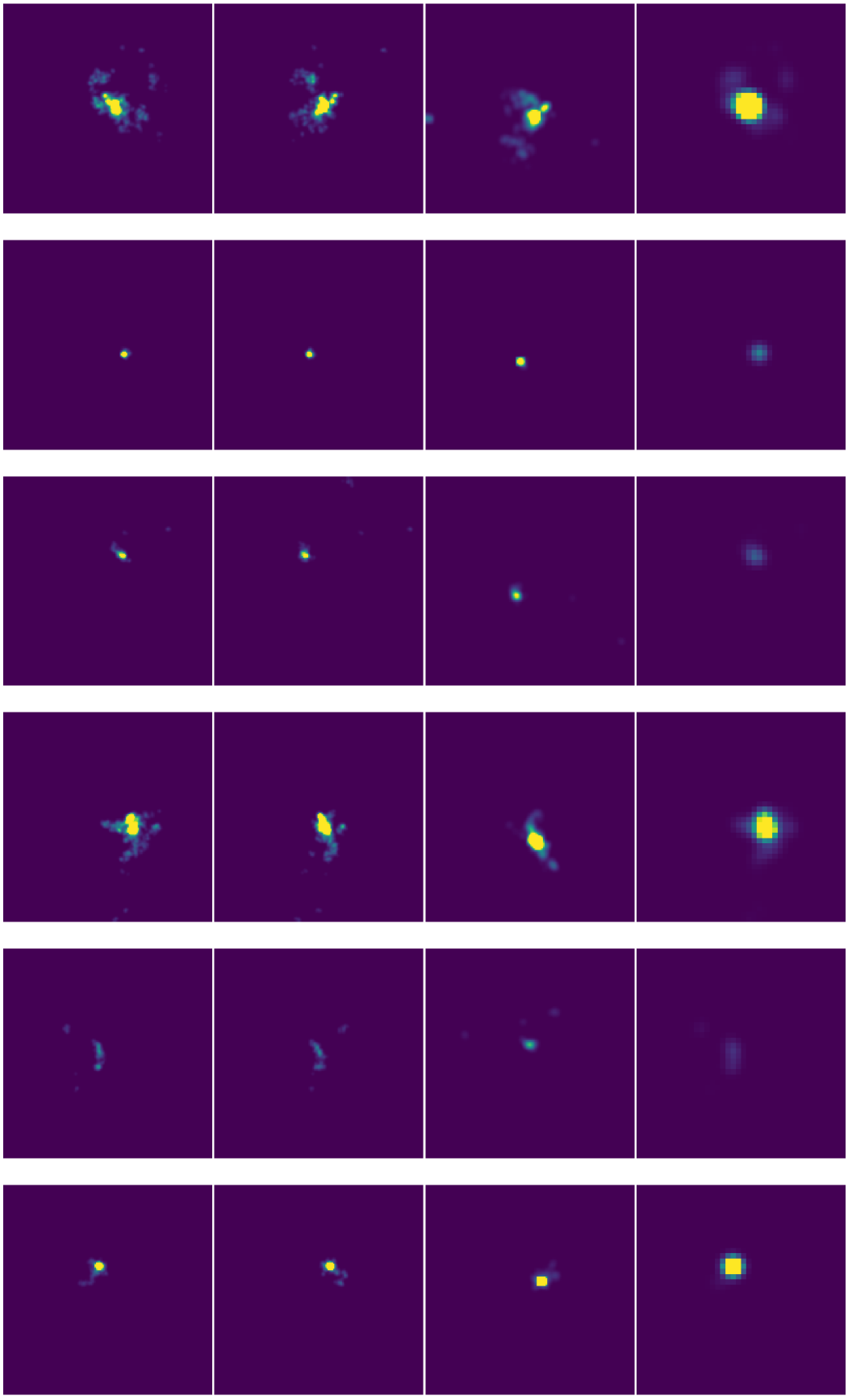

Figure 9.1: Continued.

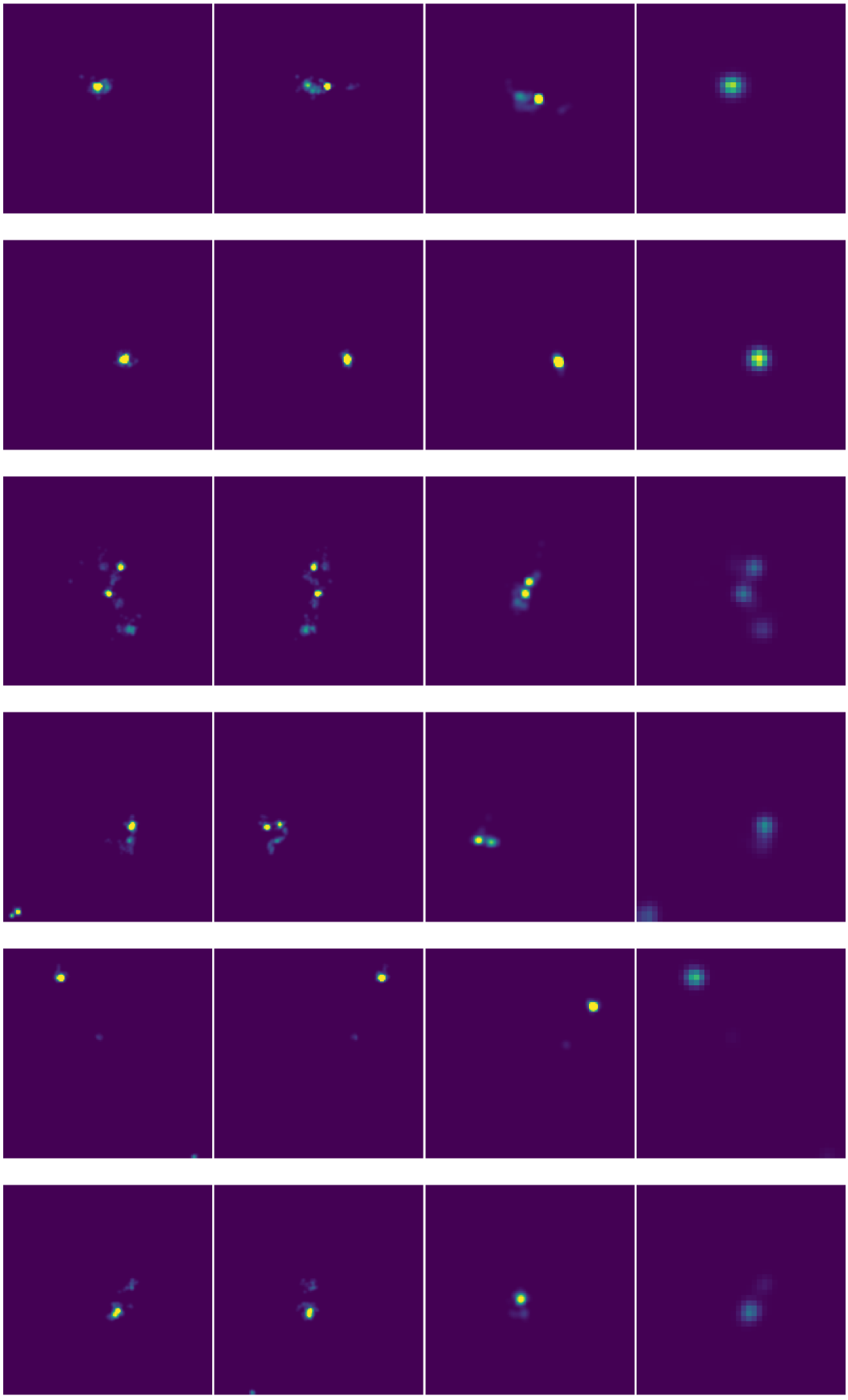

Figure 9.1: Continued.

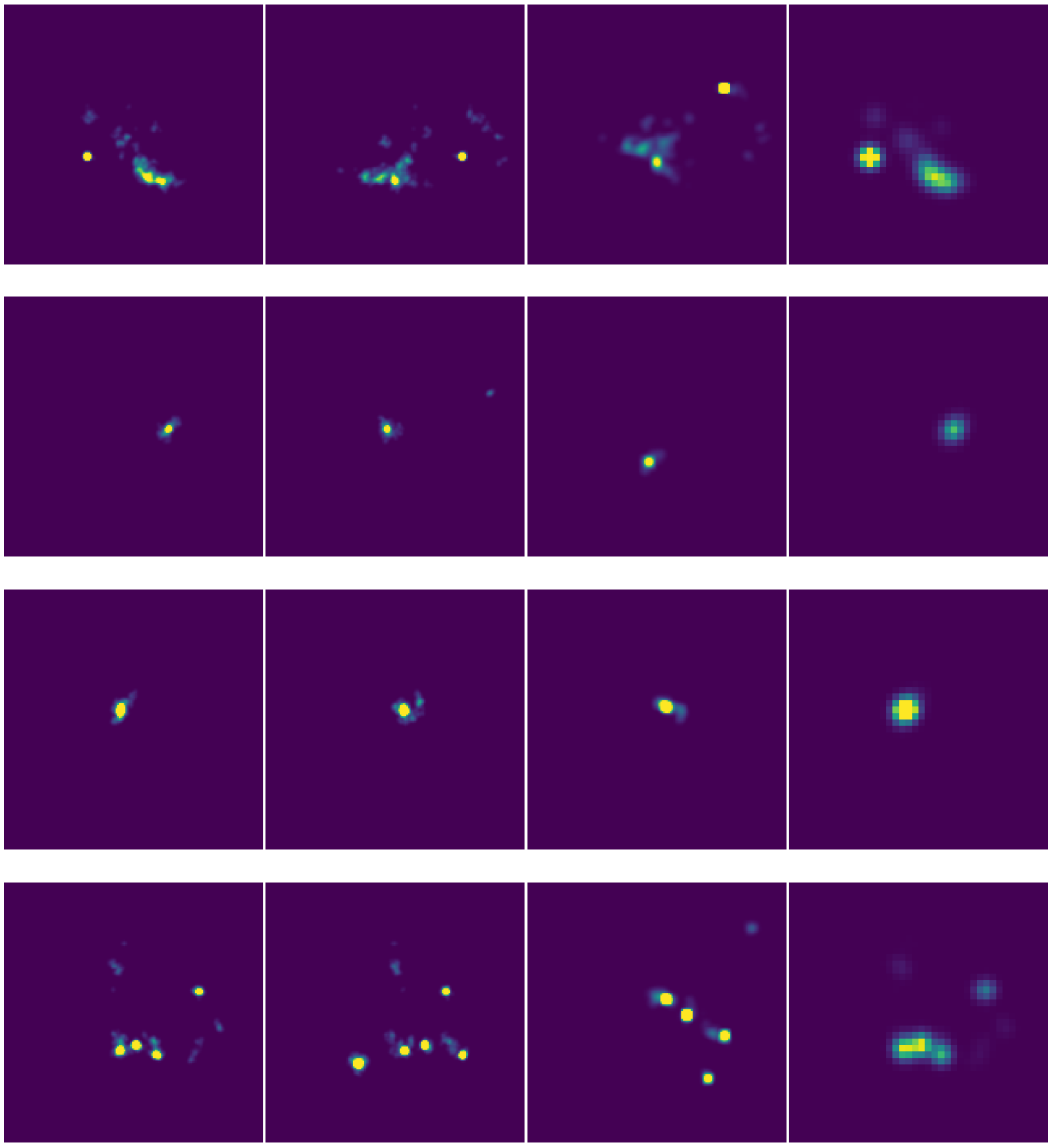

Figure 9.1: Continued.

9.2 Size–luminosity Relation

Figure 9.2 shows the size–luminosity relations of our simulated galaxies, together with the previous results. The intrinsic sizes ($r_{\rm sim}$) and magnitudes defined in the simulations are shown as filled cyan circles and the mock observed sizes ($r_{\rm obs,mock}$) and UV magnitudes are shown as filled orange circles. We perform the size measurements for all galaxies brighter than -17 mag, but we failed to converge the parameters for a fraction of them, which are shown as open cyan circles.

Kawamata et al. (2018) have performed the simultaneous maximum-likelihood estimation of the size–luminosity relation and the luminosity function assuming a log-normal size distribution at a given magnitude. They have found that the slope (β) of the observed size–luminosity relation is considerably steeper ($\beta \simeq 0.52$) (the black dashed line) than those ($\beta \sim 0.25$) at $z \sim 4-5$ (Huang et al., 2013) and the those with brighter UV magnitudes at $z \sim 6$ (Shibuya et al., 2015). This situation remains unchanged ($\beta \simeq 0.47$) even after incompleteness correction for large galaxies (the black solid line).

Our $r_{\rm sim}$–luminosity relation is slightly higher than the incompleteness-corrected size–luminosity relation by Kawamata et al. (2018), and is consistent with recent morphological studies using hydrodynamical simulations and SAMs (Ma et al., 2018b; Arata et al., 2019; Marshall et al., 2019). On the other hand, the $r_{\rm obs,mock}$–luminosity relation agrees with the uncorrected size–luminosity relation because sizes and magnitudes become smaller and fainter. This suggests that the underestimation of sizes and magnitudes is due to the size measurement procedure, and the incompleteness correction suggested by Kawamata et al. (2018) is not large enough to reproduce the intrinsic size–luminosity relation.

Before we discuss the cause of the underestimation of the sizes of the simulated galaxies in Section 9.3, we examine if the simulated galaxies also have a log-normal size distribution. According to the analytical disk model of Mo et al. (1998), the size of galaxies at a given magnitude is proportional to the dimensionless spin parameter (λ) of the hosting halos. As λ has a log-normal distribution with $\sigma_\lambda \simeq 0.5$ (Bullock et al., 2001), disk sizes also follow a log-normal distribution (Shen et al., 2003; Courteau et al., 2007; van der Wel et al., 2014). In Figure 9.3, we show the $r_{\rm sim}$ distribution with $-19 \leq M_{\rm UV} \leq -17$. In spite of a small sample size and the fact that our galaxies do not have a clear disk, the $r_{\rm sim}$ distribution follows a log-normal distribution with $\sigma_{\ln r_{\rm sim}} \simeq 0.7$. This is consistent with the previous works for high-redshift galaxies (Huang et al., 2013; Kawamata et al., 2018). Therefore, the assumption of a log-normal distribution can not be the cause of the difference between the $r_{\rm sim}$–luminosity relation and the incompleteness-corrected size–luminosity relation.

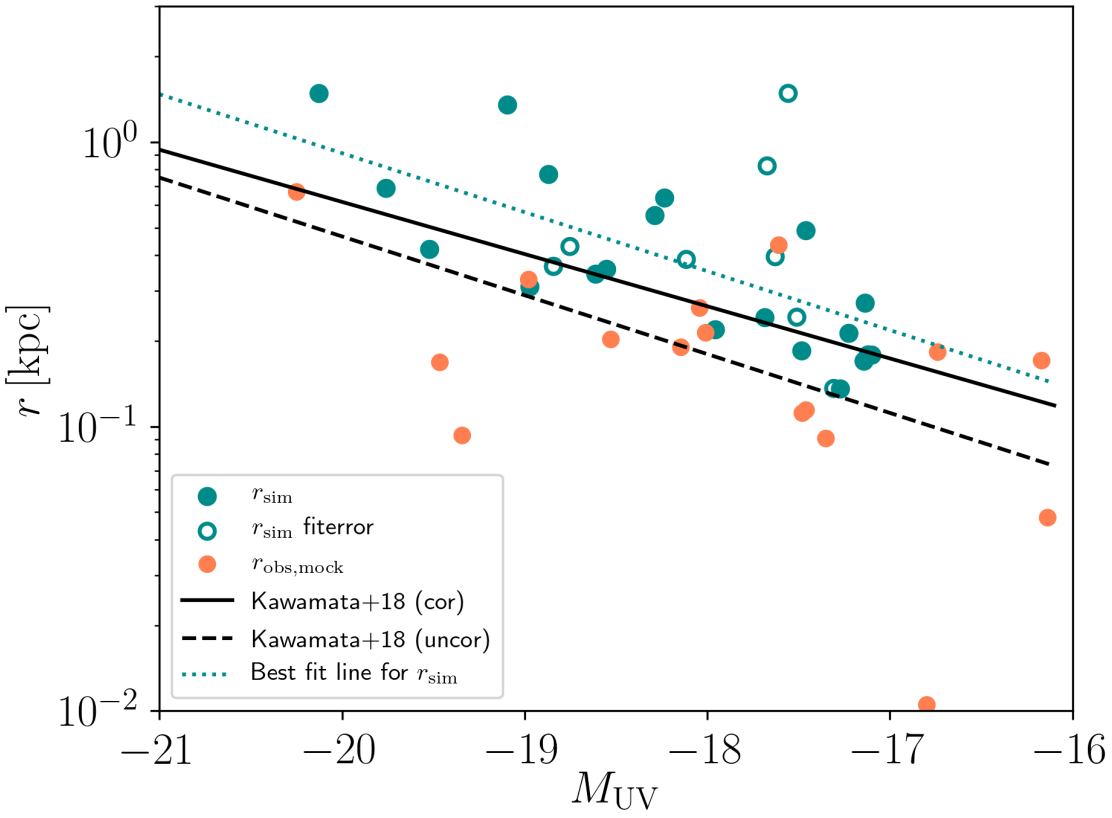

Figure 9.2: The distribution on the size–luminosity plane of the simulated galaxies. The intrinsic sizes ($r_{\rm sim}$) and UV magnitudes are shown as filled cyan circles and the mock observed sizes ($r_{\rm obs,mock}$) and UV magnitudes are shown as filled orange circles, respectively. The open cyan circles represent the $r_{\rm sim}$ and UV magnitudes of galaxies for which fitting fails. The black dashed line and black solid line show the incompleteness-corrected and uncorrected results at $z \sim 6-7$ by Kawamata et al. (2018), respectively. The cyan dotted line shows the best-fit line for $r_{\rm sim}$.

Our results also have an implication on the faint-end slope of the luminosity function. Bouwens et al. (2017) and Kawamata et al. (2018) have suggested that if the detection incompletness of faint but large galaxies is corrected, the faint-end slope of the luminosity function becomes steeper than previous estimates (Atek et al., 2014, 2015; Alavi et al., 2016; Castellano et al., 2016; Livermore et al., 2017). However, our results imply that the intrinsic sizes of faint sources are even larger than inferred by Bouwens et al. (2017) and Kawamata et al. (2018), which requires further incompleteness correction to the luminosity function.

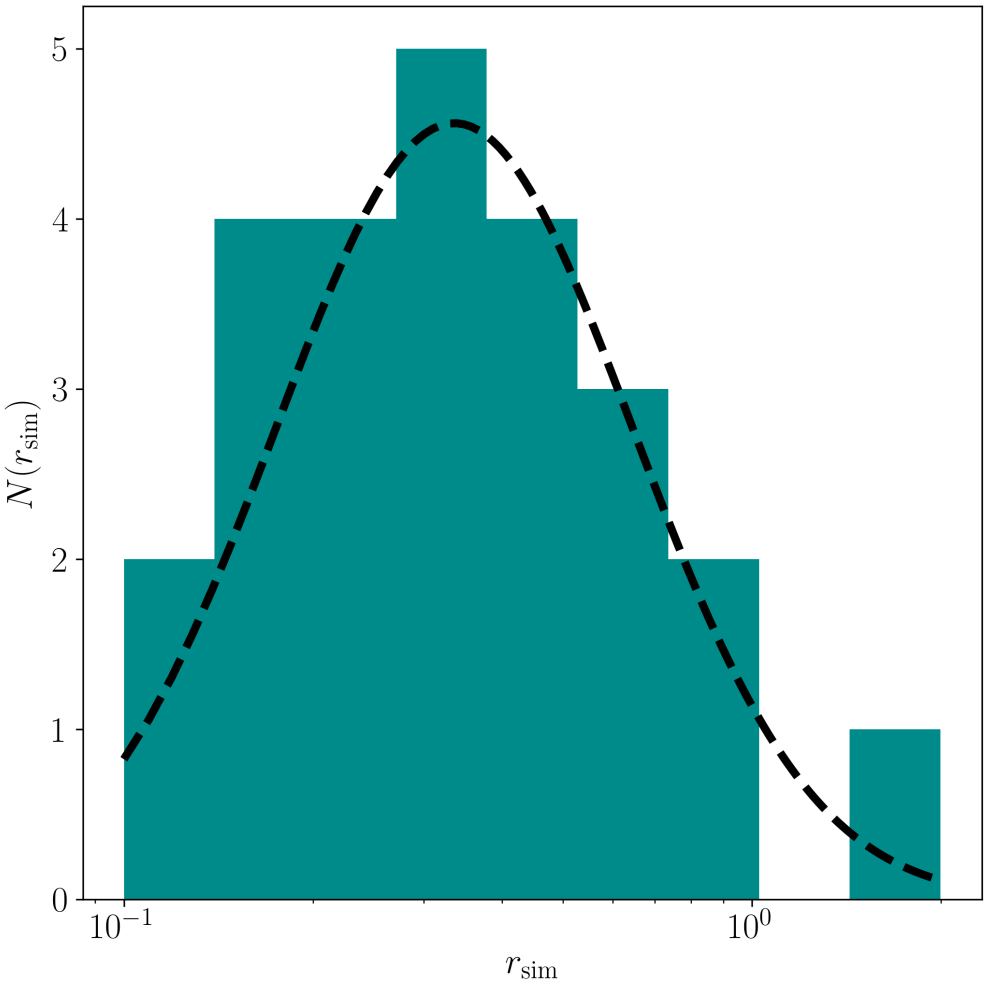

Figure 9.3: The $r_{\rm sim}$ distribution with $-19 \leq M_{\rm UV} \leq -17$. The black dashed line shows the best-fitting log-normal distribution.

9.3 Simulated sizes versus Observed sizes

Figure 9.2 has suggested that $r_{\rm obs,mock}$ is slightly smaller than $r_{\rm sim}$. It is helpful to compare $r_{\rm obs,mock}$ and $r_{\rm sim}$ in detail, which is shown in Figure 9.4. The black line denotes the $y = x$ line. This figure shows that $r_{\rm obs,mock}$ is systematically two or three times smaller than $r_{\rm sim}$. In this Section, we discuss possible causes of the underestimation.

One possible reason is that the surface brightness limit of the HFF data is too shallow, which is also suggested by Ma et al. (2018b). Ma et al. (2018b) have predicted the sizes

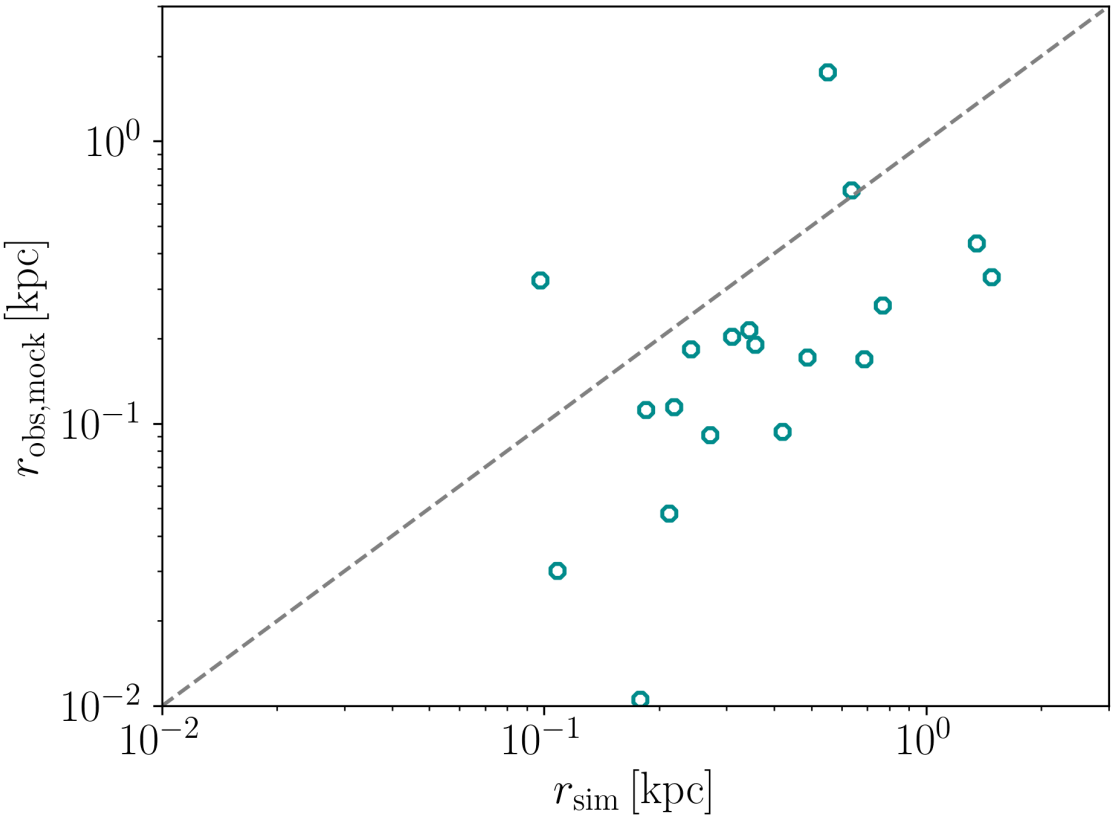

Figure 9.4: The comparison between $r_{\rm obs,mock}$ and $r_{\rm sim}$. The gray dashed line shows the $y = x$ line.

of faint ($-22 < M_{\rm UV} < -7$) galaxies at $z \geq 5$ by using the FIRE simulation. They have found that UV half-light radii, which is defined by a non-parametric method, are strongly affected by the surface brightness limit because a large fraction of UV fluxes is emitted from several bright stellar clumps. Although their galaxies have a larger intrinsic size than the extrapolation of the size–luminosity relations of Bouwens et al. (2017) and Kawamata et al. (2018), most of the clumpy structures of their galaxies become invisible and the half-light radii dramatically decrease if they assume the HFF surface brightness limit. Many of our simulated galaxies on the image plane also have faint extended structures originating from multiple clumps and the shear effect. A part of the structures are assimilated with the sky background and also becomes invisible on the JJHH image.

The second possible reason is that a single Sérsic profile with $n = 1$ can not trace the extended structures of a simulated galaxy. We show some examples of our simulated galaxies on the image plane and the fitting results in Figure 9.6. The lensed images are strongly magnified and elongated by the gravitational lensing effect. The galaxy on the

top row of Figure 9.6 has a faint extended structure at the right side. While our best-fit profile (third column from the left) successfully reproduces the surface brightness profile around the central region of the galaxy, the extended structure is not sufficiently traced. This may lead to the underestimation of the size and magnitude of the galaxy, even though we fit half-light radius and total magnitude simultaneously.

To examine these possibilities, we create a stacked image of our simulated galaxies on the source plane. The stacking is performed centered at the brightest pixel of each galaxy image. The surface brightness profile for the stacked image is shown in Figure 9.5. The gray horizontal line and the gray shaded region denote the average sky level of the JJHH image and 1-σ, respectively. This figure illustrates that a Sérsic index of the surface brightness profile changes at ~ 0.2 arcsec from the center. The surface brightness profile within ~ 0.2 arcsec is well fitted with a Sérsic profile with $n = 1$ (the black dotted line), whereas a deviation from it is seen beyond that point. This extended structure is traced with a Sérsic profile with $n \sim 0.36$ (the solid black line). A surface brightness profile that consists of two different Sérsic indices is never followed by using a single Sérsic profile. The same feature is also shown for the stacked image of lensed simulated galaxies on the image plane. Many of our galaxies are composed of several clumps, as indicated by the previous morphological studies in observations (Jiang et al., 2013; Bowler et al., 2017) and simulations (Ma et al., 2018a). On the JJHH image, these clumpy structures are not resolved and observed as extended structures.

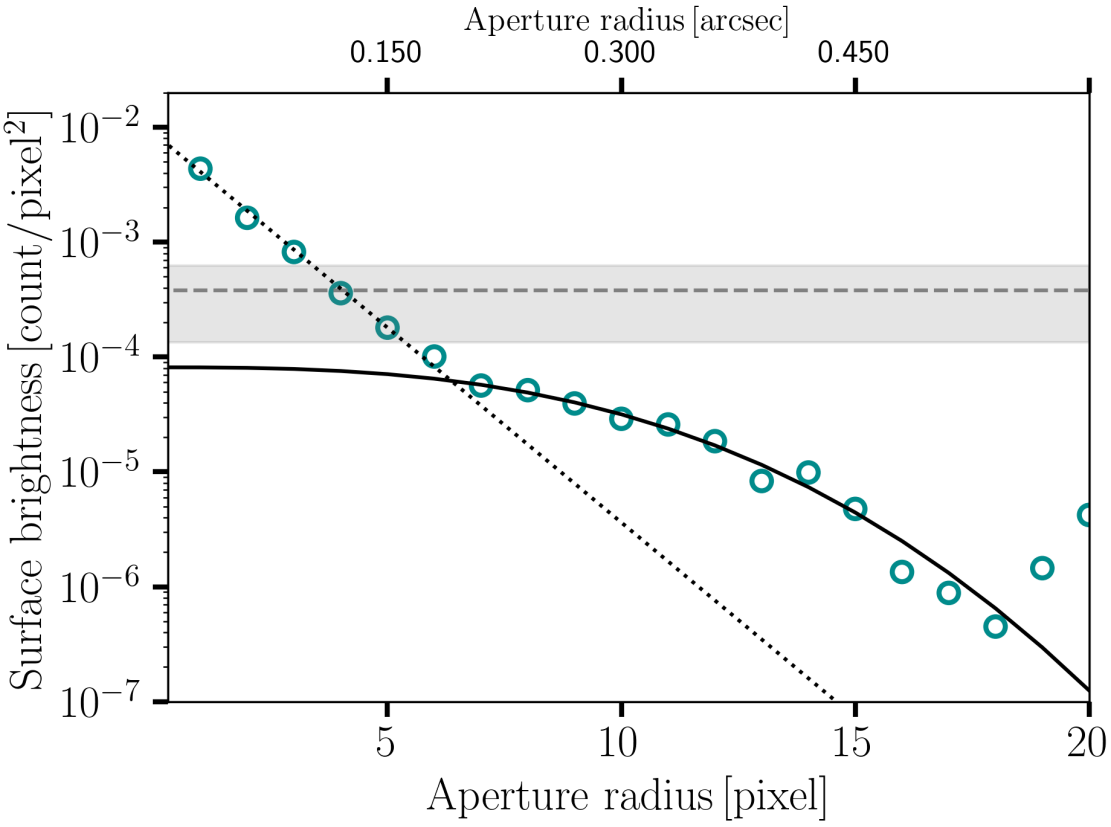

Figure 9.5: Surface brightness for the stacked image of the simulated galaxies on the source plane. The black dotted line shows the best-fitting Sérsic profile with $n = 1$ for data above the sky threshold, and the black solid line shows the best-fitting Sérsic profile at > 0.2 arcsec. The gray dashed line and the gray shaded region show the average sky level and the 1-σ error, respectively.

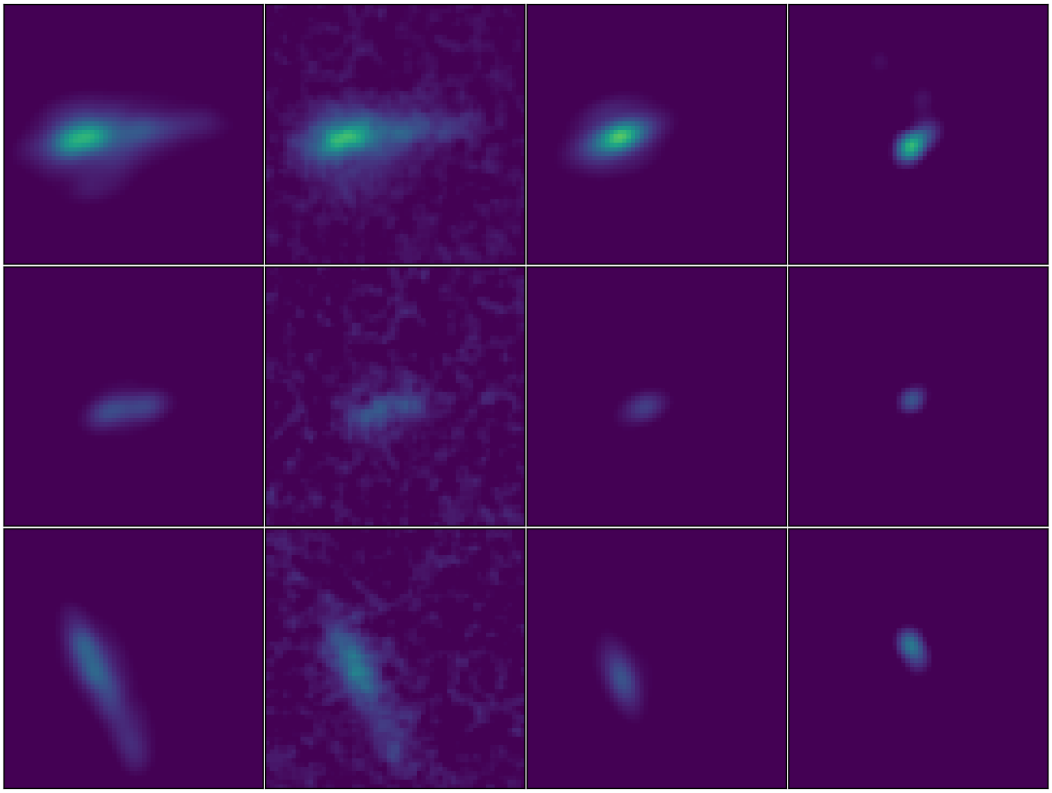

Figure 9.6: Example projected images of the simulated galaxies. From left to right columns are the lensed images on the image plane, those combined with the JJHH background images, the best-fitting Sérsic profile, the original images on the source plane.

9.4 Systematic Errors

In Section 9.3, we conclude that the shallow surface brightness limit and the assumption of a single Sérsic profile may be the cause of the underestimation of the sizes of the simulated galaxies. Besides them, there are many other possible causes of a systematic error in the procedure of the size measurements, by which $r_{\rm obs,mock}$ is underestimated or overestimated: the lensing effect, sky noise, and definition of a galaxy size. In this Section, we discuss systematic errors caused by them. In order to avoid a systematic error by sky noise, we bury our simulated galaxies in several places in Section 8.3.

The systematic errors by the lensing effect and the random error by sky noise are estimated by Kawamata et al. (2018) in the same field and mass map. The sky noise would also be the cause of a random error, which disperses the measured sizes randomly. They put a Sérsic profile with a random magnitude, size, ellipticity, and position angle, into a random position of the Abell2744 cluster field and perform the same fitting procedure as ours. They repeat this process until they obtain sufficient statistics. They find that the mock observed sizes are slightly larger ($< 10\%$) than the sizes of the original Sérsic profile. (see Figure 2 in Kawamata et al., 2018). This result is contrast to ours: the lensing effect systematically increases the observed sizes slightly. This is not the main cause of our underestimation.

A systematic error may also arise from the difference of the definition of a galaxy size. In the previous Section, we define $r_{\rm sim}$ as the radius which encloses the half light of a galaxy. On the other hand, the $r_{\rm obs,mock}$ is measured by a Sérsic profile. It is worth investigating whether the difference between the definition of $r_{\rm sim}$ and $r_{\rm obs,mock}$ affects our results. Here, we redefine $r_{\rm sim}$ as the circularized half-light radius of a Sérsic profile according to $r_{\rm obs,mock}$. We call this definition $r_{\rm sim,sersic}$. We preform a Sérsic profile fitting for the simulated UV surface density images with `GALFIT`. In the left panel of Figure 9.7, we show the same plot as Figure 9.4, but $r_{\rm sim}$ is changed to $r_{\rm sim,sersic}$. We also show the comparison between $r_{\rm sim}$ and $r_{\rm sim,sersic}$ in the right panel of Figure 9.7. Although $r_{\rm sim,sersic}$ is slightly smaller than $r_{\rm sim}$, the overall trend is not changed: the observed sizes ($r_{\rm obs,mock}$) are systematically smaller than the simulated sizes ($r_{\rm sim,sersic}$). Our main results are not affected by the difinition of $r_{\rm sim}$.

9.5 Caution for Size Measurements at very High Redshift

Here, we caution the traditional use of a Sérsic profile for $z \geq 6$ galaxies. Although a Sérsic profile approximated well the surface brightness profile of local ellipticals or disk

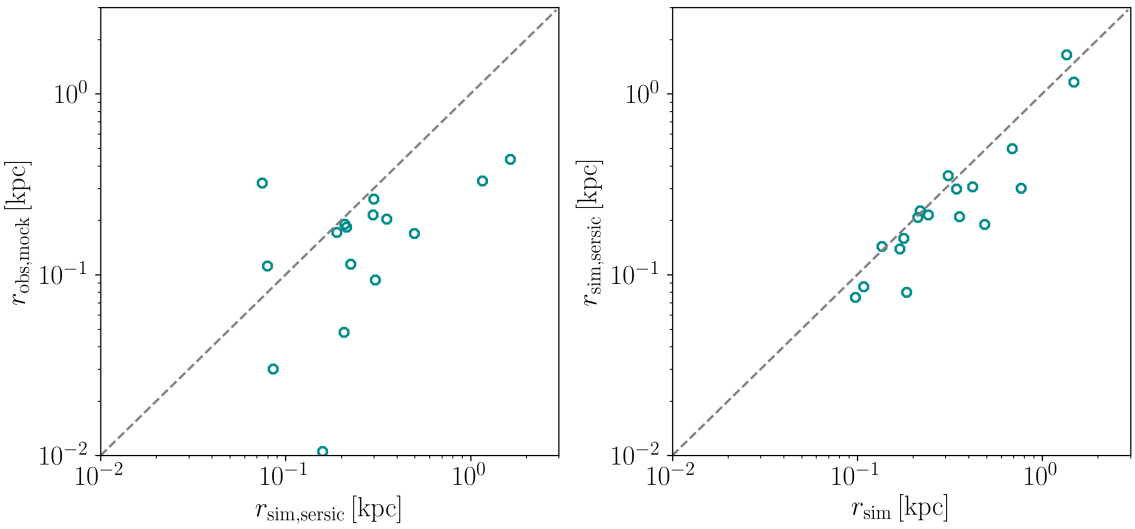

Figure 9.7: The comparison between $r_{\rm obs,mock}$ and $r_{\rm sim,sersic}$ (left) and $r_{\rm sim,sersic}$ and $r_{\rm sim}$ (right) . The gray dashed lines show the $y = x$ line.

galaxies, and probably of $z \leq 3$ galaxies, it still remains uncertain whether this profile is applicable to very high-redshift galaxies, which tend to have clumpy and extended structures. In Chapter 6, we estimate disk angular momentum from the observed sizes of galaxies at $z \sim 2-4$. This discussion is based on two assumptions that galaxies have an ordered disk with a parametric surface brightness profile and that the sizes are accurately measured with a parametric profile. These assumptions are almost valid at these redshifts. Compared with $z \sim 6$, the surface brightness dimming is ~ 30 times less severe at $z \sim 2$. This allows us to have deep images where we can measure accurate galaxy sizes. In reality, a Sérsic profile fitting for galaxies at $z \sim 2-4$ with `GALFIT` reproduces the galaxy surface brightness profile from the center to the outskirt.

However, sizes measured by assuming a Sérsic profile at $z \sim 6$ may be underestimated because it is biased toward the central region of the galaxies. Recently, a non-parametric approach, which defines the galaxy size by the number of pixels above a surface brightness threshold, has been introduced for size measurements, reflecting the clumpy and irregular morphologies of high-redshift galaxies. Figure 9.5 indicates, however, that we have a risk of underestimation even if we adopt a non-parametric size definition because most of the extended structures are under the average sky level without a magnification effect. Thus it is dangerous to use the same size measurement method as the local one. As high redshift galaxies ($z \geq 6$) tend to have clumpy or irregular shapes, the definition of a galaxy size is also crucial. We may need to change the definition according to the purposes.

Bouwens et al. (2017) have pointed out that in regions with a high shear in cluster lensing

fields, larger galaxies have been strongly stretched out along the shear axis, whereas small galaxies are not much affected. We note that our galaxies brighter than -17 mag tend to be affected by the shear, which means that the galaxies are elongated along the shear axis as shown in the bottom row in Figure 9.6. Galaxies like a point source are few. On the other hand, many of the observed galaxies fainter than -18 mag in Kawamata et al. (2018) show a round shape and look like they are not strongly affected by shear. The fact raises one possible concern that our hydrodynamic simulations make more extended sources than reality, though our result of $r_{\rm obs,mock}$–luminosity relation is consistent with observations. Future observations and simulations with next generation instruments will be necessary for further investigation. The *James Webb Space Telescope* (JWST), which is scheduled to be launched in 2020, will provide more samples of faint galaxies at $z > 6$ in and outside of the lensing fields, extending our understanding of the morphologies and sizes of galaxies.

Chapter 10

Conclusions

In this thesis, we have investigated the sizes, angular momenta, and morphologies of high-redshift galaxies. This thesis consists of two parts. In the first part, we have used the 3D-HST GOODS-South, COSMOS, and AEGIS imaging data and galaxy catalog to analyze the relation between the fraction of the dark halo mass settled as disk stars, $m_\star \equiv M_\star/M_{dh}$, and the fraction of the dark halo angular momentum transferred to the stellar disk, $j_\star \equiv J_\star/J_{dh}$ for 11738 star-forming galaxies over the stellar mass range $8.3 < \log(M_\star/M_\odot) < 11.1$ at $z \sim 2$, 3, and 4. For each redshift, we have divided the catalog into several $M_\star$ bins and infer M_{dh} by two independent methods, clustering analysis and abundance matching, to obtain an average $m_\star$ value for each bin. We have confirmed that the two mass estimators give consistent results. For our objects we have also measured effective radii r_d at rest 5000Å with `GALFIT`, and combined them with $m_\star$ and M_{dh} estimates to obtain $j_\star$ by applying Mo et al. (1998) analytic model of disk formation. The followings are the main results of the first part.

(i) We have found the median size evolution of disk star-forming galaxies $\overline{r}_d(M_{\star,10})/\mathrm{kpc} = 6.88(1+z)^{-0.91\pm0.01}$ at $M_\star = 1.0 \times 10^{10} M_\odot$. This redshift evolution is in agreement with the results by Allen et al. (2016) and Shibuya et al. (2015). We have also analyzed the slope of the disk size–stellar mass relation. While the slope is consistent with the results by van der Wel et al. (2014) at $z \sim 2$, we have found that the slope becomes shallower beyond $z \sim 2$. The scatter of r_d–$M_\star$ relation is $\sigma_{\ln r_d} \sim 0.4 - 0.6$ over the redshift range examined, which is comparable with the scatter of the log-normal distribution of λ.

(ii) We have obtained the angular momentum retention factor $j_\star/m_\star$ averaged over mass and redshift to be $\simeq 0.77\pm0.06$ from clustering analysis and $\simeq 0.83\pm0.13$ from abundance matching. These values are in rough agreement with those of local late-type galaxies by Romanowsky & Fall (2012) and those of star-forming galaxies at $z \sim 0.8 - 2.6$ by Burkert

et al. (2016).

(iii) Contrary to the star-forming galaxies at the present-day universe, $j_\star/m_\star$ appears to decrease with halo mass especially when abundance matching is used as the mass estimator. Combined with the slope of the $M_\star$–M_{dh} relation, this negative slope of the $j_\star/m_\star$–M_{dh} relation explain the shallow (< 0.2) slopes of the r_d–$M_\star$ relation obtained in this thesis. We have also found a possible decrease in the $j_\star/m_\star$–M_{dh} slope from $z \sim 2$ to $z \sim 4$, which may imply that feedback processes also change over this redshift range.

(iv) We have for the first time compared the observed mass–angular momentum relation with those of the recent galaxy formation simulations at $z \sim 2$ by Sales et al. (2012), Pedrosa & Tissera (2015), and Stevens et al. (2016). We have found that all of these simulations predict specific angular momenta systematically smaller than our values, which implies that these simulations produce too small disks at high redshifts while reproducing local measurements. We also find that a significant fraction of our galaxies appear to be unstable against bar formation.

In the second part, we use a cosmological hydrodynamical simulation framework, FiBY, which is an updated version of Gadget-3, in order to investigate what problem would happen if we adopt the same size measurement procedure as one used in the local universe for very high-redshift galaxies by providing simulated and mock observed size–luminosity relations. The simulated galaxies are lensed onto the JJHH image of the Abell2744 cluster field, and the sizes are measured with the almost same way as Kawamata et al. (2015, 2018). By comparing the intrinsic sizes in the simulations and the observed sizes in the mock observations, we have examined whether the surface brightness profile of the simulated galaxies is reproduced by a single Sérsic profile. The followings are the main results of the second part.

(v) Our simulated galaxies show a variety of shapes from clumpy structures to a single smooth isophote, and most of the galaxies do not have a disk. Our $r_{\rm sim}$–luminosity relation is slightly higher than the incompleteness corrected size–luminosity relation by Kawamata et al. (2018). However, the sizes and magnitudes are observed systematically smaller and fainter by the size measurement procedure. The $r_{\rm obs,mock}$–luminosity relation is comparable to the incompleteness uncorrected size–luminosity relation. Our results suggest that the intrinsic sizes of faint galaxies are larger than estimated by previous studies, and further incompleteness correction to the luminosity function are required.

(vi) Regarding the cause of the underestimation of the sizes of the simulated galaxies, two possible reasons are considered. One is that the surface brightness limit of the JJHH image is too shallow. The faint extended structures of our galaxies are assimilated with the background noise and become invisible. The other is that a single Sérsic profile can not trace the extended structures of the galaxies because a Sérsic profile may be biased toward the central region of the galaxies.

The results in the first part show that disk galaxies from local to intermediate redshifts retain relatively high specific angular momentum, which implies that these galaxies have well-ordered disks. For these galaxies, combined with the fact that the surface brightness dimming is not severe, we can measure the accurate galaxy sizes by using the size measurement method assuming a Sérsic profile. However, our results in the second part indicate that we need special care to apply a Sérsic profile to very high-redshift galaxies at $z > 6$, because the sizes of galaxies may be underestimated by the size measurement procedure. As very high redshift galaxies tend to have clumpy or irregular shapes, how to define a galaxy size is a complicated problem. For very high-redshift galaxies, we may need to determine an appropriate definition according to different purposes.

Appendix A

Clustering properties of GOODS-North and UDS fields

Before clustering analysis in Chapter 5, we calculate the angular correlation functions for all five fields. We separate each sample to luminosity bins, and compare with previous results (Ouchi et al., 2004; Lee et al., 2006; Barone-Nugent et al., 2014). Figure A.1 shows the angular correlation functions for the GOODS-North and UDS fields. The clustering properties for two fields are relatively smaller than the values by the previous results. The GOODS-North field has a negative correlation with luminosity. The UDS field has a smaller angular correlation function and there are no signals beyond 100 arcsec. Because of this strange behavior, we does not include these two fields for our analysis. The cause of this weak clustering properties is not clear. The small number of filters used for SED fitting may affect clustering properties.

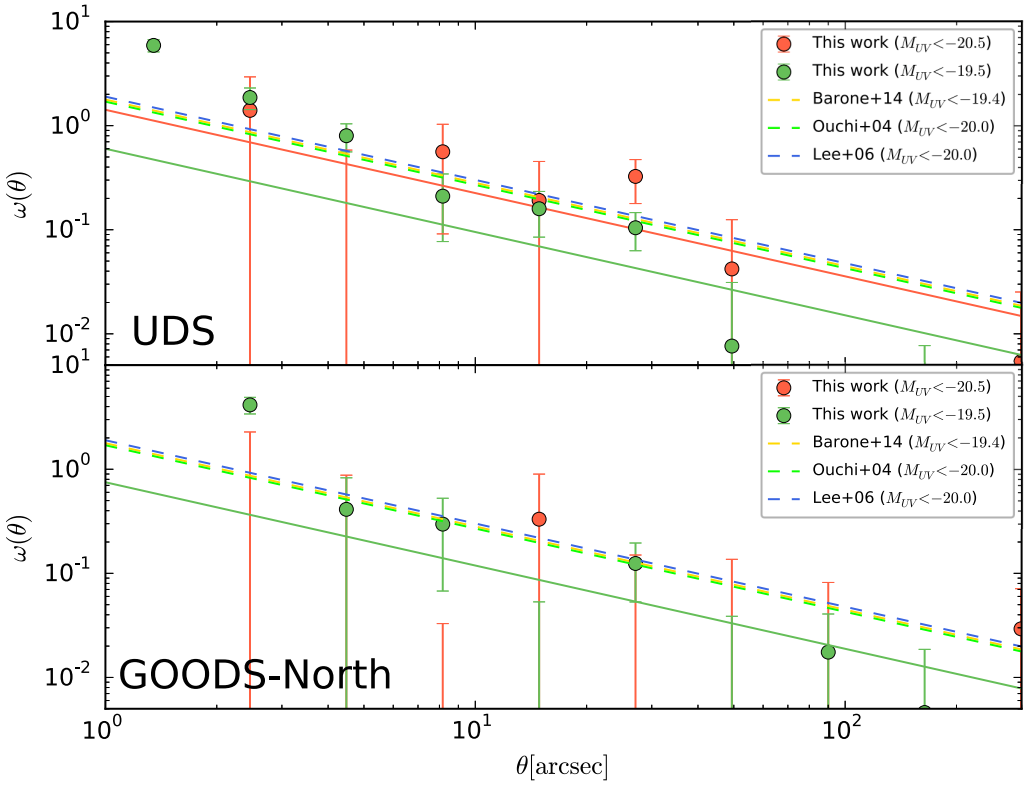

Figure A.1: Angular correlation functions compared with three previous results in UDS and GOODS-North fields at $z \sim 4$. The top and bottom panels show the results in UDS and GOODS-North fields, respectively. The solid red and green lines indicate the best-fit power laws for luminosity bins. The dashed yellow, green, and blue lines indicate the results by Barone-Nugent et al. (2014), Ouchi et al. (2004), and Lee et al. (2006), respectively.

Bibliography

Agarwal, B., & Khochfar, S. 2015, Monthly Notices of the Royal Astronomical Society, , 446, 160

Agertz, O., Teyssier, R., & Moore, B. 2011, Monthly Notices of the Royal Astronomical Society, , 410, 1391

Alavi, A., Siana, B., Richard, J., et al. 2016, The Astrophysical Journal, , 832, 56

Allen, R. J., Kacprzak, G. G., Glazebrook, K., et al. 2016, ArXiv e-prints, arXiv:1612.05262

Allende Prieto, C., Lambert, D. L., & Asplund, M. 2001, The Astrophysical Journal, Letters, , 556, L63

Andredakis, Y. C. 1998, Monthly Notices of the Royal Astronomical Society, , 295, 725

Angulo, R. E., & White, S. D. M. 2010, Monthly Notices of the Royal Astronomical Society, , 405, 143

Arata, S., Yajima, H., Nagamine, K., Li, Y., & Khochfar, S. 2019, Monthly Notices of the Royal Astronomical Society, , 488, 2629

Atek, H., Richard, J., Kneib, J.-P., et al. 2014, The Astrophysical Journal, , 786, 60

Atek, H., Richard, J., Jauzac, M., et al. 2015, The Astrophysical Journal, , 814, 69

Aumer, M., White, S. D. M., Naab, T., & Scannapieco, C. 2013, Monthly Notices of the Royal Astronomical Society, , 434, 3142

Bardeen, J. M., Bond, J. R., Kaiser, N., & Szalay, A. S. 1986, The Astrophysical Journal, , 304, 15

Barnes, J., & Efstathiou, G. 1987, The Astrophysical Journal, , 319, 575

Barone-Nugent, R. L., Trenti, M., Wyithe, J. S. B., et al. 2014, The Astrophysical Journal, , 793, 17

Behroozi, P. S., Wechsler, R. H., & Conroy, C. 2013, The Astrophysical Journal, , 770, 57

Bertin, E., & Arnouts, S. 1996, Astronomy & Astrophysics Supplement, , 117, 393

Bond, J. R., Cole, S., Efstathiou, G., & Kaiser, N. 1991, The Astrophysical Journal, , 379, 440

Bouwens, R. J., Illingworth, G. D., Oesch, P. A., et al. 2017, The Astrophysical Journal, , 843, 41

Bower, R. G. 1991, Monthly Notices of the Royal Astronomical Society, , 248, 332

Bowler, R. A. A., Dunlop, J. S., McLure, R. J., & McLeod, D. J. 2017, Monthly Notices of the Royal Astronomical Society, , 466, 3612

Bowler, R. A. A., Dunlop, J. S., McLure, R. J., et al. 2014, Monthly Notices of the Royal Astronomical Society, , 440, 2810

Brammer, G. B., van Dokkum, P. G., & Coppi, P. 2008, The Astrophysical Journal, , 686, 1503

Brammer, G. B., van Dokkum, P. G., Franx, M., et al. 2012, The Astrophysical Journal, Supplement, , 200, 13

Brennan, R., Pandya, V., Somerville, R. S., et al. 2017, Monthly Notices of the Royal Astronomical Society, , 465, 619

Brook, C. B., Stinson, G., Gibson, B. K., et al. 2012, Monthly Notices of the Royal Astronomical Society, , 419, 771

Brook, C. B., Governato, F., Roškar, R., et al. 2011, Monthly Notices of the Royal Astronomical Society, , 415, 1051

Bullock, J. S., Dekel, A., Kolatt, T. S., et al. 2001, The Astrophysical Journal, , 555, 240

Burkert, A., Förster Schreiber, N. M., Genzel, R., et al. 2016, The Astrophysical Journal, , 826, 214

Calzetti, D., Kinney, A. L., & Storchi-Bergmann, T. 1994, The Astrophysical Journal, , 429, 582

Carroll, S. M., Press, W. H., & Turner, E. L. 1992, Annual Review of Astronomy & Astrophysics, , 30, 499

Castellano, M., Yue, B., Ferrara, A., et al. 2016, The Astrophysical Journal, Letters, , 823, L40

Chabrier, G. 2003, Publications of the Astronomical Society of Pacific, , 115, 763

Ciotti, L., & Bertin, G. 1999, Astronomy & Astrophysics, , 352, 447

Coe, D., Bradley, L., & Zitrin, A. 2015, The Astrophysical Journal, , 800, 84

Colín, P., Avila-Reese, V., Roca-Fàbrega, S., & Valenzuela, O. 2016, The Astrophysical Journal, , 829, 98

Contini, T., Epinat, B., Bouché, N., et al. 2016, Astronomy & Astrophysics, , 591, A49

Courteau, S., de Jong, R. S., & Broeils, A. H. 1996, The Astrophysical Journal, Letters, , 457, L73

Courteau, S., Dutton, A. A., van den Bosch, F. C., et al. 2007, The Astrophysical Journal, , 671, 203

Crain, R. A., Schaye, J., Bower, R. G., et al. 2015, Monthly Notices of the Royal Astronomical Society, , 450, 1937

Croton, D. J., Stevens, A. R. H., Tonini, C., et al. 2016, The Astrophysical Journal, Supplement, , 222, 22

Cullen, F., McLure, R. J., Khochfar, S., Dunlop, J. S., & Dalla Vecchia, C. 2017, Monthly Notices of the Royal Astronomical Society, , 470, 3006

Curtis-Lake, E., McLure, R. J., Dunlop, J. S., et al. 2016, Monthly Notices of the Royal Astronomical Society, , 457, 440

Daddi, E., Bournaud, F., Walter, F., et al. 2010, The Astrophysical Journal, , 713, 686

Davies, J. I., Phillipps, S., Cawson, M. G. M., Disney, M. J., & Kibblewhite, E. J. 1988, Monthly Notices of the Royal Astronomical Society, , 232, 239

Davis, A. J., & Natarajan, P. 2009, Monthly Notices of the Royal Astronomical Society, , 393, 1498

DeFelippis, D., Genel, S., Bryan, G. L., & Fall, S. M. 2017, The Astrophysical Journal, , 841, 16

Draine, B. T., & Li, A. 2007, The Astrophysical Journal, , 657, 810

Draine, B. T., Dale, D. A., Bendo, G., et al. 2007, The Astrophysical Journal, , 663, 866

Draine, B. T., Aniano, G., Krause, O., et al. 2014, The Astrophysical Journal, , 780, 172

Dutton, A. A., Conroy, C., van den Bosch, F. C., Prada, F., & More, S. 2010, Monthly Notices of the Royal Astronomical Society, , 407, 2

Dutton, A. A., & van den Bosch, F. C. 2012, Monthly Notices of the Royal Astronomical Society, , 421, 608

Dutton, A. A., Conroy, C., van den Bosch, F. C., et al. 2011, Monthly Notices of the Royal Astronomical Society, , 416, 322

Efstathiou, G., Bernstein, G., Tyson, J. A., Katz, N., & Guhathakurta, P. 1991, The Astrophysical Journal, Letters, , 380, L47

Efstathiou, G., Lake, G., & Negroponte, J. 1982, Monthly Notices of the Royal Astronomical Society, , 199, 1069

Fall, S. M. 1983, in IAU Symposium, Vol. 100, Internal Kinematics and Dynamics of Galaxies, ed. E. Athanassoula, 391–398

Fall, S. M., & Efstathiou, G. 1980, Monthly Notices of the Royal Astronomical Society, , 193, 189

Fall, S. M., & Romanowsky, A. J. 2013, The Astrophysical Journal, Letters, , 769, L26

Ferguson, H. C., Dickinson, M., Giavalisco, M., et al. 2004, The Astrophysical Journal, Letters, , 600, L107

Ferland, G. J., Korista, K. T., Verner, D. A., et al. 1998, Publications of the Astronomical Society of Pacific, , 110, 761

Finkelstein, S. L., Ryan, Russell E., J., Papovich, C., et al. 2015, The Astrophysical

Journal, , 810, 71

Foreman-Mackey, D. 2016, The Journal of Open Source Software, 24, doi:10.21105/joss.00024

Foreman-Mackey, D., Hogg, D. W., Lang, D., & Goodman, J. 2013, Publications of the Astronomical Society of Pacific, , 125, 306

Foucaud, S., Conselice, C. J., Hartley, W. G., et al. 2010, Monthly Notices of the Royal Astronomical Society, , 406, 147

Foucaud, S., McCracken, H. J., Le Fèvre, O., et al. 2003, Astronomy & Astrophysics, , 409, 835

Genel, S., Fall, S. M., Hernquist, L., et al. 2015, The Astrophysical Journal, Letters, , 804, L40

Genel, S., Naab, T., Genzel, R., et al. 2012, The Astrophysical Journal, , 745, 11

Genel, S., Vogelsberger, M., Springel, V., et al. 2014, Monthly Notices of the Royal Astronomical Society, , 445, 175

Gillman, S., Swinbank, A. M., Tiley, A. L., et al. 2019, Monthly Notices of the Royal Astronomical Society, , 486, 175

Governato, F., Willman, B., Mayer, L., et al. 2007, Monthly Notices of the Royal Astronomical Society, , 374, 1479

Governato, F., Zolotov, A., Pontzen, A., et al. 2012, Monthly Notices of the Royal Astronomical Society, , 422, 1231

Grogin, N. A., Kocevski, D. D., Faber, S. M., et al. 2011, The Astrophysical Journal, Supplement, , 197, 35

Groth, E. J., & Peebles, P. J. E. 1977, The Astrophysical Journal, , 217, 385

Guo, Q., White, S., Boylan-Kolchin, M., et al. 2011, Monthly Notices of the Royal Astronomical Society, , 413, 101

Hahn, O., & Abel, T. 2011, Monthly Notices of the Royal Astronomical Society, , 415, 2101

Harikane, Y., Ouchi, M., Ono, Y., et al. 2016, The Astrophysical Journal, , 821, 123

Hatton, S., Devriendt, J. E. G., Ninin, S., et al. 2003, Monthly Notices of the Royal Astronomical Society, , 343, 75

Häussler, B., McIntosh, D. H., Barden, M., et al. 2007, The Astrophysical Journal, Supplement, , 172, 615

Henriques, B. M. B., White, S. D. M., Thomas, P. A., et al. 2015, Monthly Notices of the Royal Astronomical Society, , 451, 2663

Hopkins, P. F., Kereš, D., Oñorbe, J., et al. 2014, Monthly Notices of the Royal Astronomical Society, , 445, 581

Hopkins, P. F., Quataert, E., & Murray, N. 2011, Monthly Notices of the Royal Astronomical Society, , 417, 950

Huang, K.-H., Ferguson, H. C., Ravindranath, S., & Su, J. 2013, The Astrophysical Journal, , 765, 68

Huang, K.-H., Fall, S. M., Ferguson, H. C., et al. 2017, The Astrophysical Journal, , 838, 6

Hubble, E. P. 1936, Realm of the Nebulae

Ishigaki, M., Kawamata, R., Ouchi, M., et al. 2015, The Astrophysical Journal, , 799, 12

Jauzac, M., Richard, J., Jullo, E., et al. 2015, Monthly Notices of the Royal Astronomical Society, , 452, 1437

Jiang, L., Egami, E., Fan, X., et al. 2013, The Astrophysical Journal, , 773, 153

Johnson, J. L., Dalla Vecchia, C., & Khochfar, S. 2013, Monthly Notices of the Royal Astronomical Society, , 428, 1857

Kaufmann, T., Mayer, L., Wadsley, J., Stadel, J., & Moore, B. 2007, Monthly Notices of the Royal Astronomical Society, , 375, 53

Kawamata, R., Ishigaki, M., Shimasaku, K., Oguri, M., & Ouchi, M. 2015, The Astrophysical Journal, , 804, 103

Kawamata, R., Ishigaki, M., Shimasaku, K., et al. 2018, The Astrophysical Journal, , 855, 4

Kawamata, R., Oguri, M., Ishigaki, M., Shimasaku, K., & Ouchi, M. 2016, The Astrophysical Journal, , 819, 114

Keeton, C. R. 2001, arXiv e-prints, astro

Kennicutt, Robert C., J. 1998, The Astrophysical Journal, , 498, 541

Kochanek, C. S. 1991, The Astrophysical Journal, , 373, 354

Koekemoer, A. M., Faber, S. M., Ferguson, H. C., et al. 2011, The Astrophysical Journal, Supplement, , 197, 36

Köhlinger, F., & Schmidt, R. W. 2014, Monthly Notices of the Royal Astronomical Society, , 437, 1858

Kravtsov, A. V. 2013, The Astrophysical Journal, Letters, , 764, L31

Kriek, M., van Dokkum, P. G., Labbé, I., et al. 2009, The Astrophysical Journal, , 700, 221

Lacey, C., & Cole, S. 1993, Monthly Notices of the Royal Astronomical Society, , 262, 627

Lagos, C. d. P., Theuns, T., Stevens, A. R. H., et al. 2017, Monthly Notices of the Royal Astronomical Society, , 464, 3850

Lam, D., Broadhurst, T., Diego, J. M., et al. 2014, The Astrophysical Journal, , 797, 98

Landy, S. D., & Szalay, A. S. 1993, The Astrophysical Journal, , 412, 64

Laporte, N., Infante, L., Troncoso Iribarren, P., et al. 2016, The Astrophysical Journal, , 820, 98

Law, D. R., Steidel, C. C., Erb, D. K., et al. 2007, The Astrophysical Journal, , 656, 1

Lee, K.-S., Giavalisco, M., Gnedin, O. Y., et al. 2006, The Astrophysical Journal, , 642, 63

Lewis, G. F., Babul, A., Katz, N., et al. 2000, The Astrophysical Journal, , 536, 623

Livermore, R. C., Finkelstein, S. L., & Lotz, J. M. 2017, The Astrophysical Journal, , 835, 113

Lotz, J. M., Koekemoer, A., Coe, D., et al. 2017, The Astrophysical Journal, , 837, 97

Ma, X., Hopkins, P. F., Garrison-Kimmel, S., et al. 2018a, Monthly Notices of the Royal Astronomical Society, , 478, 1694

Ma, X., Hopkins, P. F., Boylan-Kolchin, M., et al. 2018b, Monthly Notices of the Royal Astronomical Society, , 477, 219

MacArthur, L. A., Courteau, S., & Holtzman, J. A. 2003, The Astrophysical Journal, , 582, 689

Mahler, G., Richard, J., Clément, B., et al. 2018, Monthly Notices of the Royal Astronomical Society, , 473, 663

Mandelker, N., Dekel, A., Ceverino, D., et al. 2017, Monthly Notices of the Royal Astronomical Society, , 464, 635

Marshall, M. A., Mutch, S. J., Qin, Y., Poole, G. B., & Wyithe, J. S. B. 2019, Monthly Notices of the Royal Astronomical Society, , 488, 1941

McLure, R. J., Dunlop, J. S., Bowler, R. A. A., et al. 2013, Monthly Notices of the Royal Astronomical Society, , 432, 2696

Merten, J., Coe, D., Dupke, R., et al. 2011, Monthly Notices of the Royal Astronomical Society, , 417, 333

Mo, H., van den Bosch, F. C., & White, S. 2010, Galaxy Formation and Evolution

Mo, H. J., Mao, S., & White, S. D. M. 1998, Monthly Notices of the Royal Astronomical Society, , 295, 319

Murante, G., Monaco, P., Giovalli, M., Borgani, S., & Diaferio, A. 2010, Monthly Notices of the Royal Astronomical Society, , 405, 1491

Navarro, J. F., & Benz, W. 1991, The Astrophysical Journal, , 380, 320

Navarro, J. F., Frenk, C. S., & White, S. D. M. 1997, The Astrophysical Journal, , 490, 493

Navarro, J. F., & Steinmetz, M. 2000, The Astrophysical Journal, , 538, 477

Navarro, J. F., & White, S. D. M. 1994, Monthly Notices of the Royal Astronomical Society, , 267, 401

Noguchi, M. 1987, Monthly Notices of the Royal Astronomical Society, , 228, 635

Obreschkow, D., Glazebrook, K., Bassett, R., et al. 2015, The Astrophysical Journal, , 815, 97

Oesch, P. A., Bouwens, R. J., Carollo, C. M., et al. 2010, The Astrophysical Journal, Letters, , 709, L21

Oguri, M. 2010, Publications of the Astronomical Society of Japan, , 62, 1017

Oguri, M., Bayliss, M. B., Dahle, H., et al. 2012, Monthly Notices of the Royal Astronomical Society, , 420, 3213

Oguri, M., Schrabback, T., Jullo, E., et al. 2013, Monthly Notices of the Royal Astronomical Society, , 429, 482

Oke, J. B., & Gunn, J. E. 1983, The Astrophysical Journal, , 266, 713

Ono, Y., Ouchi, M., Curtis-Lake, E., et al. 2013, The Astrophysical Journal, , 777, 155

Ouchi, M., Shimasaku, K., Okamura, S., et al. 2001, The Astrophysical Journal, Letters, , 558, L83

—. 2004, The Astrophysical Journal, , 611, 685

Ouchi, M., Shimasaku, K., Furusawa, H., et al. 2010, The Astrophysical Journal, , 723, 869

Paardekooper, J. P., Khochfar, S., & Dalla, C. V. 2013, Monthly Notices of the Royal Astronomical Society, , 429, L94

Paulino-Afonso, A., Sobral, D., Buitrago, F., & Afonso, J. 2017, Monthly Notices of the Royal Astronomical Society, , 465, 2717

Pedrosa, S. E., & Tissera, P. B. 2015, Astronomy & Astrophysics, , 584, A43

Peebles, P. J. E. 1969, The Astrophysical Journal, , 155, 393

—. 1975, The Astrophysical Journal, , 196, 647

—. 1980, The large-scale structure of the universe

Peng, C. Y., Ho, L. C., Impey, C. D., & Rix, H.-W. 2002, The Astronomical Journal, , 124, 266

—. 2010, The Astronomical Journal, , 139, 2097

Petrushevska, T., Okamura, T., Kawamata, R., et al. 2018, Astronomy Reports, 62, 917

Pillepich, A., Nelson, D., Hernquist, L., et al. 2018, Monthly Notices of the Royal Astronomical Society, , 475, 648

Pillepich, A., Nelson, D., Springel, V., et al. 2019, Monthly Notices of the Royal Astronomical Society, , 490, 3196

Planck Collaboration, Ade, P. A. R., Aghanim, N., et al. 2016, Astronomy & Astrophysics, , 594, A13

Porter, L. A., Somerville, R. S., Primack, J. R., & Johansson, P. H. 2014, Monthly Notices

of the Royal Astronomical Society, , 444, 942

Prada, F., Klypin, A. A., Cuesta, A. J., Betancort-Rijo, J. E., & Primack, J. 2012, Monthly Notices of the Royal Astronomical Society, , 423, 3018

Press, W. H., & Schechter, P. 1974, The Astrophysical Journal, , 187, 425

Puech, M., Hammer, F., Flores, H., et al. 2010, Astronomy & Astrophysics, , 510, A68

Ribeiro, B., Le Fèvre, O., Tasca, L. A. M., et al. 2016, Astronomy & Astrophysics, , 593, A22

Richard, J., Jauzac, M., Limousin, M., et al. 2014, Monthly Notices of the Royal Astronomical Society, , 444, 268

Robertson, B., Bullock, J. S., Cox, T. J., et al. 2006, The Astrophysical Journal, , 645, 986

Roche, N., & Eales, S. A. 1999, Monthly Notices of the Royal Astronomical Society, , 307, 111

Rodríguez-Puebla, A., Behroozi, P., Primack, J., et al. 2016, Monthly Notices of the Royal Astronomical Society, , 462, 893

Romanowsky, A. J., & Fall, S. M. 2012, The Astrophysical Journal, Supplement, , 203, 17

Sales, L. V., Navarro, J. F., Theuns, T., et al. 2012, Monthly Notices of the Royal Astronomical Society, , 423, 1544

Salpeter, E. E. 1955, The Astrophysical Journal, , 121, 161

Sargent, M. T., Daddi, E., Béthermin, M., et al. 2014, The Astrophysical Journal, , 793, 19

Scannapieco, C., Tissera, P. B., White, S. D. M., & Springel, V. 2008, Monthly Notices of the Royal Astronomical Society, , 389, 1137

Schaye, J. 2002, The Astrophysical Journal, 609, doi:10.1086/421232

Schaye, J., & Dalla Vecchia, C. 2008, Monthly Notices of the Royal Astronomical Society, , 383, 1210

Schaye, J., Crain, R. A., Bower, R. G., et al. 2015, Monthly Notices of the Royal Astronomical Society, , 446, 521

Schinnerer, E., Groves, B., Sargent, M. T., et al. 2016, The Astrophysical Journal, , 833, 112

Sersic, J. L. 1968, Atlas de Galaxias Australes

Shen, S., Mo, H. J., White, S. D. M., et al. 2003, Monthly Notices of the Royal Astronomical Society, , 343, 978

Sheth, R. K., Mo, H. J., & Tormen, G. 2001, Monthly Notices of the Royal Astronomical Society, , 323, 1

Shibuya, T., Ouchi, M., & Harikane, Y. 2015, The Astrophysical Journal, Supplement, , 219, 15

Simard, L., Koo, D. C., Faber, S. M., et al. 1999, The Astrophysical Journal, , 519, 563

Skelton, R. E., Whitaker, K. E., Momcheva, I. G., et al. 2014, The Astrophysical Journal, Supplement, , 214, 24

Smith, R. E., Peacock, J. A., Jenkins, A., et al. 2003, Monthly Notices of the Royal Astronomical Society, , 341, 1311

Somerville, R. S., Hopkins, P. F., Cox, T. J., Robertson, B. E., & Hernquist, L. 2008, Monthly Notices of the Royal Astronomical Society, , 391, 481

Somerville, R. S., Behroozi, P., Pandya, V., et al. 2018, Monthly Notices of the Royal Astronomical Society, , 473, 2714

Sommer-Larsen, J., Gelato, S., & Vedel, H. 1999, The Astrophysical Journal, , 519, 501

Springel, V. 2005, Monthly Notices of the Royal Astronomical Society, , 364, 1105

Steinmetz, M., & Navarro, J. F. 1999, The Astrophysical Journal, , 513, 555

Stevens, A. R. H., Croton, D. J., & Mutch, S. J. 2016, Monthly Notices of the Royal Astronomical Society, , 461, 859

Stinson, G., Seth, A., Katz, N., et al. 2006, Monthly Notices of the Royal Astronomical Society, , 373, 1074

Suginohara, T., & Ostriker, J. P. 1998, The Astrophysical Journal, , 507, 16

Tasca, L. A. M., Kneib, J. P., Iovino, A., et al. 2009, Astronomy & Astrophysics, , 503, 379

Teklu, A. F., Remus, R.-S., Dolag, K., et al. 2015, The Astrophysical Journal, , 812, 29

Tonini, C., Mutch, S. J., Wyithe, J. S. B., & Croton, D. J. 2017, Monthly Notices of the Royal Astronomical Society, , 465, 4133

Toomre, A. 1964, The Astrophysical Journal, , 139, 1217

Tornatore, L., Borgani, S., Springel, V., et al. 2003, Monthly Notices of the Royal Astronomical Society, , 342, 1025

Trujillo, I., Conselice, C. J., Bundy, K., et al. 2007, Monthly Notices of the Royal Astronomical Society, , 382, 109

van der Wel, A., Franx, M., van Dokkum, P. G., et al. 2014, The Astrophysical Journal, , 788, 28

Vecchia, C., & Schaye, J. 2012, Monthly Notices of the Royal Astronomical Society, 426, doi:10.1111/j.1365-2966.2012.21704.x

Vitvitska, M., Klypin, A. A., Kravtsov, A. V., et al. 2002, The Astrophysical Journal, , 581, 799

Vogelsberger, M., Genel, S., Springel, V., et al. 2014, Monthly Notices of the Royal

Astronomical Society, , 444, 1518

White, S. D. M., & Frenk, C. S. 1991, The Astrophysical Journal, , 379, 52

Wiersma, R. P. C., Schaye, J., & Smith, B. D. 2009, Monthly Notices of the Royal Astronomical Society, , 393, 99

Yajima, H., Shlosman, I., Romano-Díaz, E., & Nagamine, K. 2015, Monthly Notices of the Royal Astronomical Society, , 451, 418

Zhu, C., Byrd, R. H., Lu, P., & Nocedal, J. 1997, ACM Trans. Math. Softw., 23, 550

Zitrin, A., Zheng, W., Broadhurst, T., et al. 2014, The Astrophysical Journal, Letters, , 793, L12